

Evidence for Martian electrostatic charging and abrasive wheel wear from the Wheel Abrasion Experiment on the Pathfinder Sojourner rover

Dale C. Ferguson, Joseph C. Kolecki, Mark W. Siebert, and David M. Wilt

NASA Lewis Research Center, Cleveland, Ohio

Jacob R. Matijevic

Jet Propulsion Laboratory, Pasadena, California

Abstract. The Wheel Abrasion Experiment (WAE) on the Mars Pathfinder rover was designed to find out how abrasive the Martian dust would be on strips of pure metals attached to one of the wheels. A specially modified wheel, with 15 thin film samples (five each of three different metals), specularly reflected sunlight to a photovoltaic sensor. When the wheel was rotated to present the different sample surfaces to the sensor, the resulting signal was interpreted in terms of dust adhesion and abrasive wear. Many data sequences were obtained. Ground tests of similar wheels in a simulated Martian environment showed that static charging levels of 100–300 V could be expected. To prevent the possibility of Paschen discharge in the low-pressure Martian atmosphere, charge dissipation points were added to the Sojourner rover and were shown in ground tests to keep charging levels at 80 V or less. Nevertheless, significant dust accumulations on Sojourner's wheels may be interpreted as evidence for electrostatic charging. Simple considerations of the expected maximum level of charging and electrostatic dust adhesion lead to an estimate for the size of the adhering dust grains. From the WAE data, it is hypothesized that the photoelectric effect is the most important mechanism for slow discharge in Martian daylight. Sensor signals obtained late in the Pathfinder mission show that significant wheel wear was seen on the metal wheel strips, with the most wear on the thinnest aluminum samples and the least on the thickest nickel and platinum samples. An estimate is made of the reflectance of the adhering Martian dust. The depth of dig of the WAE wheel shows that the dust is in some places very loose and in others tightly packed. Finally, comparison of the WAE results with ground test results makes possible a comparison of the Martian soil with mineral grain types and sizes found on Earth and show that the Martian dust is fine-grained and of limited hardness.

1. Introduction

The engineering properties of the Martian dust have been of interest to spacecraft designers since the dawn of Martian robotic exploration. We have known for decades that the dust is picked up and carried by Martian winds during the global dust storms. While others [Landis *et al.*, 1997; Jenkins *et al.*, 1997] have placed experiments on Mars Pathfinder to determine how much dust will be deposited on solar arrays, etc., we have been more interested in other aspects of the dust [Ferguson, 1997]. For instance, is the dust fine enough to get into mechanisms? Is the dust very abrasive, so that mechanisms could be at risk? And, finally, could electrical properties of the dust prove to be a problem? For instance, can a moving rover build up an electrostatic charge sufficient to cause a Paschen discharge (a breakdown of the air by ionization cascade) in the thin Martian atmosphere? And can electrostatic dust attraction prove to be a problem for charged surfaces [Kolecki and Hillard, 1991]? The Wheel Abrasion Experiment (WAE) was designed to answer the questions about dust abrasiveness and

Copyright 1999 by the American Geophysical Union.

Paper number 98JE02249.
0148-0227/98/98JE-02249\$09.00

was included on the Mars Pathfinder Sojourner rover. WAE also answered some of our questions about electrostatic charging. In this paper, we detail the results obtained so far from the operation of WAE on the Martian surface.

The right central wheel of Sojourner was modified to include the WAE. The modifications, designed and constructed at the NASA Lewis Research Center, consisted of replacing the central 2.5 cm of the traction-aiding "growlers" on the wheel with strips of black anodized aluminum having metal coatings of varying thicknesses and hardnesses. Three such strips were mounted to the wheel surface with adhesives. The first strip was coated with nickel, the second with platinum, and the third with aluminum, metals chosen for their adhesion to the black anodized substrate, their reflectivity, and their noncorrosive nature. Each 12 cm strip was coated with five thicknesses of metal, of 200, 300, 450, 700, and 1000 Å (see Figures 1 and 2). These thicknesses are incorrectly reported by Siebert [1997] but are correctly given by Hepp *et al.* [1996]. The coated samples were 1.5 cm in length, with three uncoated black-anodized surfaces in between for a baseline. The coating thicknesses were chosen, based on ground tests, because significant wear was seen when the wheel was rotated through the simulated Martian dust. For a fuller description of the metals selection, see Hepp *et al.* [1996].

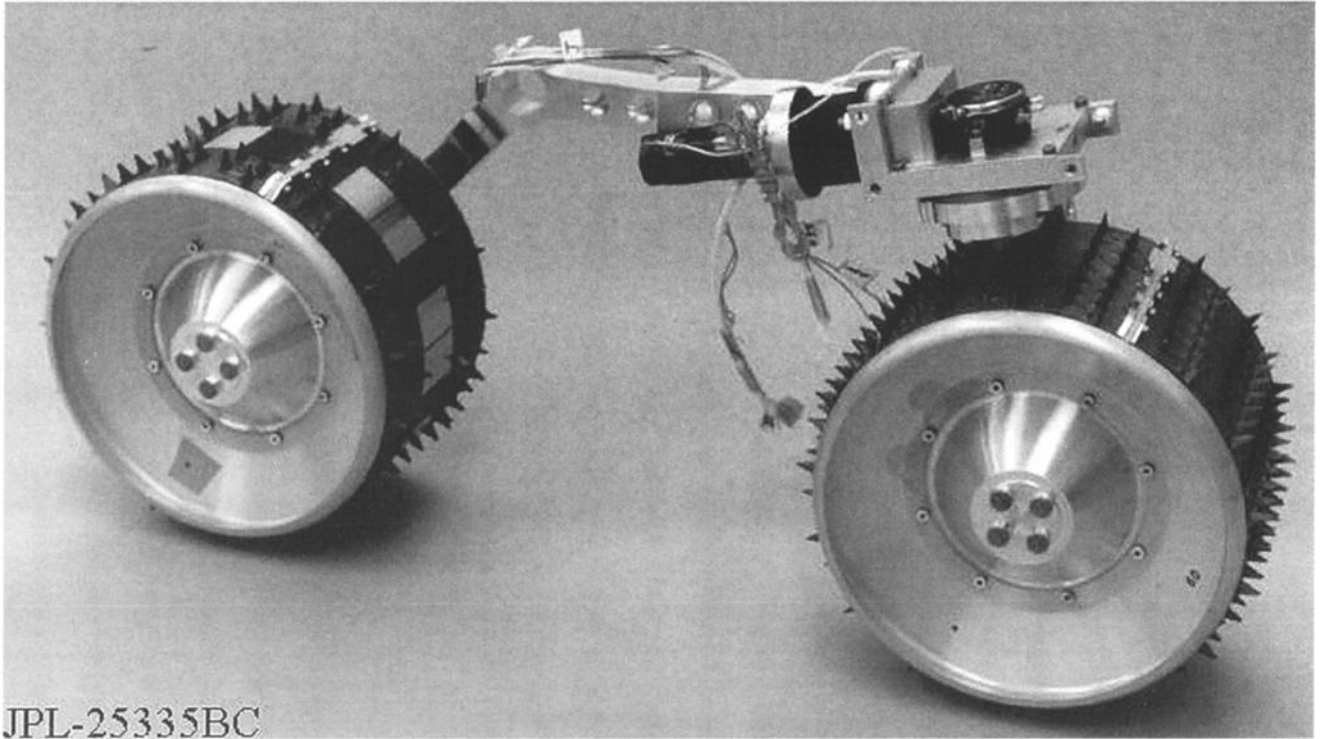


Figure 1. Preflight Sojourner right front rocker and wheel assembly. Front is to the right. The WAE wheel is shown with its reflective metallic strips. The WAE sensor is mounted near the bend in the WAE wheel support.

On Mars, the amount of wear for each metal coating was detected by a specially built photodetector, mounted on the wheel strut [see *Wilt et al.*, 1997]. During each experiment, the WAE wheel was rotated backward through two revolutions, while Sojourner was held stationary by the other five nonrotating wheels, and the photodetector determined the amount of Martian sunlight reflected in turn by each metal coating on each WAE wheel strip. In some experiments the wheel was then rotated three revolutions without taking WAE data to help build up wear and, then, two more revolutions while taking data. Ideally, Sojourner was first pointed in the direction that would lead to the best specular reflection from the Sun, and the change in the amount of reflected signal indicated the amount of metal which had been removed by abrasion from each surface. In reality, inaccurate pointing and dust unevenly coating the wheel led to difficulties in interpreting the data. The wheel rotation was at a rate of 1 cm/s, and five readings were obtained from each coated sample in each wheel rotation. The central, or peak, reading from each sample is, by design, unaffected by light reflected from any adjacent samples.

Complicating the interpretation of the results was a change in the reflectance due to dust which stuck to the WAE wheel. The Martian environment is extremely dry, and the WAE wheel was therefore subject to triboelectric charging (static charging due to friction) during traverses. It was known from ground tests of a simulated WAE wheel in a simulated Martian atmosphere at the Lewis Research Center [*Siebert and Kolecki*, 1996] that the wheel would pick up dust and charge to a steady state value of greater than 100 V. When the wheel was jarred, the wheel potential fell dramatically, and dust fell off the wheel. Thus charging and dust coverage were anticipated to be possible problems with the data analysis.

A simple model of the peak specular reflection from each sample is that the signal S is given by

$$S = I_{\text{sun}} R_s A [1 - f(1 - (R_d/R_s))], \quad (1)$$

where I_{sun} is the solar intensity, R_s is the specular reflectivity of the sample, A is the area of the sample reflecting to the sensor, f is the fraction of the area coated by dust, and R_d is the specular reflectivity of the dust. This assumes that each dust grain is optically thick but that only a fraction of the surface is covered by dust. Then the ratio of the normalized signals from an experimental sample to the calibration (cal) signal for that sample is proportional to $(I_{\text{sun}}/I_0)[1 - f(1 - (R_d/R_s))]$, where I_0 is the solar intensity in the cal signal.

If $R_d/R_s \ll 1$, as will be the case from the highly specularly reflecting metal samples, then the signals will be approximately diminished by the factor $(1 - f)$ for these samples. Thus if the wheel dust coating is uniform and the dust is poorly specularly reflecting, the reflected signals from each metal sample will be reduced by about the same fraction, so that normalized signals will still be useful for comparing the amount of wear seen on different samples. Confirmation of this fact was obtained in ground tests [*Siebert*, 1997].

Calibration of the WAE flight wheel and detector was done using a full spectrum collimated light source at the Jet Propulsion Laboratory (JPL) shortly prior to shipping the wheel to Cape Canaveral. The average reflected signal of the baseline black anodized regions was found to be approximately 15% of the peak metallic reflected signal over the effective wavelength interval (360–870 nm). Since the peak reflectance was from the aluminum samples at about 71% [*Hepp et al.*, 1996], the estimated average reflectance of the black anodization is about

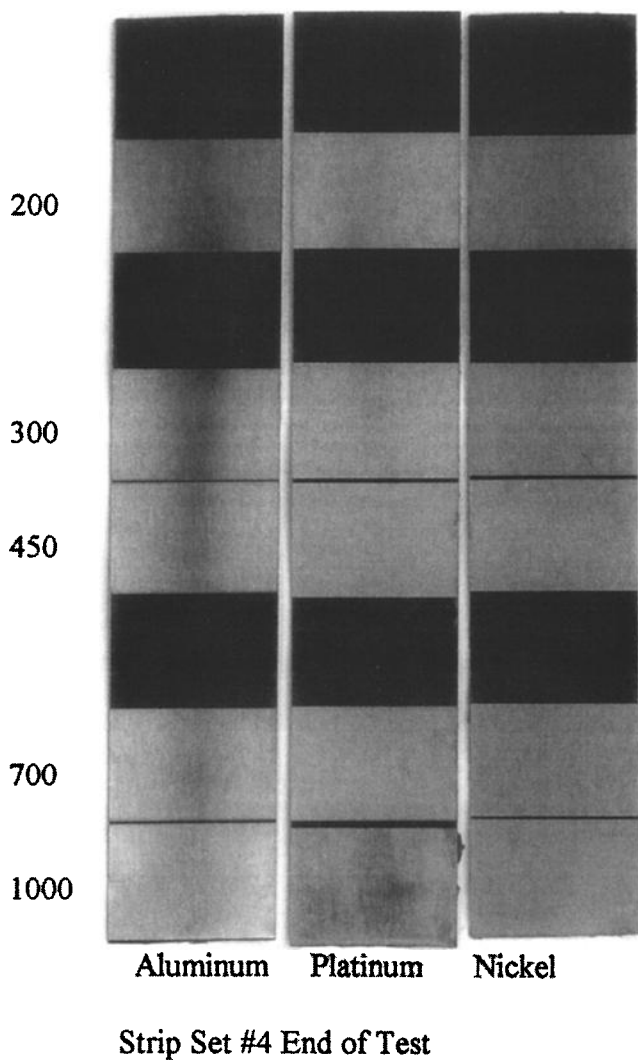


Figure 2. WAE strips used in one of the ground tests. On the WAE wheel, such strips were attached sequentially.

11%. Most of the reflectance of black anodized aluminum is in the near infrared.

2. Charging Mitigation on Sojourner

While the Sojourner rover was being developed for the Mars Pathfinder Mission, tests and calculations done at the NASA Lewis Research Center indicated the possibility that, when moving over the Martian surface, Sojourner would accumulate electrostatic charge. In a simulated test environment at Lewis, this charge was repeatedly shown to raise on-board electrical potentials above the suspected very low Paschen minimum of the Martian atmosphere (100 V [Haberle and Greeley, 1991]). Potentials of this magnitude and greater might be capable of initiating Paschen discharge across electrode distances comparable to separations of parts of Sojourner (millimeters to centimeters), with possible disruption of on-board electronics and logic, and production of electromagnetic noise. Methods of eliminating built-up charge were also explored. A lightweight, passive discharge method was chosen: the use of small metal discharge points to "bleed" accumulated charge off Sojourner and into the Martian atmosphere.

Ground tests were conducted in a simulated Martian envi-

ronment. A cylindrical chamber was evacuated, then backfilled with a Viking-derived gas mix to a pressure of 7 mbar. A weighted rover wheel was mounted in a movable tray filled with crushed basalt and driven at typical equivalent rover speeds of 0.76–1.5 cm/s. The tests repeatedly showed that the wheels accumulated electrically charged dust (Figure 3) and developed steady state electrical potentials averaging 110 ± 25 V relative to chamber ground [Siebert and Kolecki, 1996]. The basalt is believed to become triboelectrically charged after being moved about by slip during wheel starts and stops, or compacted by the wheel during steady state rolling operation. (Starts occasionally gave rise to transient voltages greater than 300 V with a risetime of one wheel revolution and a settling time of several (<10) wheel revolutions.) The adhering dust transferred a net nonzero charge to the wheel, raising its electrical potential relative to chamber ground.

The capacitance of the wheel relative to the chamber was estimated to be 74 pF; the electrical charge on the wheel was estimated to be 8.1 nC. With an accumulated net charge of this magnitude and average arc time interval of 1 μ s, arc currents could approach 10 mA. Discharges of this magnitude could interfere with the operation of sensitive electrical elements on the rover [Haberle and Greeley, 1991; Kolecki and Hillard, 1991; Hillard and Kolecki, 1993]. If similar charging and comparable potential differences occurred on Mars, then disruptive electrical discharges through the Martian atmosphere appeared to be a likely occurrence on Sojourner. When apprised of these results, Pathfinder engineers decided to implement the recommendation of adding the discharge points to the Sojourner. (Subsequently, modifications were also made to rover on-board electronics.) Six tungsten points were electromachined from 10 mil tungsten wire at Case Western Reserve University, Cleveland, four of which were mounted on the rover antenna base. While tests showed that the points did not entirely eliminate accumulated charge, they appeared to work well enough to maintain on-board electrical potential differences at acceptable levels (in the chamber, 60–80 V).

3. Electrostatic Charging on Mars

During the mission, lander camera images of the Sojourner rover on Mars provided evidence of dust accumulation on rover wheels during traverses, turns, and crabbing maneuvers. In addition, whenever WAE experiments were performed, dust would depress the reflectance signals. Dust adherence was first identified on sol 4 (each sol is one Martian day after landing), and carefully watched and evaluated (see Figure 4). In Figure 5 can be seen the severely depressed flight reflectance signal obtained on sol 4 beginning with the platinum samples and continuing with the aluminum samples. The sol 22 end-of-day image (Figure 6) clearly shows fine red dust concentrated around the wheel edges with additional accumulation in the wheel hubs. A sol 41 image of the rover (Figure 7) shows a more uniform coating of dust on the wheel drive surfaces with accumulation in the hubs similar to the previous figure. In Figure 7, note particularly the loss of black-white contrast on the Wheel Abrasion Experiment strips (center wheel). This loss of contrast was also seen when dust accumulated on test wheels in the laboratory (Figure 3) [Siebert and Kolecki, 1996]. The tentative conclusion for the Sojourner observations is that the surface dust may be acquiring an electrostatic charge during rover traverses and adhering to the rover wheels, transfer-

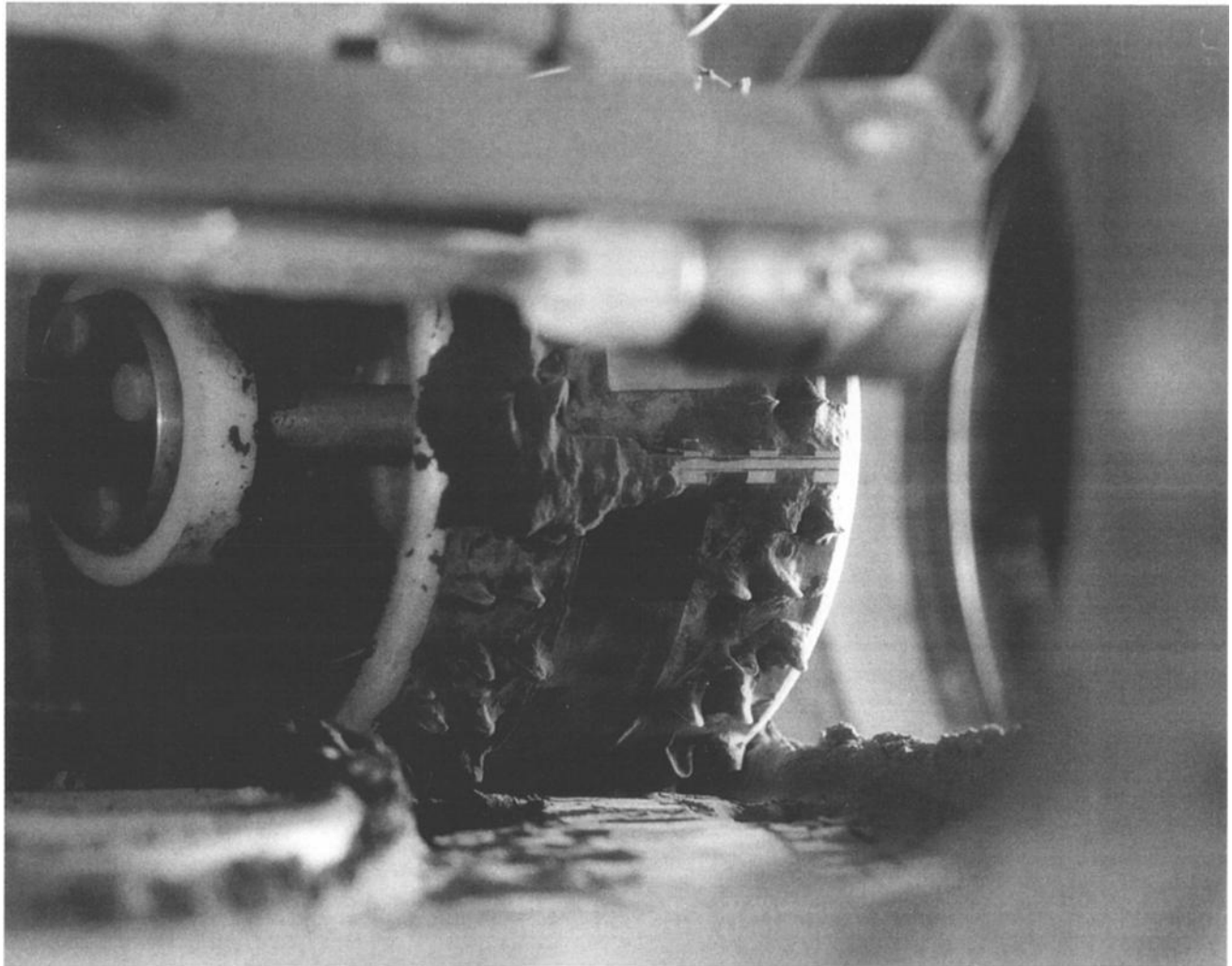


Figure 3. WAE wheel picking up dust in ground tests. In the foreground, the Mars environment chamber porthole frames the tray of simulated soil. The cleated wheel in the background is becoming caked with material. Dust in the foreground is packed smooth by the central wheel strip.

ring electrical charge to the rover. Since Sojourner carried no instruments to measure on-board electrical charge, no confirmatory measurements were possible. Such measurements appear desirable on future rover/lander missions to Mars to enable characterization of the physical and electrical properties of the Martian surface dust.

In ground tests, although the dust in the laboratory wheel tray averaged about $70 \mu\text{m}$ in grain size, dust removed from the wheel averaged only about $10 \mu\text{m}$ in size (clay size). Much coarser grains were left behind in the wheel track. Charge differentiation was also observed: the wheel always charged positively, and the wheel track negatively, relative to chamber ground. Additionally, grain size estimates of $2\text{--}10 \mu\text{m}$ were derived for the Martian surface materials from the Viking Gas Exchange Experiment [Moore et al., 1987]. These size estimates approximately match the laboratory wheel samples. Further, if electrostatic attraction is assumed to be the dominant force between a dust grain and the wheel, then assuming that the electrostatic force must at least equal the weight of a dust grain, the expression

$$r = (3/16\epsilon_0)(1/\rho g)(CV/A)^2 \quad (2)$$

may be derived for the radius r of the grain, where ϵ_0 is the

permittivity of free space, ρ is the density of a grain (density is $2.6 \times 10^3 \text{ kg/m}^3$ [Moore et al., 1987]), g is the acceleration of gravity on Mars, and C , V , and A are the strip capacitance, voltage, and area, respectively, all in MKS units. The measured rover capacitance is about 30 pF (B. Wilcox, personal communication, 1997). This value is similar to the measured capacitance of a wheel strip of $1\text{--}100 \text{ pF}$. Assuming a wheel charging voltage of $60\text{--}80 \text{ V}$ (cf. laboratory results), and a maximum strip capacitance of 100 pF (since all wheel strips were seen to charge independently), one obtains a maximum grain radius range of about $10\text{--}18 \mu\text{m}$. The patchy nature of adhesion to the wheels may be due to differences of the effective capacitance or resistance of different parts of the wheel on the soil. However, the reflectance data on sol 4 may give an important clue to the patchiness. There was a close correspondence between the dirty parts of the WAE wheel (as determined from the low reflectivity) and the parts of the wheel which had been in the shade during the traverse immediately preceding the early morning data taking. This suggests that sunlight may discharge parts of the wheel that become illuminated. A natural mechanism for this type of discharge is the photoelectric effect. The metal strips or the dust exposed to the UV in

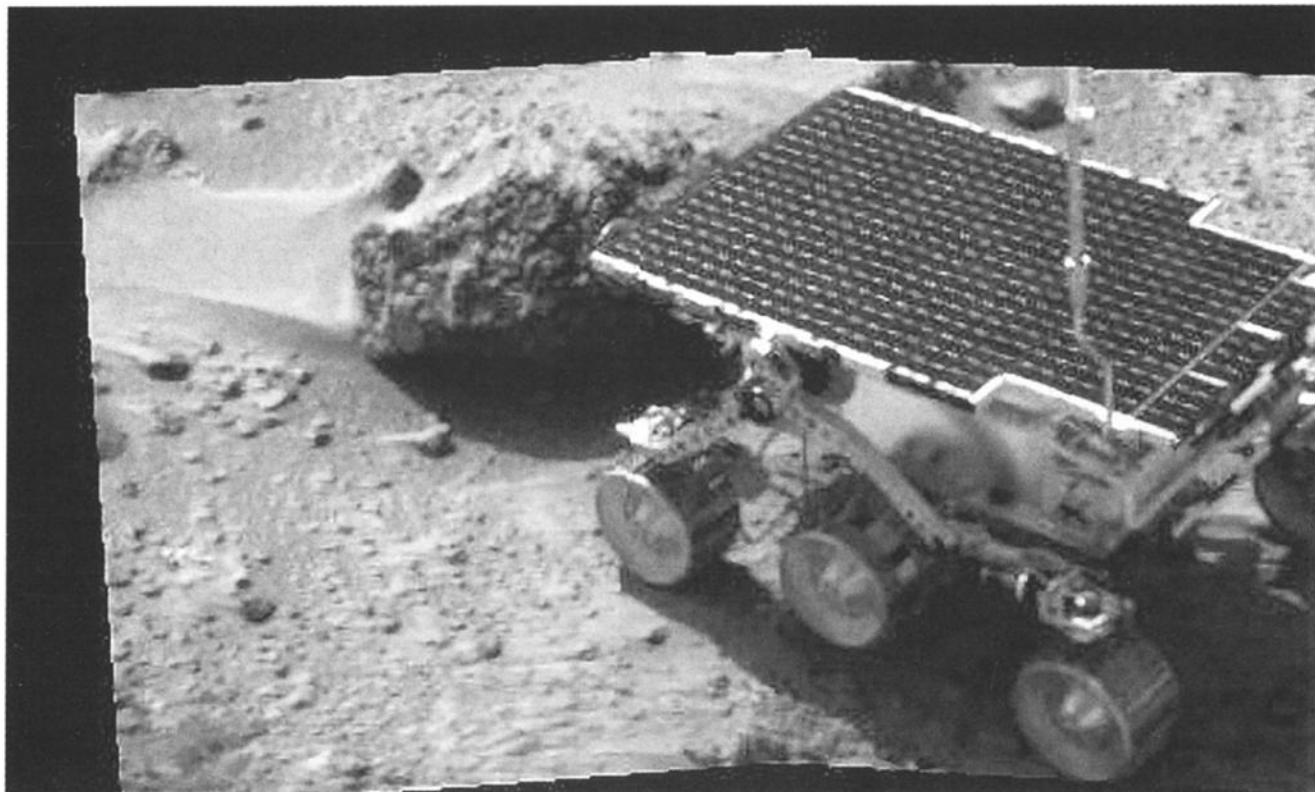


Figure 4. The WAE wheel on sol 3 before dust accumulation was first noticed on sol 4.

sunlight may have discharged through photoemission of electrons, and when discharged, the adhering dust was released. In order for this mechanism to be effective, the photoemission current must more than equal the charging current during a traverse. Using the estimate for strip capacitance above, and an estimated charging time of 1 s, we find a charging current of 8 nA. The strip area newly exposed to sunlight is about $2.5 \text{ cm}^2/\text{s}$, implying a minimum necessary photoemission current of about

3 nA/cm^2 . This is entirely reasonable for Martian sunlight (D. B. Snyder, personal communication, 1998).

In laboratory tests with different soil types, it was found that grain sizes of less than about $40 \mu\text{m}$ resulted in severe wheel clogging. Similar clogging may also be seen in several of the images of Sojourner on the Martian surface (Figure 8). Such pictures also seem to suggest a grain size of less than about $40 \mu\text{m}$ for the Martian dust.

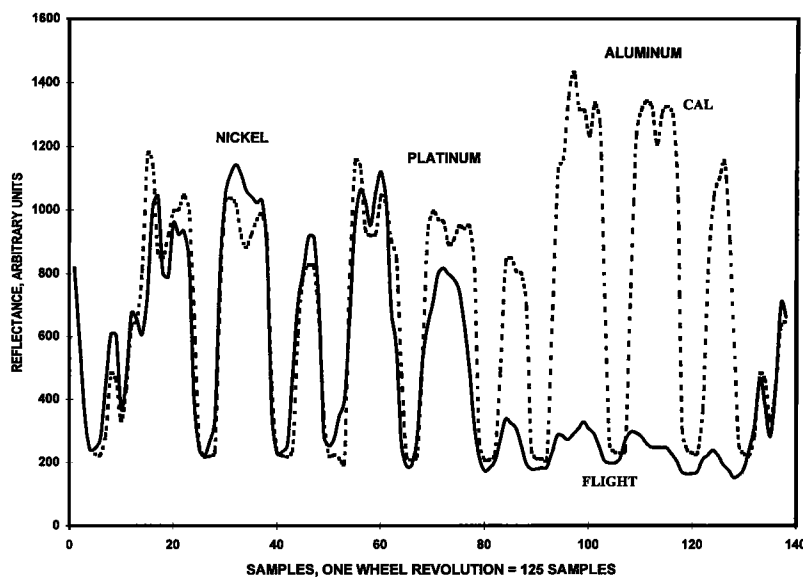


Figure 5. Normalized sol 4 reflectance signals, compared to the preflight calibration. Dust coverage starts with the platinum samples.

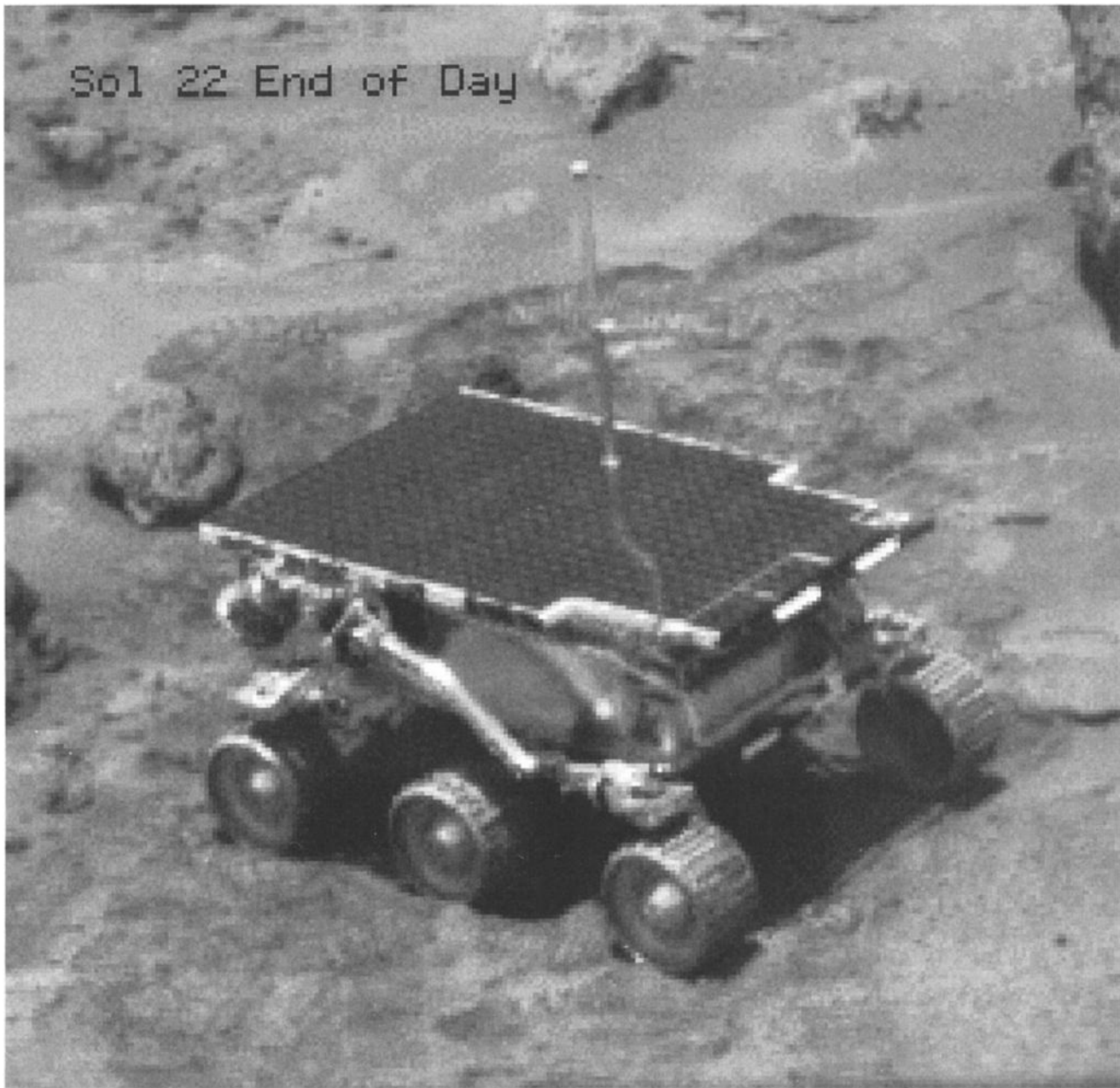


Figure 6. End of day image, sol 22. Patchy coverage of the WAE wheel is seen, indicating charged and uncharged regions.

Corroboration for our grain size estimates may be found in the work by the *Rover Team* [1997]. The smooth tracks of the Sojourner wheels in the soil are interpreted as indicating a grain size of $40 \mu\text{m}$ or less.

Large systems (piloted and robotic) are being contemplated for the Martian surface in the foreseeable future. The design of such systems requires a detailed knowledge of how they will interact with their environment. Validated environmental interaction models and guidelines for the Martian surface must be developed in order for design engineers to test out new ideas prior to cutting hardware. These models and guidelines cannot be validated without actual data. Electrical charging of vehicles and astronauts moving across the Martian surface can have moderate to severe consequences if large potential differences develop [Kolecki and Hillard, 1991]. The reported

observations from Sojourner point to just such a possibility. It is desirable to quantify these results. The various lander/rover missions being planned for the upcoming decade provide the means for doing so. They should therefore carry appropriate instruments, not only to measure vehicle charging, but to characterize all of the natural and induced electrical phenomena occurring in the environment, and to assess their impact on future missions.

4. Abrasive Wheel Wear on Mars

On sol 53, a nearly perfect set of data was obtained. In Figure 9 we see the reflectance data obtained, along with the calibration signal obtained before flight. The data consisted of two complete wheel rotations, and the degree of consistency

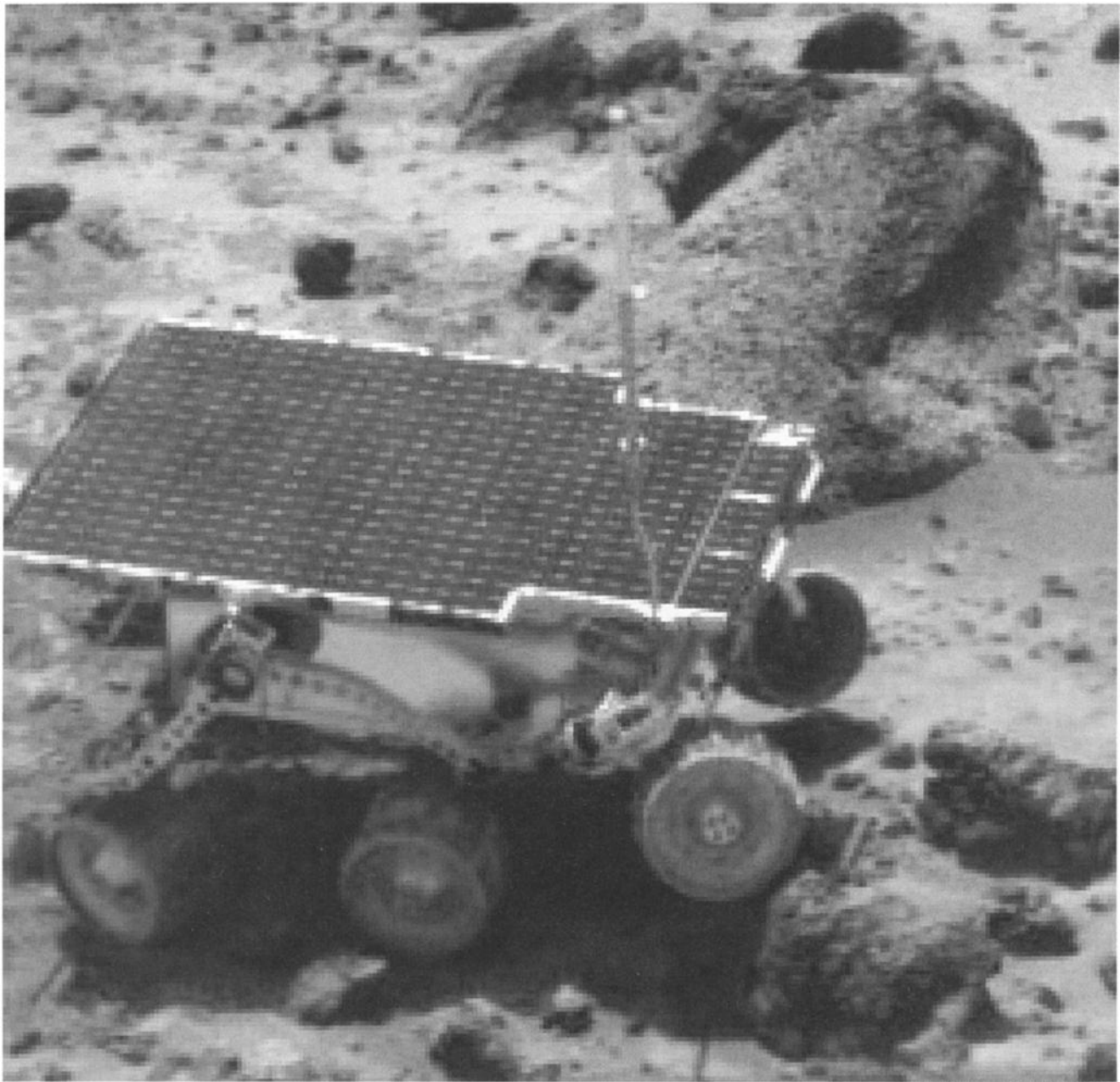


Figure 7. Sol 41. Notice the lack of contrast between the metal coated wheel samples and the black anodized surfaces.

between the two rotations was remarkable. We will show that these data are consistent with a significant amount of abrasive wheel wear on the WAE wheel. This can be seen in Figures 10–12, where ratios of the aluminum, nickel, and platinum signals to the cal signals are shown. Ratios are used here because an even coating of dark dust on the samples is not expected to change the ratios very much, whereas it most certainly will detract from the overall reflectance. Ratios in between the metal samples will roughly indicate the reflectivity of the anodized aluminum when covered with dust, compared to its pristine condition. Anodized aluminum is expected to undergo no wear because of its extreme hardness. Arrows in the figures mark the peak positions, where the signal of one metal sample is unaffected by adjacent samples.

The results shown in Figures 10–12 are obviously affected by

the normalization chosen. In terms of (1), normalization corresponds to modifying the I_{sun} term by a factor that is the same for all samples. Let us call this normalizing factor X . Then the ratio of the normalized signal to the calibration signal becomes

$$\text{Ratio} = X\{1 - f[1 - (R_d/R_s)]\}. \quad (3)$$

Abrasion will wear away the softest and thinnest samples first. Using the thick samples of nickel, platinum, and the black anodized aluminum, we can solve for X , f , and R_d . Reflectances of the pristine nickel and platinum samples are taken from Hepp *et al.* [1996]. The following approximate values are found:

$$X = 1.54, \quad (4)$$

$$f = 0.66, \quad (5)$$



Figure 8. Sol 12. Here the dust is clogging the WAE wheel. Compare to the caking in Figure 3.

$$R_d = 0.17. \quad (6)$$

Thus the dust is very dark but not quite as dark as the black anodized aluminum ($R = 0.11$). Our assumption that the normalized ratios will be reduced by dust buildup in approximately the same ratio is correct, since $R_d \ll R_s$ for all of the metal samples. Substituting these values into (1) for aluminum, we find that the thick aluminum samples should have a normalized ratio of 0.89, much smaller than the 1.0 observed. What can account for the discrepancy? We believe that a thin layer of aluminum was removed from the high spots on the sample, improving the specular reflectivity. On the thin samples, removal of this material will lay bare the anodized aluminum underneath and reduce the average reflectivity. This is what is seen for the thin aluminum samples. Real abrasive wear should affect the reflectance most for the softest metal

(aluminum) and for the thinnest metal samples (200 Å samples). This is exactly the pattern seen in these traces.

Furthermore, one can perform linear regression on the ratios versus sample thickness for these samples, to see if there is the expected behavior for true abrasive wear. These results can be seen for all of the sol 53 metal sample peak reflectances in Figure 13. The highest correlation of reflectance ratio with metal thickness occurs for the aluminum samples, where the correlation coefficient is 0.442, corresponding to a significance level of about 80%. For nickel, the correlation is nearly zero, and there is a negative correlation for platinum. Had the normalization been different, the ratios would have all changed, but the sense of the correlations would not. Curiously, platinum seems to be more reflective in its thinnest coatings after some wear. For abrasive wear by a very hard mineral (SiC), the

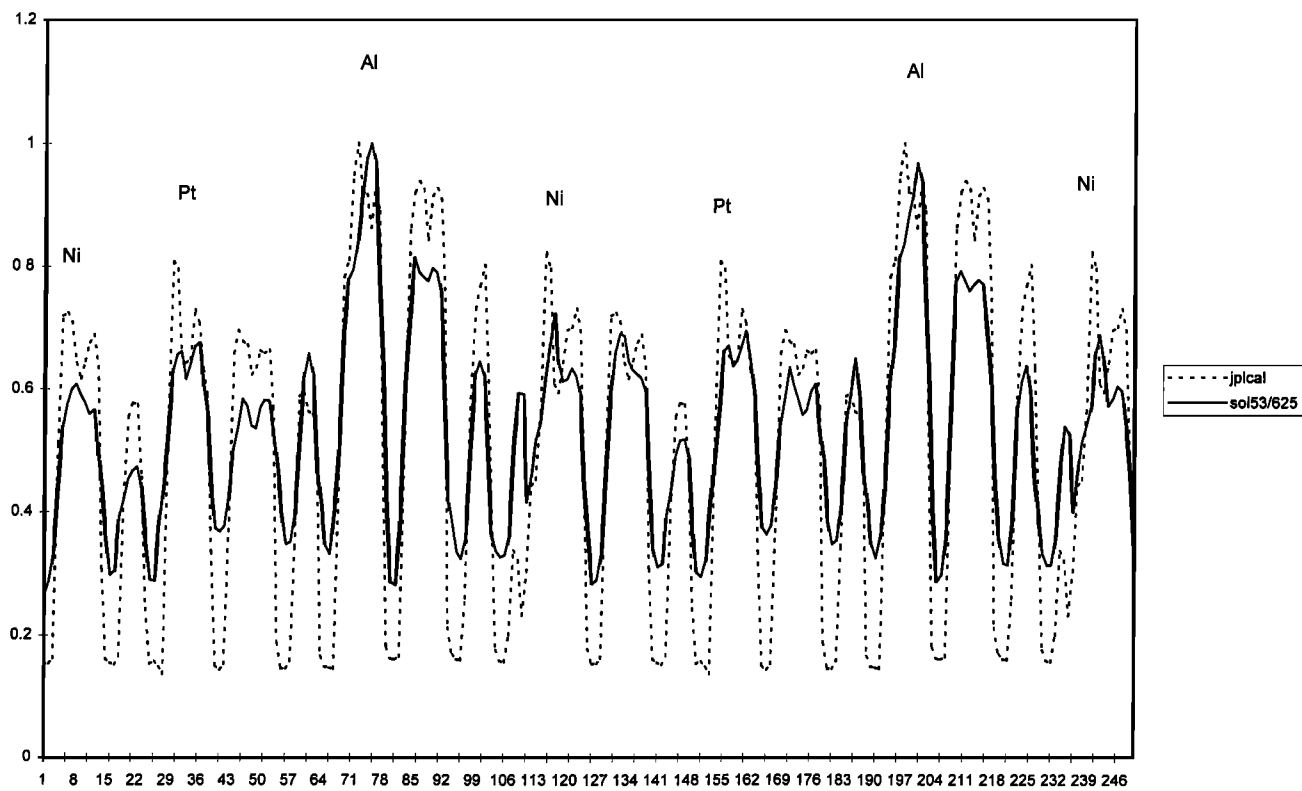


Figure 9. Sol 53 WAE data, normalized to the absolute peak reflectance of the JPL calibration data, also shown.

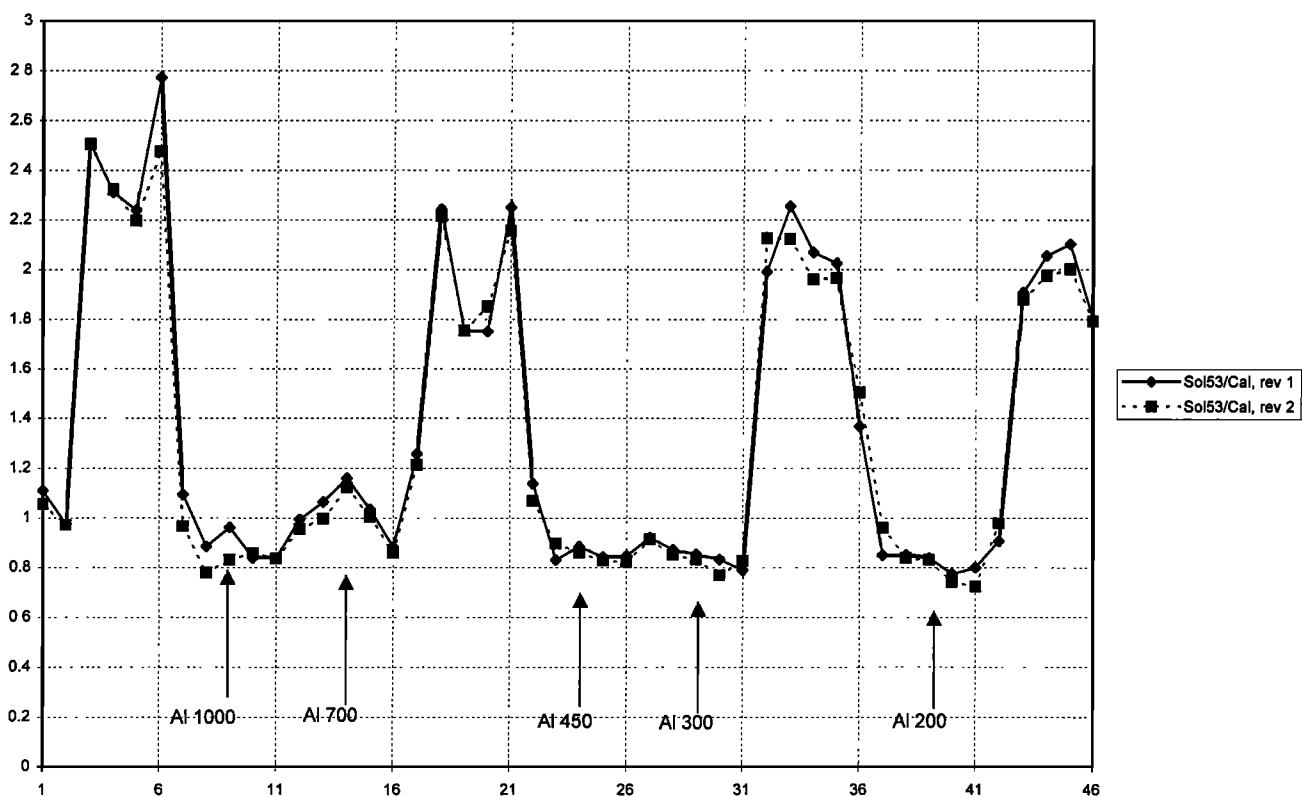


Figure 10. Ratios of the aluminum signals on sol 53 divided by the cal signal.

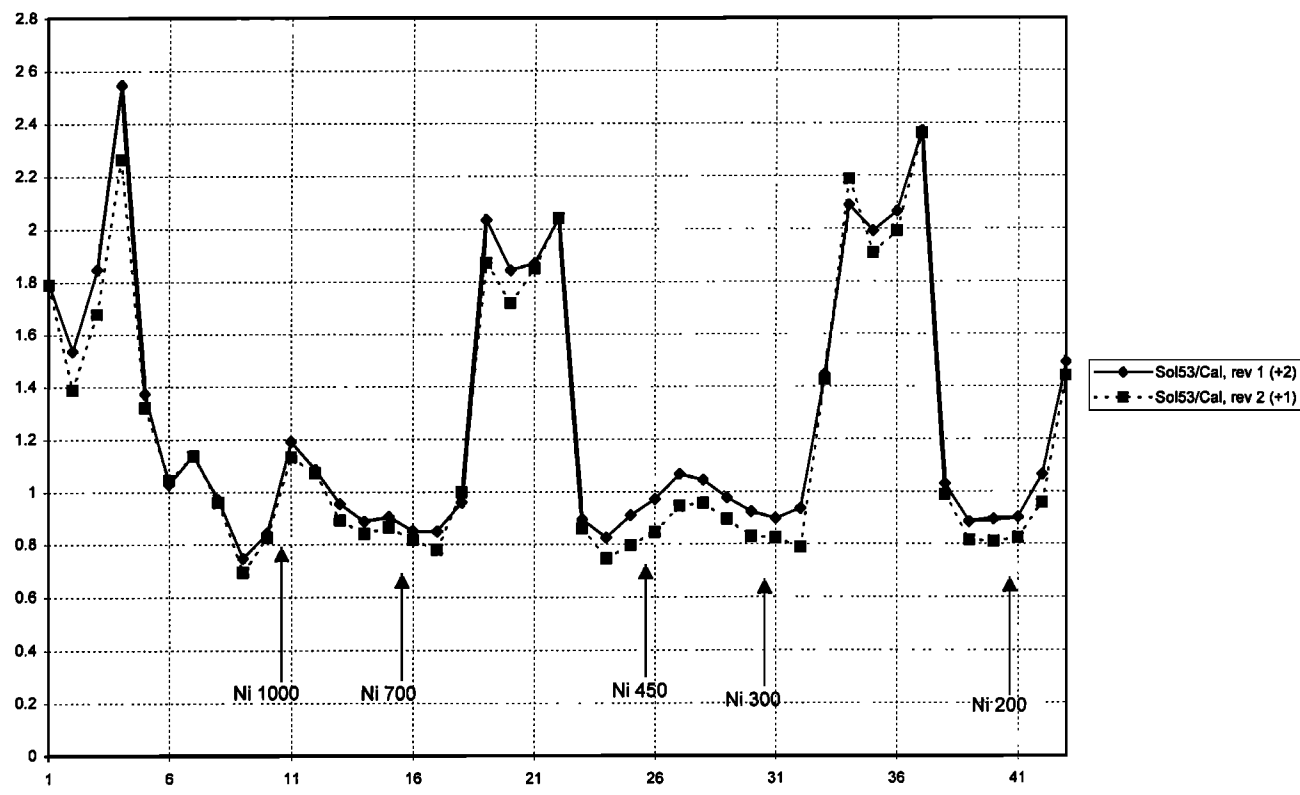


Figure 11. Ratios of the nickel signals on sol 53 divided by the cal signal.

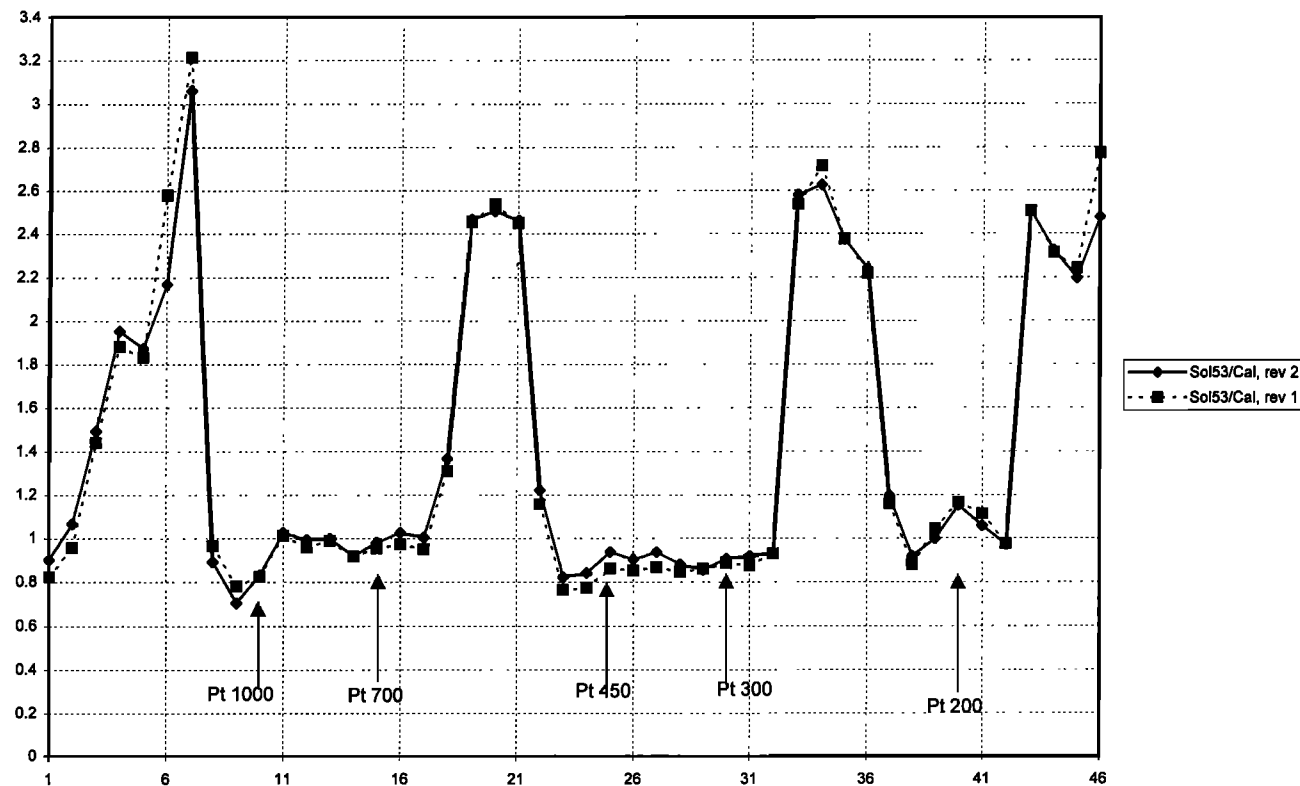


Figure 12. Ratios of the platinum signals on sol 53 divided by the cal signal.

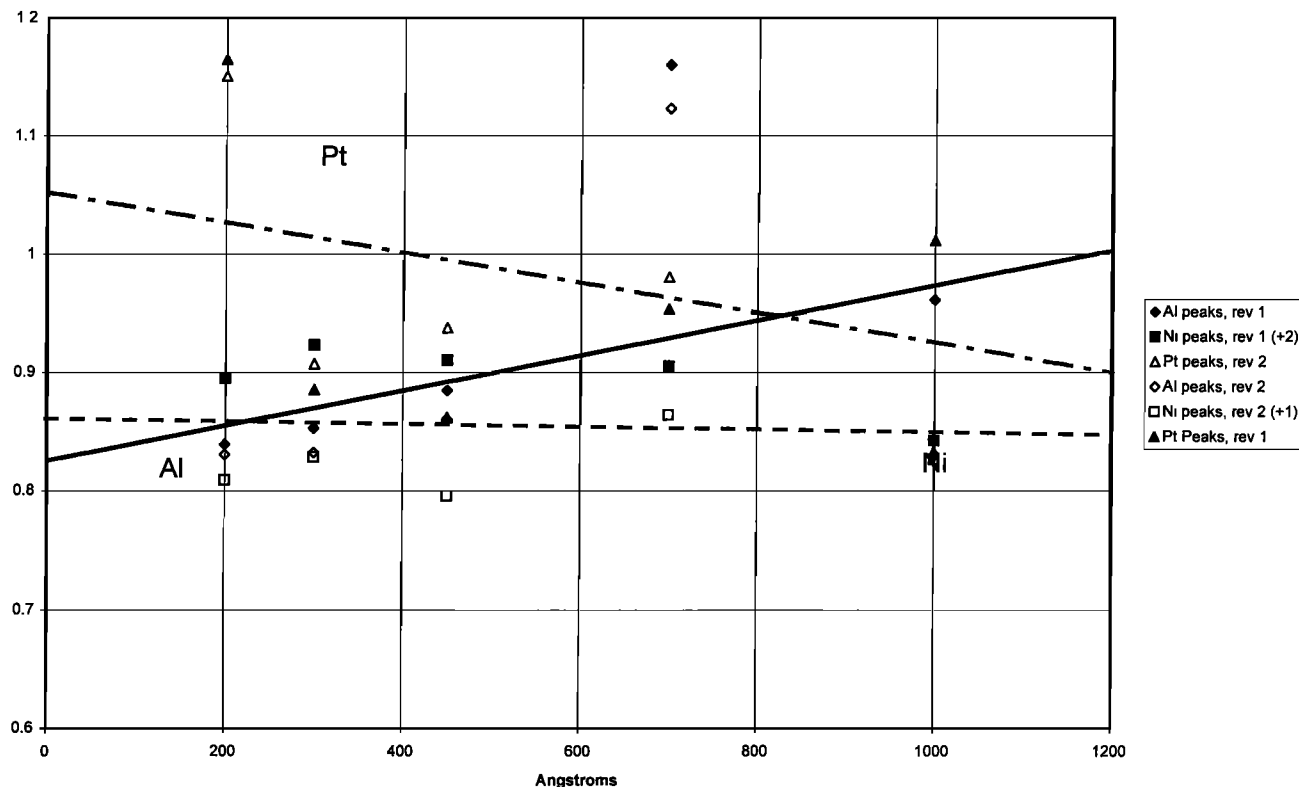


Figure 13. Peak values and linear regression lines of reflectance ratios on sol 53 versus metal coating thickness for all three metals.

platinum signal should have degraded initially about half as fast as the aluminum [Hepp *et al.*, 1996]. While not very significant, the negative correlation observed might indicate some degree of platinum polishing by the Martian dust, indicating that it may have a similar hardness to platinum. If these results are correct, the Martian dust is somewhat harder than alumini-

num, nearly the same hardness as platinum, but softer than nickel. On the Brinell hardness scale, aluminum is about 16, nickel about 100, and platinum about 64 [Chemical Rubber Company, 1961, pp. 2164–2167], or in terms of Mohs' scale of hardness, aluminum is about 2.5, nickel about 5.7, and platinum about 4.3 [Chemical Rubber Company, 1961, pp. 2188–

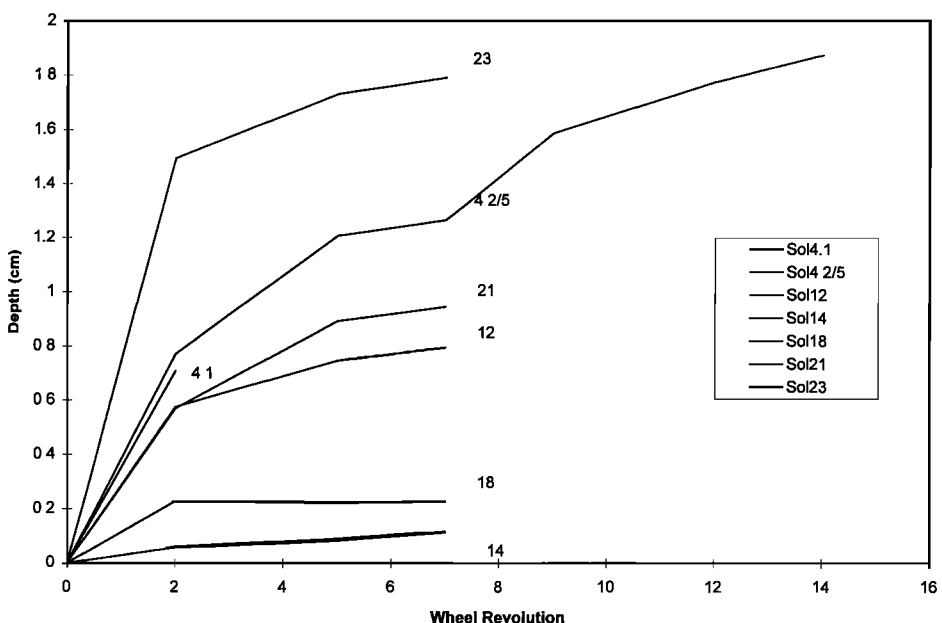


Figure 14. Depth-of-dig versus wheel revolutions for the entire WAE data set when the WAE wheel was in contact with the surface. Sol 5 is a continuation in the same hole dug on sol 4.2.

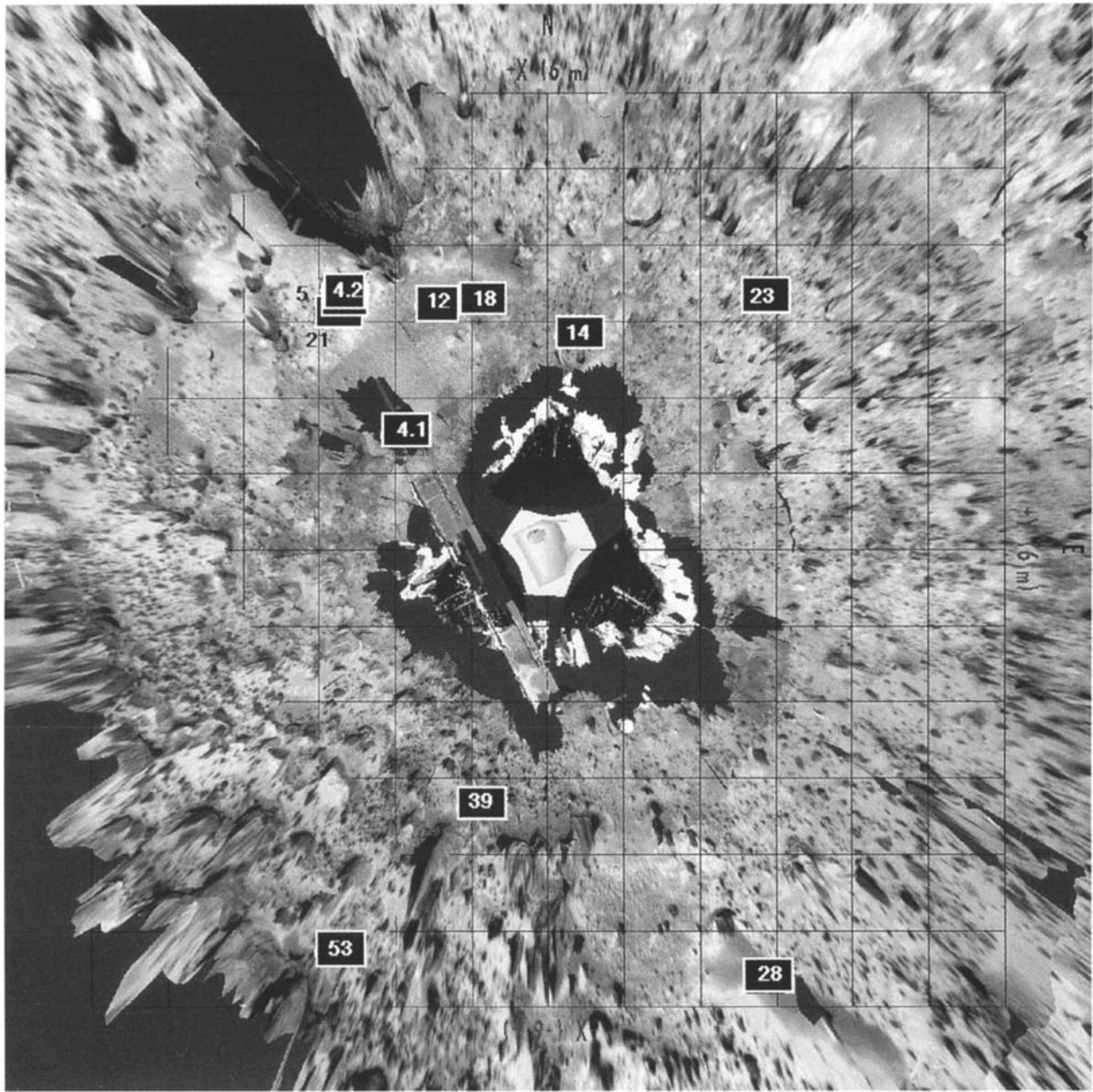


Figure 15. Locations of wheel abrasion experiments, indicated by sol. Grid squares are 1 m on a side.

2189; Hepp et al., 1996]. This places Martian dust with about the same hardness as fluorite or apatite. Of course, the Martian dust may have been harder than this, but the hard nickel was just not worn a significant amount in our limited number of abrasive wheel turns.

How much abrasion has occurred on our samples? If the reflectance signal lost is proportional to the aluminum lost, we could say that perhaps 14% of the thinnest aluminum sample has been worn away, or 28 Å. The error bars on this estimate must be quite large, however. The total number of abrasive WAE wheel revolutions up to and including sol 53 was 55. Of those, 16 were performed on a hard or rocky surface, where the WAE strip was probably not abraded. Thus the loss of aluminum may amount to about 28 Å in 39 wheel revs, or roughly 0.7 Å per revolution.

We are attempting at present to compare the abrasion found

in the flight data with that produced in ground simulations, using different soil types. So far, the best match appears to be with a fairly fine grained (<30 µm) Martian soil simulant. This simulant is an artificial mineral made largely of silicon dioxide and iron oxides [see Gaier and Perez-Davis, 1991], which approximates the elemental combination of Martian soil. We will present the detailed comparisons in a future paper.

5. Depth of Dig in the Martian Dust

During the course of each WAE experiment, Sojourner provided periodic information on the angular displacement of the rover suspension elements (rockers and bogies) relative to the body of Sojourner. These data were reported before and after each experimental sequence element (set of wheel revolutions). We used these data to estimate the depth to which the

WAE wheel had dug as a function of the wheel revolution. Figure 14 shows the data for all of the WAE experiments except for sol 53. The depth of dig is defined as the movement of the WAE wheel in the +z direction (as defined by the rover coordinate system). No attempt was made to translate this depth into the local Martian frame of reference (correct for pitch and roll of the rover) due to the sporadic nature of the rover attitude sensors. It is believed that the difference between the reported depth and the actual depth in the Martian frame of reference is small, given the relatively flat terrain where the experiments were performed.

The dig data fall into three general categories: rock-like or very hard soil material (sols 14 and 18), somewhat softer material (sols 4.1, 4.2, 5, 12, and 21), and loose soil (sol 23). For the positions of the WAE digs, see Figure 15. Sol 14 was done on a feature named Scooby Doo, and sol 18 data were taken in the vicinity of the feature named Cabbage Patch. There was no appreciable change in the depth of the WAE wheel after seven full revolutions at either of these locations. For a fuller description of these areas, see *Rover Team* [1997]. The WAE experiments in the softer material (sol 4.1, 4.2, 5, 12, and 21) all show a similar dig profile, dropping 0.6–0.7 cm in the first two revolutions. The dig rate then begins to decrease with a final depth of 0.8–1.2 cm after seven revolutions.

The sol 5 experiment was conducted on the morning following the sol 4.2 experiment. The rover was not moved in the interval between the experiments, so the WAE wheel began the sol 5 test in the hole left by the sol 4.2 test. As can be seen, the dig rate generally follows the profile established in the sol 4.2 test. There is a slight increase in the initial dig rate for sol 5, possibly due to the rover settling into the soil during the period between experiments. The sol 23 WAE test was conducted in the vicinity of a rock called Snowy. This material was very loose, as demonstrated by the 1.5 cm dig depth in two wheel revolutions. It appears as though the sol 4.2/5 and sol 23 data indicate an asymptotic approach to an ultimate dig depth of approximately 2 cm. This may indicate the presence of a hard, crust-like material at that depth. In preflight sandbox testing done at JPL, the WAE wheel was able to dig >3 cm into sand in a few revolutions. Therefore the dig depth on Mars was not limited by rover mechanical characteristics, and we must infer that the Martian dust in places is much more compacted only a few centimeters beneath the surface than it is at the surface. These results should be compared with those found by *Moore et al.* [this issue] using other Sojourner wheels as part of the soil mechanics experiments.

6. Conclusions

The WAE experiment has provided the first evidence for abrasion and electrostatic charging by a Rover moving over the dust of Mars. The grain size (diameter) of the Martian dust inferred from electrostatic charging considerations is less than 20–36 μm . From clogging of dust in a cleated wheel and from abrasive characteristics, grain sizes of <40 and <30 μm are inferred, respectively. The dust clinging to the wheel is quite

dark, with a specular reflectance of about 0.17. Abrasion was most pronounced on the softest metal samples (aluminum), and there are some indications that the dust may have a hardness similar to that of the platinum samples. The Martian soil abraded metal samples similarly to laboratory abrasion from a fine-grained artificial Martian soil simulant. Depth-of-dig data show that in some places the digging gets more difficult at a depth of about 1–2 cm, perhaps indicating a harder, compacted material covered with about 1–2 cm of fluffier dust.

References

- Chemical Rubber Company, *CRC Handbook of Chemistry and Physics*, 43rd ed., Cleveland, Ohio, 1961.
- Ferguson, D. C., The Wheel Abrasion Experiment—How abrasive is the Martian dust?, *Proc. Intersoc. Energy Conversion Eng. Conf.*, 32nd, 734–737, 1997.
- Gaier, J. R., and M. E. Perez-Davis, Effect of particle size of Martian dust on the degradation of photovoltaic cell performance, *NASA Tech. Memo.*, TM 105232, 1991.
- Haberle, R. M., and R. Greeley, Sand and dust on Mars, *NASA Conf. Publ.*, CP 10074, 36–39, Feb. 1991.
- Hepp, A. F., N. S. Fatemi, D. M. Wilt, D. C. Ferguson, R. W. Hoffman, M. M. Hill, and A. E. Kaloyerous, Wheel Abrasion Experiment metals selection for Mars Pathfinder mission, *NASA Tech. Memo.*, TM 107378, 1996.
- Hillard, G. B., and J. C. Kolecki, The interaction of high voltage systems with the environments of the Moon and Mars, *NASA Tech. Memo.*, TM 106107, AIAA-93-0704, Jan. 1993.
- Jenkins, P. P., G. A. Landis, and L. G. Oberle, Materials Adherence Experiment: Technology, *Proc. Intersoc. Energy Conversion Eng. Conf.*, 32nd, 728–731, 1997.
- Kolecki, J. C., and G. B. Hillard, Electrical and chemical interactions at Mars workshop, Final report, parts 1 and 2, *NASA Conf. Publ.*, CP 10093, Nov. 1991.
- Landis, G. A., P. P. Jenkins, and G. Hunter, Materials Adherence Experiment on Mars Pathfinder: Early results, *Proc. Intersoc. Energy Conversion Eng. Conf.*, 32nd, 732–733, 1997.
- Moore, H. J., R. E. Hutton, G. D. Clow, and C. R. Spitzer, Other Viking experiments and investigations: Physical properties of the surface materials at the Viking landing sites on Mars, *U.S. Geol. Surv. Prof. Pap.*, 1389, 117–118, 1987.
- Moore, H. J., D. B. Bickler, J. A. Crisp, H. J. Eisen, J. A. Gensler, A. F. C. Haldemann, J. R. Matijevic, F. Pavlics, and L. K. Reid, Soil-like deposits observed by Sojourner, the Pathfinder rover, *J. Geophys. Res.*, this issue.
- Rover Team, Characterization of the Martian surface deposits by the Mars Pathfinder rover, Sojourner, *Science*, 278, 1765, 1997.
- Siebert, M., Wheel Abrasion Experiment ground tests: Initial results, *Proc. Intersoc. Energy Conversion Eng. Conf.*, 32nd, 743–748, 1997.
- Siebert, M., and J. C. Kolecki, Electrostatic charging of the Pathfinder rover, paper AIAA 96-0486 presented at the 34th Aerospace Sciences Meeting and Exhibit, Am. Inst. of Aeronaut. and Astronaut., Reno, Nev., Jan. 15–18, 1996.
- Wilt, D. M., P. P. Jenkins, and D. A. Scheiman, Photodetector development for the Wheel Abrasion Experiment on the Sojourner microrover of the Mars Pathfinder Mission, *Proc. Intersoc. Energy Conversion Eng. Conf.*, 32nd, 738–742, 1997.

D. C. Ferguson, J. C. Kolecki, M. W. Siebert, and D. M. Wilt, NASA Lewis Research Center, MS 302-1, Cleveland, OH 44135. (e-mail: dale.c.ferguson@lerc.nasa.gov)

J. R. Matijevic, Jet Propulsion Laboratory, Pasadena, CA 91109.

(Received February 6, 1998; revised May 20, 1998; accepted June 15, 1998.)

The magnetic properties experiments on Mars Pathfinder

M. B. Madsen, S. F. Hviid, H. P. Gunnlaugsson, J. M. Knudsen, W. Goetz,
C. T. Pedersen, A. R. Dinesen, C. T. Mogensen, and M. Olsen

Niels Bohr Institute for Astronomy, Physics and Geophysics, Ørsted Laboratory, University of Copenhagen,
Copenhagen, Denmark

R. B. Hargraves

Department of Geological and Geophysical Sciences, Princeton University, Princeton, New Jersey

Abstract. The Mars Pathfinder lander carried two magnet arrays, each containing five small permanent magnets of varying strength. The magnet arrays were passively exposed to the wind borne dust on Mars. By the end of the Mars Pathfinder mission a bull's-eye pattern was visible on the four strongest magnets of the arrays showing the presence of magnetic dust particles. From the images we conclude that the dust suspended in the atmosphere is not solely single phase particles of hematite ($\alpha\text{-Fe}_2\text{O}_3$) and that single phase particles of the ferrimagnetic minerals maghemite ($\gamma\text{-Fe}_2\text{O}_3$) or magnetite (Fe_3O_4) are not present as free particles in any appreciable amount. The material on the strongest magnets seems to be indistinguishable from the bright surface material around the lander. From X-ray fluorescence it is known that the soil consists mainly of silicates. The element iron constitutes about 13% of the soil. The particles in the airborne dust seem to be composite, containing a few percent of a strongly magnetic component. We conclude that the magnetic phase present in the airborne dust particles is most likely maghemite. The particles thus appear to consist of silicate aggregates stained or cemented by ferric oxides, some of the stain and cement being maghemite. These results imply that Fe^{2+} ions were leached from the bedrock, and after passing through a state as free Fe^{2+} ions in liquid water, the Fe^{2+} was oxidized to Fe^{3+} and then precipitated. It cannot, however, be ruled out that the magnetic particles are titanomagnetite (or titanomaghemite) occurring in palagonite, having been inherited directly from the bedrock.

1. Introduction

This investigation was designed to detect magnetic dust particles, if such particles are present among those suspended in the Martian atmosphere, and to determine the nature of the magnetic phase responsible for the magnetic properties of such particles. In principle, the experiments are simple, utilizing a series of permanent magnets passively exposed to windblown particles suspended in the Martian atmosphere [Smith *et al.*, 1997a; Hviid *et al.*, 1997; Gunnlaugsson *et al.*, 1998]. The magnets were periodically viewed by the Imager for Mars Pathfinder (IMP), and the resulting images transmitted to Earth.

During the Viking mission (1976), two permanent Sm-Co magnets of different strength mounted on the backhoe of the surface sampler were immersed directly into the soil on the surface of Mars. The strong Viking magnet had a characteristic magnitude of the surface magnetic field $B = |\mathbf{B}|$ of 0.25 T and a surface field gradient (of the magnitude of \mathbf{B}), ∇B of magnitude 100 T m^{-1} . The corresponding numbers for the weak magnet were 0.07 T and 30 T m^{-1} . The Martian soil was found to adhere almost equally to the strong and the weak magnet at both landing sites. Furthermore, it was estimated that the particles in the soil on the Martian surface contain between 1% and 7% of a strongly magnetic phase, most probably a ferri-

magnetic ferric oxide intimately dispersed throughout the soil [Hargraves *et al.*, 1977, 1979].

An important observation was that both the weak and the strong backhoe magnets were essentially saturated with magnetic soil following the first insertion of the backhoes into the soil and they remained that way throughout the Viking mission. The results were the same for both landing sites. The limits for the spontaneous magnetization σ were given as

$$1 \text{ A m}^2(\text{kg soil})^{-1} < \sigma < 7 \text{ A m}^2(\text{kg soil})^{-1}.$$

Elemental analyses by means of an X-ray fluorescence spectrometer indicate a content of iron given as about 18% by weight of Fe_2O_3 in the Martian soil [Clark *et al.*, 1982].

In addition to the backhoe magnets (strong and weak), each Viking lander carried a reference test chart (RTC) magnet, which was passively exposed to the dust suspended in the Martian atmosphere. The RTC magnets were of the strong type only.

The backhoe magnets and the RTC magnets on the Viking landers were constructed as disc-shaped magnets of diameter 6.5 mm surrounded by a ring magnet of an outer diameter of 18.0 mm and an inner diameter of 13.0 mm. When assembled, the magnets resembled a “bull’s-eye.”

The pink sky on Mars has been attributed to the presence of reddish dust particles of the order of $1 \mu\text{m}$ in size [Tomasko *et al.*, this issue] and in an amount of 1–10 particles per cm^3 [Hargraves *et al.*, 1977; Pollack *et al.*, 1995].

Before the Viking mission, it was calculated (assuming nominal wind velocities of 5 m s^{-1} and an extraction efficiency of

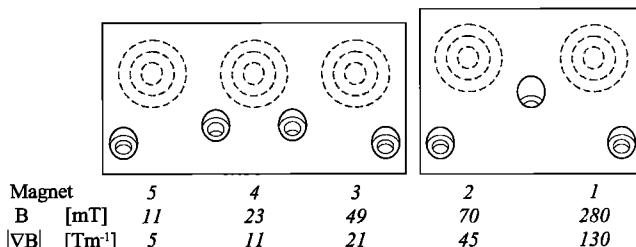


Figure 1. Front view of a magnet array. The position of the magnets below the surface of the magnesium block is indicated. The ring magnets have an outer diameter of 18 mm and an inner diameter of 13 mm, the cylindrical (disk) magnets have a diameter of 6.5 mm. The strongest magnet, magnet 1, is to the right. Representative values (cf. Figure 2) of the magnetic field B and the magnetic field gradient ∇B at the surface above the magnets are shown. The total length of the two blocks (plus their separation) is 147 mm. The mass of the instrument is 71 g. Four mounting holes are shown on the block containing the weak magnets, and three mounting holes on the block containing the strong magnets.

5%) that a minimum of 15 days would be required to accumulate a discernible layer ($\sim 10 \mu\text{m}$) of dust on the RTC magnets [Hargraves et al., 1977]. However, a bull's-eye pattern was visible on the RTC magnets immediately after landing at both landing sites. The magnetic particles thus attracted are assumed to have come from the dust cloud raised into the atmosphere by the retro-rocket exhausts when the spacecraft landed. A significant increase in the amount of material on the RTC magnets was noticeable following acquisition of samples by the soil sampler arm and their delivery to the analytical instruments aboard the landers [Hargraves et al., 1977].

Dust raised from the soil into the local atmosphere by the retro-rockets and by the sampling activity was thus considered to be a significant source of magnetic particles attracted to the RTC magnets.

2. Mars Pathfinder Magnets

As both the strong and the weak backhoe magnets on the Viking landers were saturated with dust throughout the mission, it was decided that the series of permanent magnets on the Mars Pathfinder lander should include magnets of lower strengths than the weakest Viking magnets.

The Pathfinder lander carried two magnet arrays (MAs) and one tip plate magnet (TPM). A detailed description of the construction and mounting of the magnets has been published [Gunnlaugsson et al., 1998]. Here follows a brief summary.

2.1. Magnet Arrays

The MAs on the Pathfinder lander are placed at a distance of 118 and 145 cm, respectively, from the IMP when the IMP is in the deployed position. The two MAs are identical. An MA consists of two blocks of magnesium, one block carrying two bull's-eye magnets (of Viking strengths) and another block carrying three magnets of lower and decreasing strengths [Gunnlaugsson et al., 1998]. To ensure electrical conductivity, the surface was coated with a thin layer ($\sim 0.5 \mu\text{m}$) of platinum. Electrostatic effects of charged dust grains arriving were minimized by an electrical connection (grounding) between the instruments and the body of the lander.

The shape and dimension of the $\text{Sm}_2\text{Co}_{17}$ permanent mag-

nets are illustrated in Figure 1, which shows a sketch of an MA. The ring magnets have an outer diameter of 18.0 mm and an inner diameter of 13.0 mm, and the cylindrical disk magnets have a diameter of 6.5 mm (like the Viking magnets). The ring magnets and center magnets are magnetized parallel to their symmetry axes but in opposite directions. Representative values of the magnitudes of the magnetic field B and the magnetic field gradient ∇B for each magnet are shown in Figure 1. Note the numbering of the magnets.

The detailed construction of the instruments is slightly more complicated than indicated in the illustrations; for example, the two weakest magnets are made as sandwiches of oppositely magnetized bull's-eye magnets [Gunnlaugsson et al., 1998].

Figure 2 shows the surface magnetic field B and magnetic field gradient ∇B for the magnets of an MA. Because of the cylindrical symmetry, we show the r and z components of both fields. The r component and the z component of the field gradient are designated f_r and f_z , respectively. The z components are normal to the surface of the instrument, and the r components are perpendicular to the z components. The origin of the coordinate system for each magnet is where the surface of the instrument cuts the symmetry axis of the concentric magnet system.

The dust attracted by the magnets was imaged through the 12 optical filters of the IMP, and the images were transmitted to Earth. These images constitute the data on which conclusions concerning the magnetic properties of the dust suspended in the Martian atmosphere will be based.

The lower of the MAs is situated at a height of about 40 cm above the Martian surface. It may thus be able to attract saltating grains if such grains exist. The upper MA (~ 75 cm above the Martian surface) can attract only magnetic particles suspended in the atmosphere. If the Pathfinder lander is horizontal, the MAs are mounted in such a way that their active surfaces have a tilt angle of 30° relative to the horizontal plane.

2.2. Tip Plate Magnet

The TPM consists of one bull's-eye magnet embedded in a magnesium structure, coated with a thin layer of platinum. The TPM is placed about 7 cm from the camera eye, and the magnet is imaged through a diopter lens in the filter wheel of the right eye of the IMP. The mounting allows imaging of the dust on the magnet with a high resolution (~ 140 pixels per 18 mm corresponding to $0.13 \text{ mm per pixel}$). The TPM is about 1.4 m above the surface of Mars when the IMP is in deployed position.

The TPM is constructed in such a way that the magnetic field B and the magnetic field gradient ∇B have a strong variation across the surface of the magnet. Figure 3 is a sketch showing the design of the TPM. A strongly varying magnetic strength across the surface of the magnet is obtained by mounting the bull's-eye magnet below a wedged surface with a tilt of 7° and by translating the inner disc magnet 0.9 mm relative to the center of the ring magnet.

Figure 4 shows a contour plot of the magnetic field strength and the component of the magnetic field gradient perpendicular to the surface of the TPM. Five marker points define a local coordinate system in which the magnetic field can conveniently be mapped. The magnesium surface above the magnet is thinnest where the double marker is, and consequently, the magnetic field is highest here (170 mT). The vertical component of the magnetic field gradient on the TPM varies from

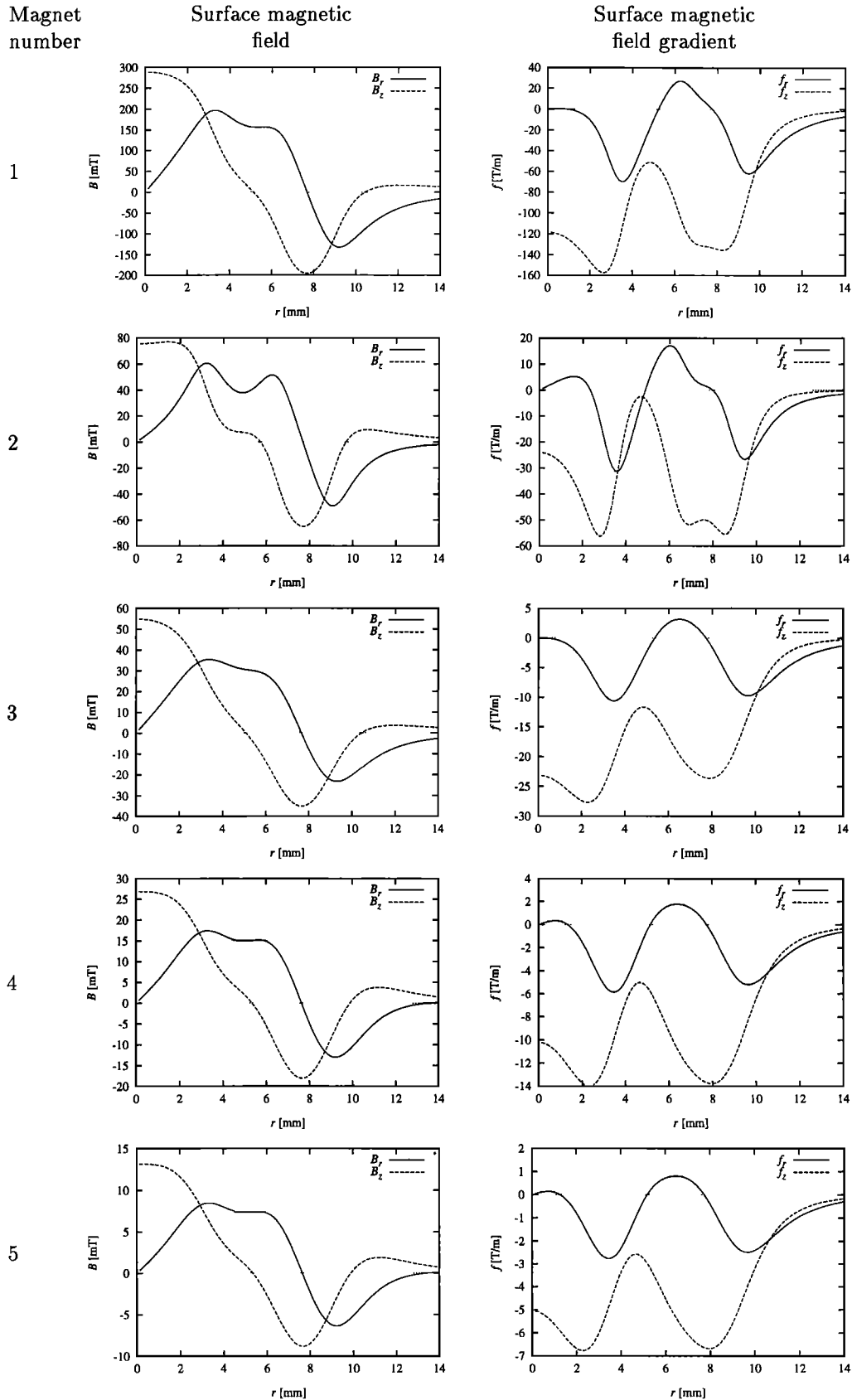


Figure 2. Surface magnetic field and magnetic field gradient for the five magnets of a magnet array. Because of the cylindrical symmetry, the r and z components of the fields are shown. The r and z components of the magnetic field gradient are denoted f_r and f_z , respectively. The origin of the coordinate system for each magnet is where the surface of the instrument cuts the symmetry axis of the concentric system of magnets. The z axis is perpendicular to the surface of the array.

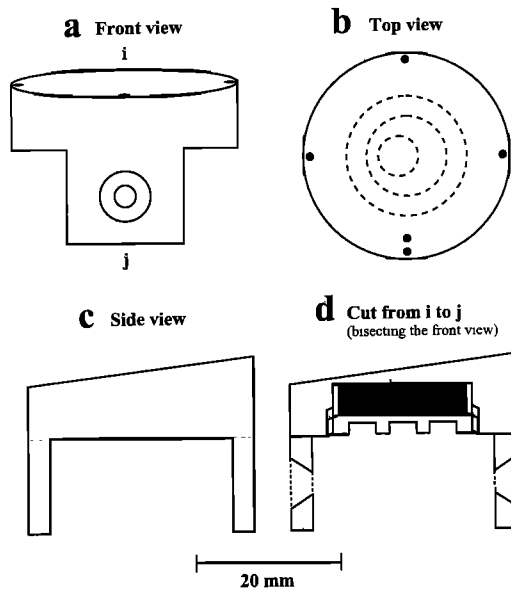


Figure 3. The tip plate magnet. The magnet is mounted below a wedged surface in a block of magnesium metal. In this way, a variation of the magnetic field \mathbf{B} and the field gradient $\nabla\mathbf{B}$ at the surface is achieved. (a) The circles in the rectangular extension toward the bottom show the position of holes for the mounting screws. (b) This top view shows the “active” surface of the instrument. The dotted lines indicate the position of the magnet assembly below the surface, and the five marker points define a local coordinate system on the surface. (c, d) This side view shows how the instrument is assembled. The magnesium surface above the magnet is thinnest where the double marker is, and consequently, the magnetic strength is highest here ($B = 170$ mT, $\nabla B = 130$ T m $^{-1}$).

approximately 130 T m $^{-1}$ to 12 T m $^{-1}$, which is the interval covered by the four strongest magnets in the MAS.

3. Preparatory Studies

The goal of the magnetic properties experiment is to determine the specific saturation magnetization σ_s of the particles sticking to the various magnets on Mars and, if possible, to identify the mineral, or minerals, responsible for the magnetization of the dust suspended in the Martian atmosphere.

The capture of airborne magnetic particles by permanent magnets is a complicated process depending on several parameters: (1) the force on the magnetized particle in the magnetic field provided by the permanent magnets, (2) the effective coefficient of friction between the particle and the platinum-coated surface of the magnet arrays, (3) the force of gravity on the particle, and (4) the wind velocity, i.e., the velocity by which the particle arrives on the magnetic target.

3.1. Theory

The force \mathbf{F} on a magnetized particle in a magnetic field is given by

$$\mathbf{F} = -\nabla U,$$

where U is the potential energy of the particle in the magnetic field \mathbf{B} . Let the particle have the mass m and the specific magnetization σ . The magnetization will, in general, depend on the impressed magnetic field \mathbf{B} . If the particle is able to

rotate in the magnetic field, and if the rotational energy of the particle can be quickly dissipated by friction, the magnetization vector of the particle will align itself parallel to the external field. In the following discussion, we assume that the specific magnetization σ remains at all times parallel to the magnetic field \mathbf{B} . This will, at least approximately, be true for particles captured by the magnets from the Martian atmosphere.

To calculate the energy of the particle in the magnetic field, we need to know the analytical expression for the magnetization curve $\sigma(B)$. In the Pathfinder mission a measurement of $\sigma(B)$ for the magnetic minerals on Mars is impossible. Approximations, and some guesswork, are necessary. We start by considering two limiting cases.

1. For single-domain particles or particles in large magnetic fields (above about 250 mT), the particles are nearly saturated magnetically. This means

$$\sigma(B) = \sigma_s,$$

where σ_s is the saturation magnetization. Then

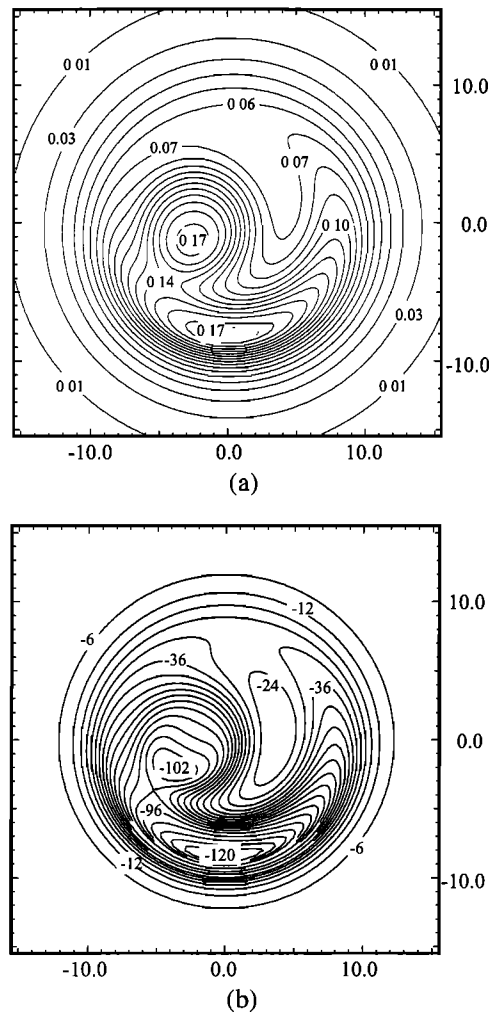


Figure 4. Contour plots of (a) the magnetic field B (T) at the surface of the TPM and (b) the z component of the magnetic field gradient ∇B (T m $^{-1}$). Note that the magnet is closest to the surface of the TPM structure toward the bottom in these figures corresponding to the double marker points on the outer surface of the instrument. The labels on the axes are in millimeters.

$$U = -m\sigma_s B, \quad (1)$$

which implies

$$\mathbf{F} = m\sigma_s \nabla B. \quad (2)$$

The force on the particle is proportional to the gradient of the magnitude of the magnetic field. For particles with the same value of $m\sigma_s$, the ability of the five magnets in the MA to hold magnetic particles is then proportional to the average magnitude of ∇B on a given magnet.

2. For small magnetic fields (< 1 mT),

$$M = \rho\sigma = \chi_i \frac{B}{\mu_0},$$

M = magnetic moment per volume ($A\ m^2/m^3 = A/m$), ρ is density (kg/m^3), $\mu_0 = 4\pi \times 10^{-7}$ (V s)/(A m), and χ_i is volume magnetic susceptibility (dimensionless). We have

$$\sigma = \frac{\chi_i}{\rho} \frac{B}{\mu_0} = \kappa_i \frac{B}{\mu_0}, \quad (3)$$

where κ_i is the specific magnetic susceptibility (m^3/kg).

The magnetic susceptibilities are not corrected for the demagnetization field. The B field (the magnetic induction) is the applied (vacuum) field. When M is proportional to B , the force on a particle is proportional to the product of the magnetic field and the magnetic field gradient:

$$\mathbf{F} = \frac{m\kappa_i}{\mu_0} B \nabla B = m\sigma \nabla B. \quad (4)$$

The values for κ_i , which for a given mineral may be found in various works on geophysics, are values obtained in low magnetic fields, i.e., $B < 1$ mT.

In the next section, we shall see that in a rough approximation we may assume that the magnetization is linearly dependent on the impressed magnetic field up to about 70 mT, which is the maximum of the field on magnet 2 of the arrays. Magnets 3, 4, and 5 all have lower surface fields (see Figure 1).

Assuming the validity of (4), the force on a magnetic particle is proportional to the product of the magnetic field and the magnetic field gradient. For particles with the same value of m and κ_i , the relative strength of the magnets may now, in a rough approximation based on the values shown in Figure 1, be given as

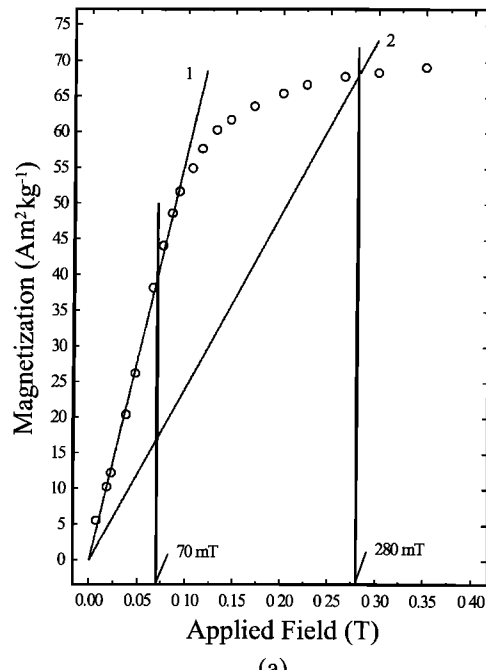
$$(B|\nabla B|)_1 : (B|\nabla B|)_2 : (B|\nabla B|)_3 : (B|\nabla B|)_4 : (B|\nabla B|)_5 \\ = 100 : 9 : 3 : 0.7 : 0.2.$$

It is, however, evident that the ability to capture a given particle is dependent not only on the magnetic field above the magnet, but also on the properties of the particle.

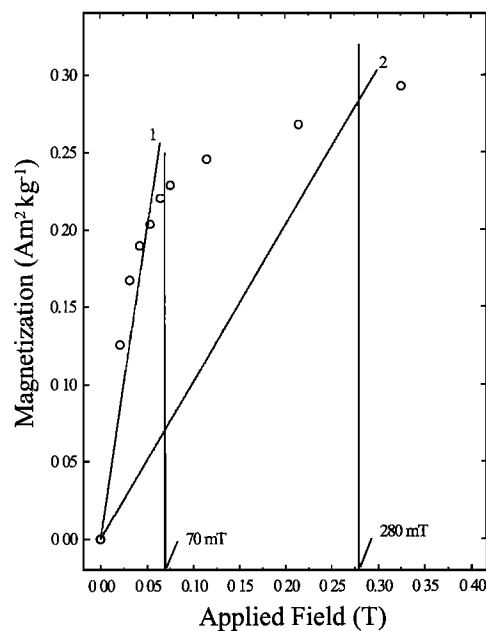
We shall proceed by considering the magnetization curves for two pertinent minerals, maghemite ($\gamma\text{-Fe}_2\text{O}_3$) and hematite ($\alpha\text{-Fe}_2\text{O}_3$). The minerals used for this study were high-grade analytical products in the form of powders obtained from Ventron, Karlsruhe, and Ferroperm, Denmark. The behavior of magnetite (Fe_3O_4) is similar to that of maghemite, except for the fact that the values of the saturation magnetization are different. For maghemite, $\sigma_s = 70 \text{ A m}^2 \text{ kg}^{-1}$; for magnetite, $\sigma_s = 92 \text{ A m}^2 \text{ kg}^{-1}$.

3.2. Magnetization Curves

In order to calculate the force on a magnetic particle in a magnetic field, we need to know the magnetization σ of the



(a)



(b)

Figure 5. Specific magnetization σ as a function of the impressed magnetic field B for (a) maghemite and (b) hematite.

particle in the given field. Figure 5 shows the magnetization σ as function of the impressed magnetic field B for maghemite ($\gamma\text{-Fe}_2\text{O}_3$) and hematite ($\alpha\text{-Fe}_2\text{O}_3$).

Let us start by presenting some qualitative remarks concerning the magnetization curves. The strongest field B due to magnet 1 of the MA is 280 mT. Maghemite is close to saturation for a field of 280 mT. The strongest field from magnet 2 is 70 mT. This is (nearly) within the “linear” part of the magnetization curve.

By inspection of Figure 5, we may conclude that

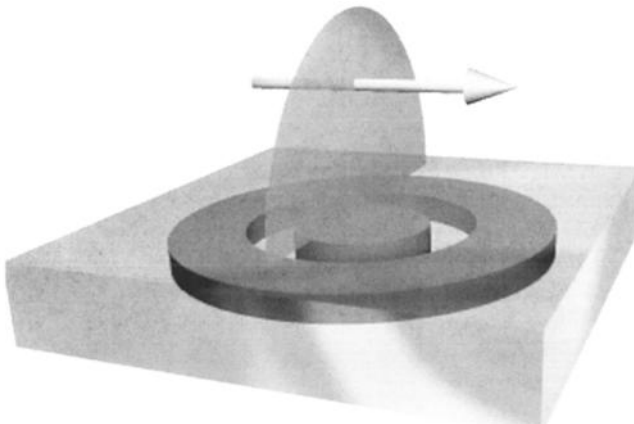


Figure 6. Definition of capture cross section of a given magnet of the arrays. P is a plane perpendicular to the surface of the magnet and containing the center of the cylindrical magnet. The capture cross section Σ (see text) of a given magnet is that area of the plane P where the magnetic force on the particle is equal to or larger than the gravitational force on the particle ($B|\nabla B| \geq g_M\mu_0/\kappa_i$; see the text). The arrow represents the velocity of the wind, v .

$$\sigma = \kappa_i \frac{B}{\mu_0}$$

is a rather good approximation for the magnetization of maghemite in the fields of magnets 2–5 if κ_i is properly selected. The value of κ_i for the lines marked 1 and 2 on Figure 5 is $\kappa_i = 7.2 \times 10^{-4}$ and $3.1 \times 10^{-4} \text{ m}^3 \text{ kg}^{-1}$, respectively. As previously stated, in order to be able to give a rough comparison of the ability of the magnets to capture magnetic grains suspended in the atmosphere, we have to choose an approximation. For the case of maghemite, we chose to use a value of κ_i given by the average value, i.e., $\kappa_i = 5.2 \times 10^{-4} \text{ m}^3 \text{ kg}^{-1}$. Based on a similar analysis for hematite, we chose the value $\kappa_i = 0.03 \times 10^{-4} \text{ m}^3 \text{ kg}^{-1}$.

For maghemite, some variability in the saturation magnetization has been reported. This variability can be attributed to internal defects and to spin canting in small particles ($d \ll 1 \mu\text{m}$). Therefore the value of saturation magnetization of maghemite depends on the mode of preparation and the resulting particle size and defect structure. The commercial maghemite used here as a reference is not affected by these effects. If, what seems to be highly probable, the maghemite component in the dust grains on Mars is microcrystalline, this maghemite may have values of saturation magnetization down to $50 \text{ A m}^2 \text{ kg}^{-1}$.

3.3. Relative Capture Cross Sections of the Magnets

As mentioned above, the process of the capture of magnetic particles by the permanent magnets depends on both the magnetic and mechanical properties of the dust particles. For reference purposes, we shall begin by comparing the magnetic force F_m acting on a particle to the corresponding gravitational force F_{g_M} [Gunnlaugsson, 1997].

Let the acceleration due to gravity on Mars be g_M ($g_M = 3.7 \text{ m s}^{-2}$). We then have

$$\frac{F_m}{F_{g_M}} = \frac{\kappa_i B |\nabla B|}{\mu_0 g_M}.$$

The force due to the magnetization will dominate the force due to gravity if

$$B |\nabla B| > \frac{g_M \mu_0}{\kappa_i} = \lambda.$$

Based on these considerations, we define the capture cross section of a given magnet in the following, rather arbitrary, way. Consider a plane normal to the surface of the MA and containing the center of the cylindrical (disc) magnet (see Figure 6). Owing to the cylindrical symmetry, we may choose the plane as being perpendicular to the projection of the wind velocity. We choose to define the capture cross section Σ_λ of a given magnet as that part (area) of the plane perpendicular to the magnet for which

$$B |\nabla B| \geq \frac{g_M \mu_0}{\kappa_i} = \lambda.$$

The dimension of λ is $\text{T}^2 \text{ m}^{-1}$. From this definition, it is possible to compare the capability of the various magnets to capture airborne particles for different values of the parameter λ . Using the values of κ_i stated above, we find for maghemite

$$\lambda = \frac{g_M \mu_0}{\kappa_i} = 0.009 \text{ T}^2 \text{ m}^{-1} \approx 0.01 \text{ T}^2 \text{ m}^{-1},$$

and for hematite

$$\lambda = \frac{g_M \mu_0}{\kappa_i} = 1.56 \text{ T}^2 \text{ m}^{-1} \approx 1.6 \text{ T}^2 \text{ m}^{-1}.$$

In addition to maghemite and hematite, we have calculated the capture cross section for an intermediate value of the parameter λ , $\lambda = 0.1 \text{ T}^2 \text{ m}^{-1}$ corresponding, for example, to composite particles. Table 1a shows the results of the calculations.

Note that hematite will stick at most to the two strongest magnets, i.e., magnets 1 and 2. For magnet 2 the capture cross section for maghemite is a factor of $107/5 \sim 21$ higher than the capture cross section for hematite.

It should be clearly understood that the numbers given in Table 1a are useful only for determining the relative capture cross section of the magnets for the various values of $\lambda = g_M \mu_0 / \kappa_i$. The absolute ability to attract airborne dust particles will be influenced by, for example, the direction of the wind relative to the active surface of the instruments and the wind speed, i.e., the velocity by which the particles arrive at the array.

If, for each value of λ in Table 1a, the capture of material on the different magnets is compared to that of magnet 1, some interesting observations can be made. Table 1b shows the results of this alternative way of displaying the results of Table 1a.

Table 1a. Capture Cross Sections

Magnet	$\Sigma_{0.01}$	$\Sigma_{0.1}$	$\Sigma_{1.6}$
1	235	126	48
2	107	49	5
3	86	32	0
4	51	8	0
5	23	0	0

Only the relative values of the capture cross section are of significance, see the text. Values are in units of mm^2 .

Table 1b. Relative Capture Cross Sections

Fraction of Dust on Magnet Number	$\lambda = 0.01$	$\lambda = 0.1$	$\lambda = 1.6$
1/1	1.00	1.00	1.00
2/1	0.46	0.39	0.10
3/1	0.37	0.25	0.0
4/1	0.22	0.06	0.0
5/1	0.10	0.0	0.0

Relative capture of dust for the various magnets on a magnet array compared to that of magnet 1 for different values of λ ($T^2 m^{-1}$).

From Table 1b it is seen that for $\lambda = 0.01 T^2 m^{-1}$, corresponding to maghemite, there is a relatively even decrease of capture versus the number of the magnet: roughly 1/2, 1/3, 1/5, and 1/10 for each magnet compared to magnet 1, whereas for $\lambda = 1.6 T^2 m^{-1}$, corresponding to hematite, the amount captured on magnet 2 corresponds to the relative amount of maghemite that would be captured on magnet 5, reflecting a much more drastic decrease of capture versus the number of the magnet. For an intermediate value of λ the behavior is between that found for the limiting values of λ .

Hence the distribution of dust among the different magnets of the magnet array reflects the relative proportions of dust grains with a given value of effective saturation magnetization.

These observations are, as we shall see later, important for our interpretation that there is a distribution of magnetization among the dust particles captured by the MA and that the dust particles therefore must be composite particles, consisting mainly of silicates mixed with a few percent of maghemite.

A representation of the relative capture cross sections different from that given in Table 1b is displayed in Figure 7. This figure gives the capture cross section of a given magnet relative to the strongest magnet (number 1), and as function of the parameter $\lambda = g_M \mu_0 / \kappa_i$. By inspection of Figure 7, it is seen that hematite will be able to stick to the two strongest magnets.

3.4. Stability Criteria for a Magnetic Particle on the Magnet Array

When a magnet array is mounted on a horizontal surface, it has a tilt angle of 30° . The tilt of the Pathfinder lander on Mars is 2.7° . With the precision attainable in the determination of the saturation magnetization in mind, we shall use a tilt angle for the array of 30° , i.e., we neglect the small tilt of the lander.

We now proceed to calculate the stability of a particle on the surface of an MA. In these calculations, we assume that the stability of the particle is a result of a competition between the gravitational force and the magnetic force on the particle. Later on, we shall discuss problems related to this model for the stability of a given grain on the arrays.

Consider a magnetic grain placed at a point on the magnet array where there is no magnetic field; the grain may be removed by the gravitational force if disturbed by a light wind or a colliding airborne particle. The influence of a light wind ($\sim 1-5 m s^{-1}$) is mainly to provide a slight lifting force, which can be considered as a reduction of the effective coefficient of friction μ .

When a magnetic grain has come to rest at a given point on the magnet array (see Figure 8a), there are several conditions for stability. Consider as an illustration the stability of a particle on a line along the surface of the array as indicated in Figure 8b (the line is marked 1). On line 1 in Figure 8b the condition for stability is given by (where the sign of f_r varies)

$$\mu(mg \cos 30^\circ + m\sigma|f_z|) \geq m(g \sin 30^\circ + \sigma f_r).$$

Here μ is the coefficient of friction between the grain and the platinum-coated surface of the MA. The coefficient of friction is dependent not only on the slightly roughened surface of the array, but also on the nature of the particle (size, shape, and texture).

The results of computer simulations taking into account the conditions for stability on the whole surface (i.e., with the azimuth dependence of the influence of f_r included) is shown in Figure 10.

In the calculations of the conditions for stability of the grains

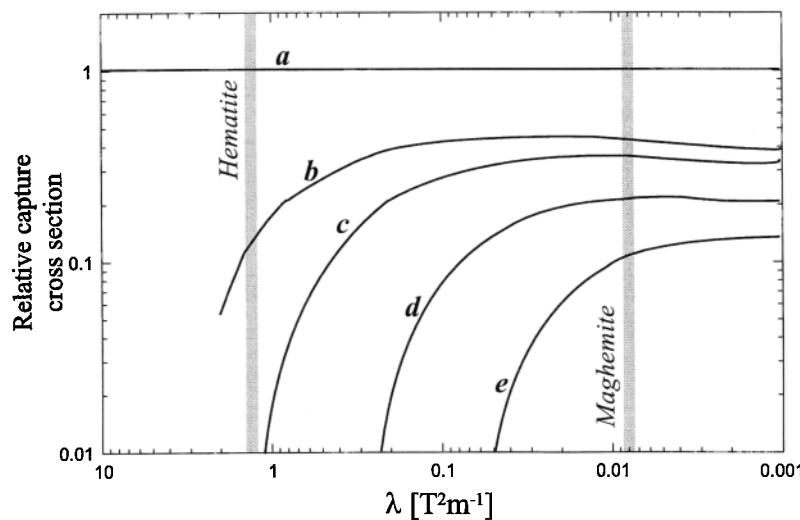


Figure 7. Graph of relative capture cross sections as function of the parameter λ for the various magnets (relative to magnet 1). Curve b represents the ratio $\Sigma_{\text{magnet}_2} / \Sigma_{\text{magnet}_1}$. Analogous representations hold for curves c, d, and e. The values of the parameter λ for the minerals maghemite and hematite are indicated.

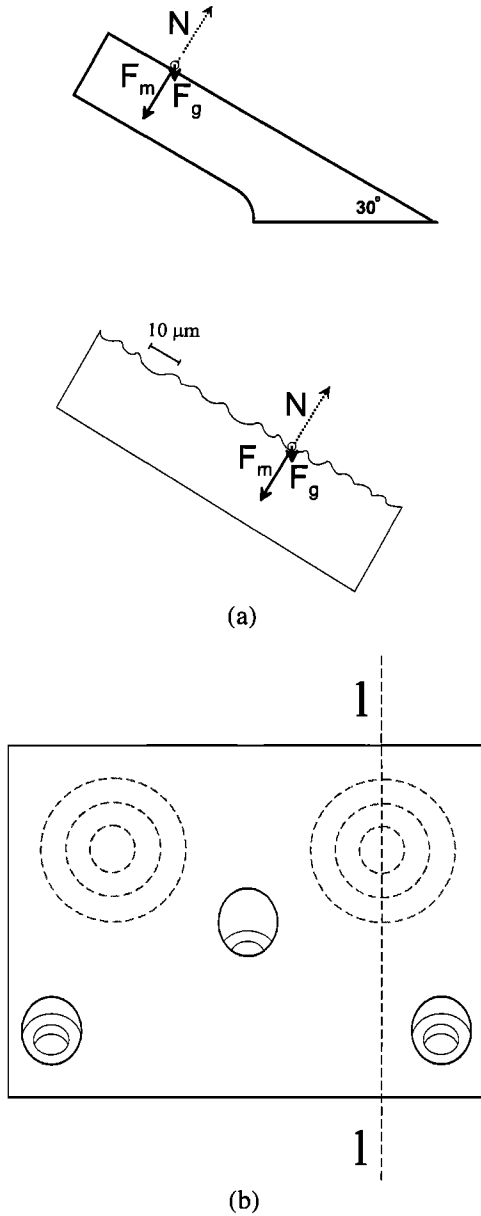


Figure 8. Stability of a magnetic particle on a magnet array. (a) The magnet arrays are mounted in such a way that when the Pathfinder lander is horizontal, the imaged surface of the array is tilted 30° with respect to the horizontal plane. Note that if the size of the particles is less than the characteristic scale of roughness of the platinum-coated surface, the action of gravity, and the effective coefficient of friction, varies drastically. (b) Line on the surface along which stability is described in the text.

on the array, we have used a more detailed model for the function $\sigma = \sigma(B)$ than the (linear) model used for the calculations of the relative capture cross sections (Table 1b and Figure 7).

One of the most important characteristics of the magnetization curve is how fast the curve rises as a function of the applied field and, specifically, how high a value of the applied field is necessary to reach the saturation magnetization.

Characteristic values of the magnetic field B on the weakest and the strongest magnet of the arrays are 11 and 280 mT, respectively. It is therefore sufficient to find an expression $\sigma =$

$\sigma(B)$ for fields larger than 10 mT, and the behavior of $\sigma = \sigma(B)$ for $B > 300$ mT is not relevant for the magnetic properties experiment on Mars Pathfinder.

As a rough empirical formula for $\sigma = \sigma(B)$, we have chosen the following:

$$\sigma = \frac{\sigma_0 B}{\gamma + B}. \quad (5)$$

Here γ is the value of the magnetic field B , where σ has reached half the value of σ_s . The magnetic field γ is thus an empirical parameter that must be determined for each given sample. The parameter γ describes how steeply the magnetization curve grows with the impressed field B . For maghemite (and magnetite) the value of γ is ≈ 50 mT, and for hematite, $\gamma \approx 90$ mT. A description of the validity of the model used is given by Gunnlaugsson *et al.* [1998].

Figure 9 shows the magnetization curve of three selected samples. Two of the samples are basaltic sands from Iceland, and one is thermally decomposed ochre [Pedersen *et al.*, 1998]. Concerning the magnetic properties of the decomposed ochre, see also the section on thermally decomposed ochre below. The solid curves correspond to the model given in (5).

The curve marked c in Figure 9 demonstrates that some samples cannot be described adequately for magnetic fields B higher than 300 mT. The reason in this case is that the sample contains a paramagnetic phase, the contribution of which is significant for $B > 300$ mT. The fitting is therefore limited to the interval of importance for the magnetic properties experiments on Mars.

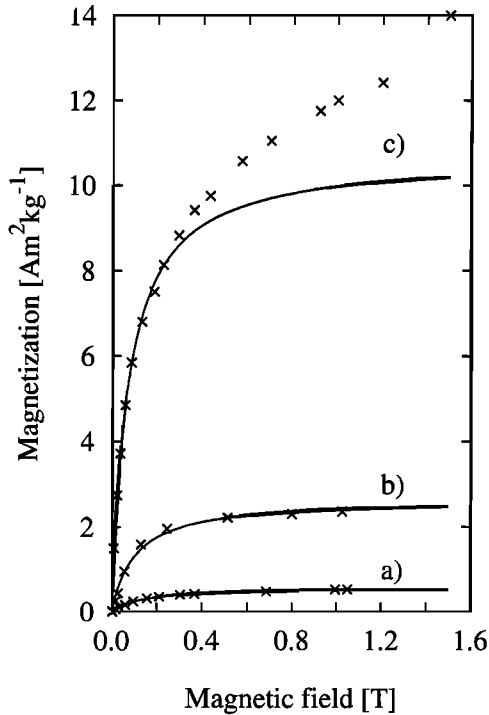


Figure 9. The curves marked a and b are the magnetization curves for magnetic separates from basaltic sand from Iceland. The crosses are measured values, and the solid lines represent fits to (5). The curve marked c is the magnetization curve of thermally decomposed ochre. Besides the ferrimagnetic component, the sample contains a paramagnetic compound. The fit has been restricted to $B < 0.3$ T.

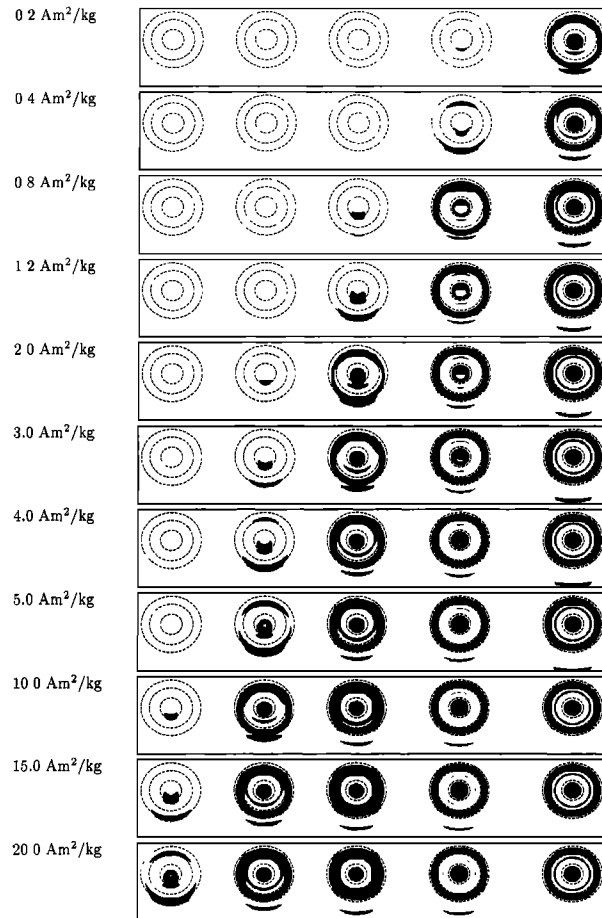
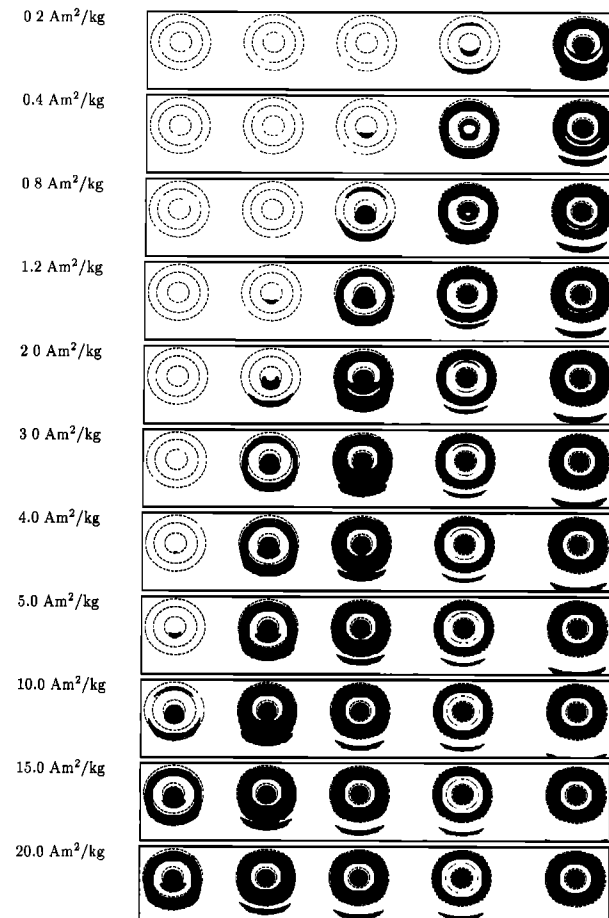
a. Pattern for $\mu = 0.2, \gamma = 50$ mTb. Pattern for $\mu = 0.3, \gamma = 50$ mT

Figure 10. Areas on the surface of the magnet array where magnetic particles are potentially stable. The calculations have been performed for various combinations of values of the saturation magnetization of the particle, σ_s , the parameter γ (see the text), and the effective coefficient of friction μ , as indicated in the figure. Note that the figure says nothing about the actual pattern that would be observed if the different capture cross sections for the different magnets were folded in (see the text).

Using the model described by (5), we have calculated the areas of the MA where a particle with a given value of σ_s and γ is stable. The calculations have been performed for various combinations of selected values of σ_s , γ , and μ .

Note that the effective coefficient of friction μ is, in general, different for different minerals, but μ is also strongly dependent on particle size and the surface roughness of the particles. It is not possible to determine μ . We have calculated the stability patterns for many values of μ , of which we have chosen to show the results for $\mu = 0.2$ and 0.3 .

Figure 10 shows the results for different selected values of σ_s , with four sets of parameters: $(\mu, \gamma) = (0.2, 50$ mT), $(0.3, 50$ mT), $(0.2, 90$ mT), and $(0.3, 90$ mT). From Figure 10 it is evident that both the value of μ and the value of γ influence the pattern strongly.

The images are useful in the sense that they demonstrate the condition where a particle is not stable, i.e., when a magnetized grain is not able to stick to a given magnet.

Consider, for example, hematite ($\sigma_s = 0.4$ A m²/kg and $\gamma \approx 90$ mT). If $\mu = 0.2$, hematite will essentially stick to magnet 1 only. For $\mu = 0.3$, hematite will stick also to magnet 2 but not to magnets 3, 4, or 5 (see also Figure 15b).

For the mineral maghemite, the parameter γ has a value of

about 50 mT, i.e. maghemite has a steep magnetization curve. As $\sigma_s \approx 70$ A m²/kg, it is evident that pure maghemite sticks to all five magnets (see also Figure 15a).

For composite particles, for instance, silicates containing a few percent of maghemite, the content of maghemite will determine the value of σ_s for a given particle. A particle of saturation magnetization $\sigma_s = 4$ A m²/kg will (for both $\mu = 0.2$ and 0.3), in principle, be stable on magnets 1–4 but not on magnet 5.

As previously mentioned, the wind has an influence on the patterns of dust on the magnets. Besides transporting the particles toward the magnets, the wind interacts with particles already on the magnets. During the development of the MAs for Mars Pathfinder, wind tunnel experiments were performed at NASA Ames Research Center, Mountain View, California. The wind tunnel is capable of operating at low air pressures (~ 10 mbar = 10 hPa). Among the conclusions from these experiments were that high wind speeds (> 20 m s⁻¹) were necessary for directly removing dust from the MAs. Typical wind speeds on Mars during the operation of Mars Pathfinder were below 5 m s⁻¹.

A dynamic process of significance for the accumulation of dust, and the formation of the pattern, is the following. As-

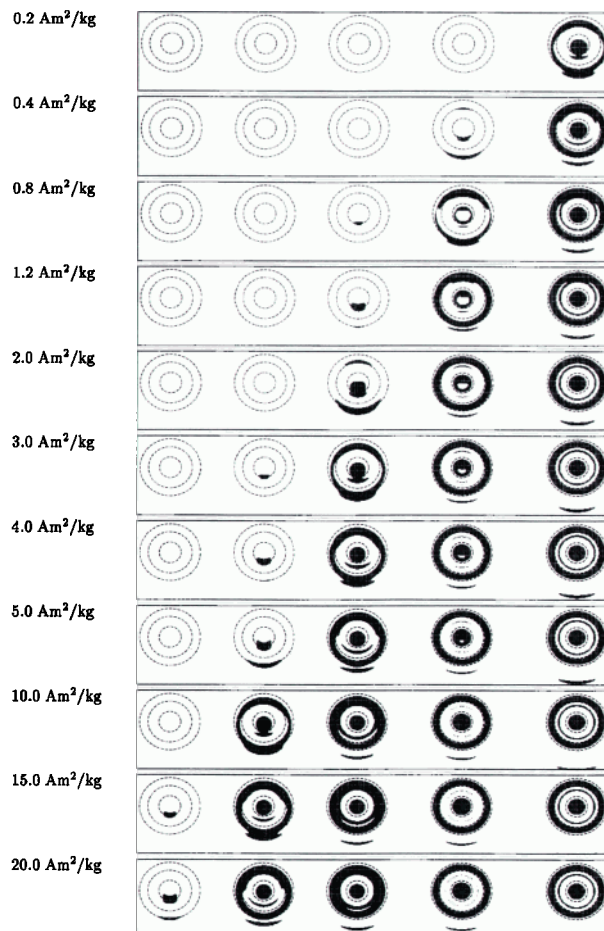
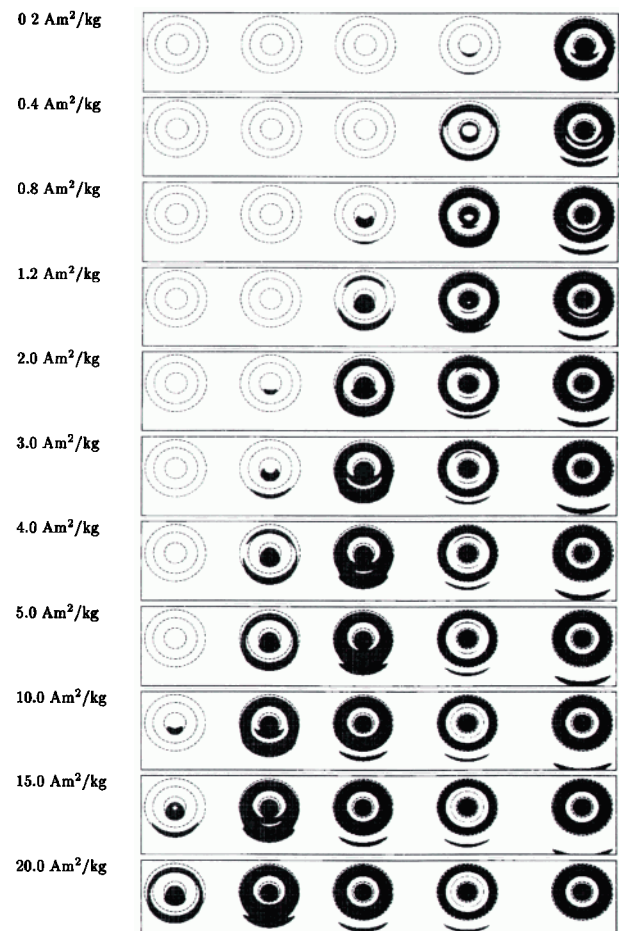
c. Pattern for $\mu = 0.2$, $\gamma = 90$ mTd. Pattern for $\mu = 0.3$, $\gamma = 90$ mT

Figure 10. (continued)

sume that a particle has come to rest on the surface of the MA. The particle is now hit by another arriving particle. This process may, helped by gravity, remove the first particle, while the arriving particle loses momentum in the collision and may thus be captured by the MA. Such processes appear to be as important as the gravitational field on Mars in itself and, for the moderate wind velocities encountered during the Pathfinder mission, certainly more important than the direct influence of the wind.

In conclusion, we state that for the formation of the pattern on the MAs, the wind is important mainly in the sense that it determines the velocity (and hence frequency) with which new particles are delivered to the surface of the array. The gravitational field provides a force that helps remove potentially unstable particles from the surface. However, to actually remove such particles, it is probably necessary that the wind carries new particles to the array. It is the collision with arriving particles that provides the action that removes a potentially unstable particle from the array. The shape of the pattern observed on the MAs is determined mainly by the magnetic forces on the particles. Figure 10 is useful due to the fact that it shows where on the MA a particle with a given magnetization will not be stable.

4. Magnetic Properties Experiments on Mars

4.1. Magnet Arrays

Figure 11 shows the upper magnet array imaged on various sols (1 sol = 1 Martian day = 24.6 hours). No dust could be seen on the magnets on sol 1. A bull's-eye pattern, testifying to adhering particles, was seen on the strongest magnet by sol 5. This pattern has strengthened with time. By sol 10, a pattern was visible on magnet 2. A pattern appeared also on magnet 3 (sol 21), and finally, on magnet 4 a pattern was visible on sol 68.

There are two possible sources of the magnetic particles

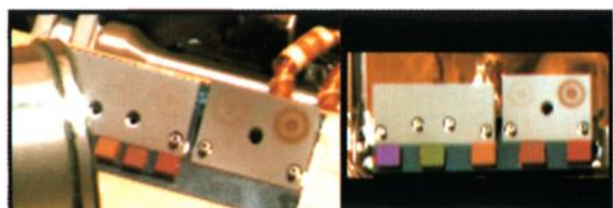


Plate 1. The two magnet arrays imaged on sol 80. The pictures are composed from the red-green-blue filters of the IMP (670, 530, and 440 nm).

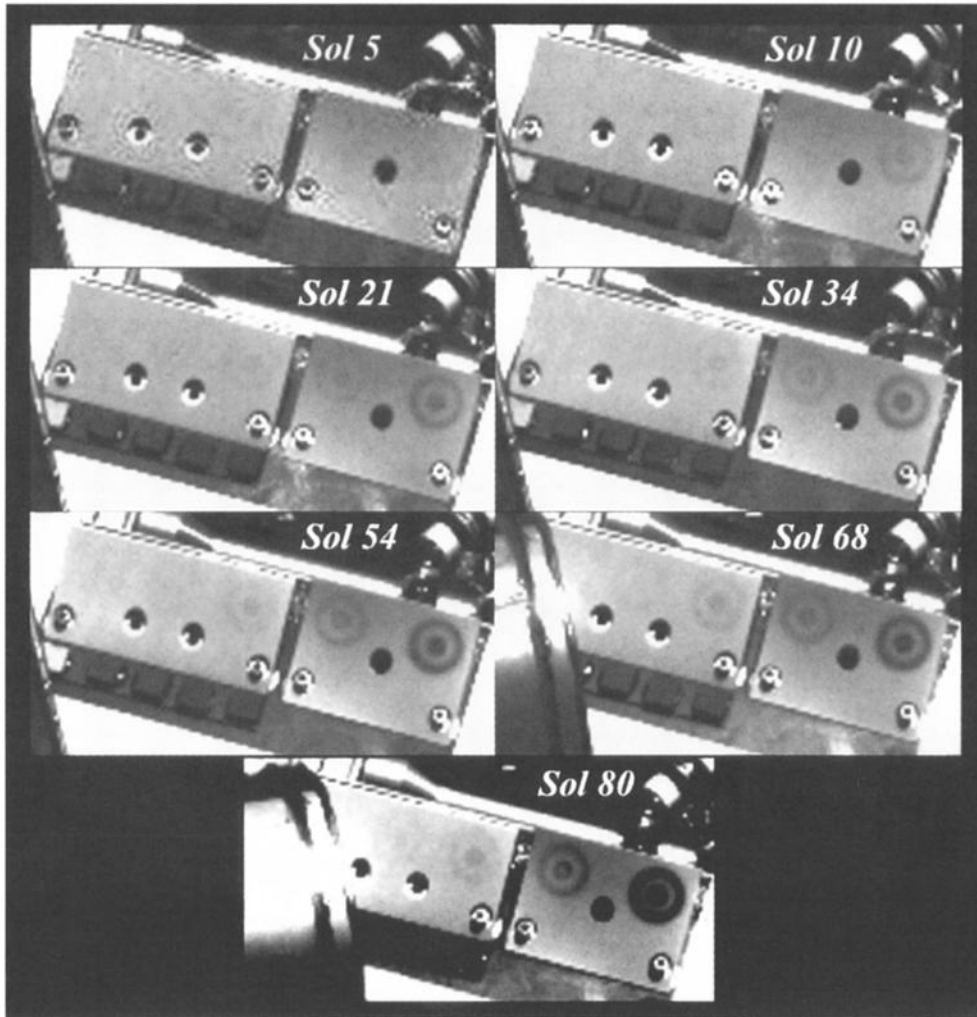


Figure 11. Dust collected on the upper magnet array at various sols as imaged through the 440-nm filter. The amount of dust on the magnets grows with time. The noise pattern visible on the sol 5 image is a result of the Joint Photographic Experts Group (JPEG) compression algorithm.

attracted to MAs: (1) dust elevated into the atmosphere during the landing of the spacecraft (compare with the discussion of the RTC magnet experiment on the Viking landers) and (2) dust particles normally suspended in the Martian atmosphere.

As a relatively clear bull's-eye pattern on the strong magnet did not appear until sol 5, we conclude that the dust attracted is from the particles normally suspended in the Martian atmosphere.

As shown in the series of pictures in Figure 11, the amount of dust on the magnets of the upper array has slowly increased during the mission. Comparing the images in Figure 11 with Figure 10, we conclude that only a few of the dust particles suspended in the atmosphere can have a magnetization above $10 \text{ A m}^2 \text{ kg}^{-1}$.

Figure 12 shows a series of pictures of the lower magnet array at various sols. The growth of the bull's-eye patterns is evident. By comparison with Figure 11, it is seen that the amount of dust on the lower array is less than that on the upper array. The reason for this may be that the lower array for certain wind directions is on the leeward side of the electronics box of the lander.

A major question related to the magnetic properties experiment is the following: Are the magnet arrays on Mars culling

a small subset of highly magnetic particles, or are most of the articles in the Martian atmosphere moderately magnetic? To elucidate this problem, we must briefly turn to other measurements of the atmosphere of Mars and the suspended dust particles.

4.2. Dust in the Martian Atmosphere

Wind speeds measured during the Pathfinder mission were generally less than 5 m s^{-1} [Schofield et al., 1997]. In the morning hours the wind speeds measured were sometimes even less than 1 m s^{-1} . The wind directions were mainly south-easterly, but the directions were variable [Schofield et al., 1997].

During the Pathfinder mission, the light scattering properties of the suspended particles were measured by the IMP team [Smith et al., 1997b]. The vertical optical depth was found to be about 0.5. The estimate for the average radius of the suspended particles given by Smith et al. is $1.6 \mu\text{m}$, with a distribution in size around this value. An average radius of $1.6 \mu\text{m}$ is a little less than the value of $1.85 \mu\text{m}$ given by J. B. Pollack and collaborators from the corresponding measurements during the Viking mission [Pollack et al., 1995]. Apart from the slightly different value of mean radius of the particles, there

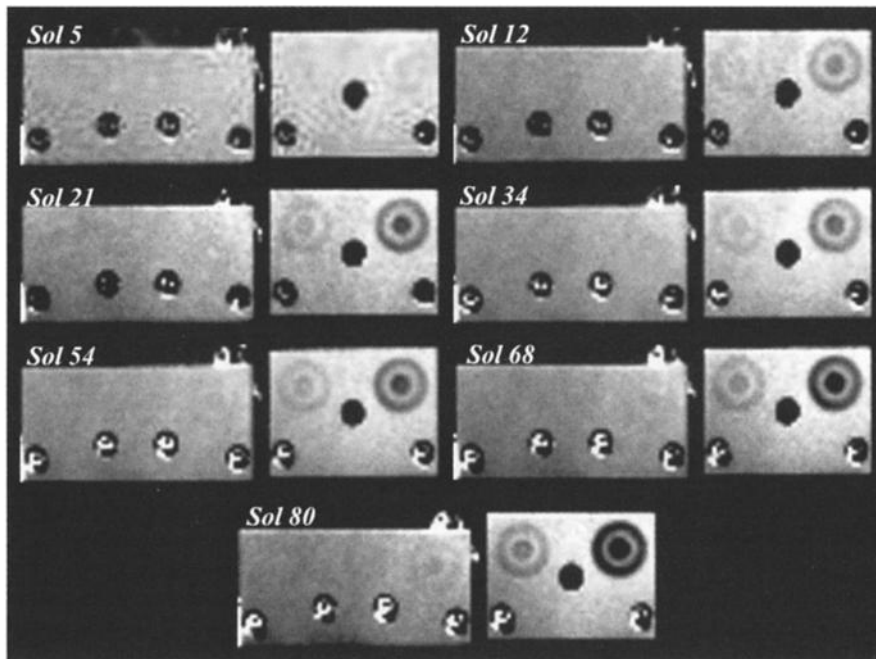


Figure 12. Dust collected on the lower magnet array at various sols as imaged through the 440-nm filter. As on the upper array, the amount of dust on the magnets grows with time.

are no major differences between the observations of Pathfinder and Viking with respect to the atmosphere.

Based on the results from the Pathfinder mission, and the Viking mission, it is impossible to give a quantitative answer to the essential question posed above: Are the magnet arrays on Pathfinder culling a small subset of highly magnetic particles? To present a rough estimate, which perhaps may be considered as no more than guesswork, we shall here use the results from studies on both the Viking mission and the Pathfinder mission to elucidate the problem.

As mentioned, during the Viking mission, two magnets were inserted directly into the soil, with the result that both magnets were saturated with magnetic dust from the beginning. It is thus certain that both the material on the surface and the dust suspended in the atmosphere are magnetic to some degree.

To decide if (nearly) all the particles suspended in the atmosphere are magnetic, we should calculate the number of sols required to accumulate a discernible layer of dust on the strongest magnet of the arrays on Pathfinder. This is not possible. We can at most give a rough estimate using the following crude model.

We assume a wind velocity of 3 m s^{-1} and a number density of particles of 1 cm^{-3} . Furthermore, we assume that each particle brought to the magnet will be held by the magnet. Per sol, the number of particles brought to an area of 1 cm^2 of the target is then approximately $300 \times 1 \times 10^5 \approx 3 \times 10^7$. If each particle has a linear dimension of $1 \mu\text{m}$, 10^8 particles are needed to cover 1 cm^2 completely. The time needed for covering the magnet with a discernible layer is thus of the order of a few sols.

As mentioned, a faint bull's-eye pattern could be seen with certainty on the strongest magnet on Mars on sol 5. On the screen of a monitor it was actually possible to discern a very feeble ring on sol 2. The result indicates that a major fraction of the particles suspended in the Martian atmosphere rather than a small subset are indeed somewhat magnetic. With the data at hand, it is impossible to reach a more firm conclusion.

4.3. Spectroscopy of the Dust on the Magnets

By the end of the mission, only the two strongest magnets, namely, magnets 1 and 2, had attracted sufficient dust to perform spectroscopic investigations. Plate 1 shows the two strongest magnets of the upper magnet array. The picture was composed from the red-green-blue filters of the IMP. The dust on the magnets is evidently reddish, and by inspection alone, there appears to be no difference between the dust on the two magnets of the upper array. Also there seems to be no difference between the dust on the strongest magnet of the upper and lower arrays. No saltating grains of a different appearance seem to have been attracted and kept by the lower array. This is in accordance with the low wind velocities reported.

A detailed interpretation of the reflection spectra of the dust on the magnets must be based on the radiative transfer equation for a two-layer system. The layers of dust on the magnets are so thin that diffuse reflection is obtained from both the dust and from the underlying, platinum-coated magnesium plate. For analysis, we have used the diffusive-reflectance approximation of a two-layer system as described by Hapke [1993, Figure 11.2, page 296].

Some of our preliminary results are shown in Figure 13, where the reflection spectrum of the dust on magnet 1 of the upper magnet array is shown. The curve (marked UM) for the dust on the MA represents the reflectivity relative to that of the bare platinum-coated surface, i.e., the platinum surface where no particles are magnetically attracted. For comparison, we show the spectra of a bright soil on the surface of Mars (the wind tail of Barnacle Bill, marked BS) and a darker soil (the northeast facing side of Mermaid Dune, marked DS) [Smith et al., 1997b]. The curves for the soil patches represent reflectivity relative to the reflectivity of the onboard calibration target. From Figure 13, we conclude that there are no major differences between the bright soil on the surface of Mars and the dust attracted by the strongest magnet.

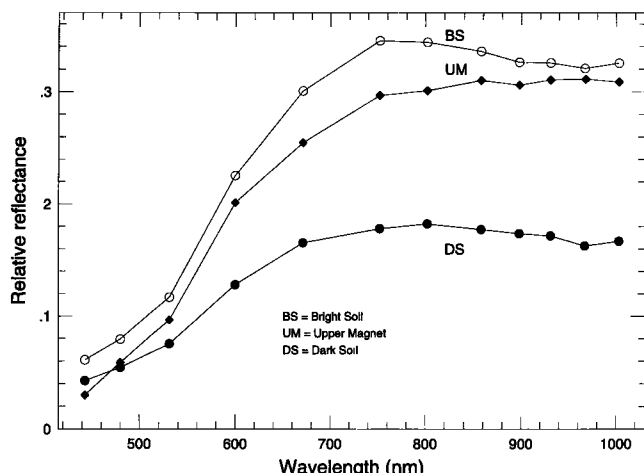


Figure 13. The reflection spectrum of the dust on magnet 1 of the upper magnet array (UM). For comparison, a spectrum of a bright soil on the surface of Mars (BS) and a darker soil (DS) is included.

The slight differences apparent on Figure 13 cannot at present be regarded as significant. We are attempting, using simulation experiments and calculations, to determine the thickness of the dust cover on the strongest magnets. As a preliminary conclusion, we state that the dust attracted by the magnets appears to be of the same (mineralogical) composition as the bright soils on the surface of the planet.

4.4. Tip Plate Magnet

Figure 14 shows the TPM imaged on sols 66 and 78. The amount of dust on the TPM has increased with time. On sol 78 it was possible to distinguish dust all along the circle above the ring magnet. The fact that the cylindrical (disc) magnet is displaced 0.9 mm from the center of the ring magnet can also be seen from the pattern of attracted dust.

Several features of the dust pattern should be emphasized. As noted, the variation of the magnetic strength along the

circle, i.e., the variation of the magnetic field gradient ∇B spans the variation from magnet 1 on the MAs to magnet 4. The fact that dust is visible all along the circle implies that the result of the TPM experiment confirms the results derived from the MA experiment.

The dust slowly settling on the rover material adherence experiment (MAE) target is found to cover the target area, resulting in 0.28% optical obscuration per day [Rover Team, 1997]. Dust is thus settling on all surfaces, including the TPM. Because dust is also delivered to the surface by the wind, some of the dust particles already present on a given surface may be removed by collision with arriving airborne particles, as discussed in a previous section.

The tilt of the surface of the TPM ($\sim 7^\circ$) is much less than the tilt of the MAs ($\sim 30^\circ$). If no magnetic field were present, the particles left on the surface of the TPM, by settling, would be stochastically distributed over the surface. This is evidently not the case. The magnetic fields above the magnet draw the arriving magnetic particles into the pattern now visible on the magnet. This is another confirmation that the magnetic force dominates other forces on the particles. It seems impossible to give a quantitative description of the capture process. For example, the electrically conductive surface of the TPM makes it difficult to make a direct comparison with the dust settling on the rover (MAE). Nonmagnetic dust grains settling on the TPM may not be stable. Qualitatively, the pattern seen on the TPM is consistent with the idea that the particles suspended in the atmosphere are drawn by the magnetic field into the pattern observed; hence most particles must be at least moderately magnetic.

5. Selected Simulation Experiments

5.1. Introduction

To support the theoretical considerations described above, we are performing laboratory simulation experiments. In this section we shall briefly describe a few selected results of such experiments.

In a terrestrial laboratory it is difficult to simulate the pro-

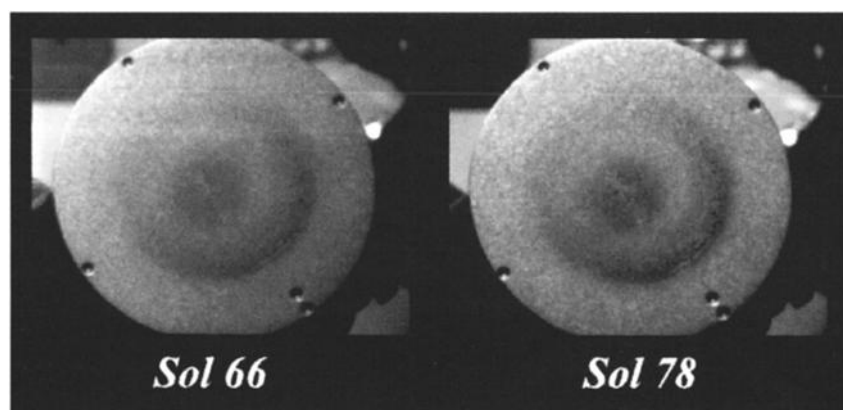


Figure 14. Dust collected on the tip plate magnet on sols 66 and 78. As the accumulation of dust progresses, the ring surrounding the central spot of dust approaches completion.

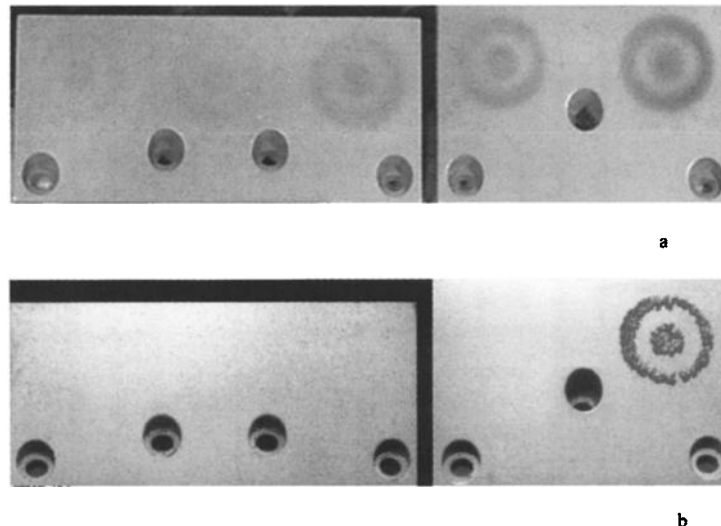


Figure 15. Pattern formed when (a) maghemite, $\gamma\text{-Fe}_2\text{O}_3$ is collected on the magnet array and (b) macroscopic hematite, $\alpha\text{-Fe}_2\text{O}_3$ is collected on the magnet array.

cess of the capture of magnetic particles by the MAs and the TPM on Mars. To deliver magnetic dust particles to an MA in the laboratory, we are, for the time being, restricted to using the following very simple setup.

An MA is placed inside a desiccator equipped with a small fan that can be driven at various speeds. The dust to be studied is introduced to the desiccator through a sieve and falls in front of the fan. When the fan is running, the dust particles are whirled around inside the desiccator. One is then able to observe how the bull's-eye pattern grows.

Figure 15 shows pictures of the minerals maghemite and hematite blown onto the MA in the manner described above. The surface of the array was tilted at an angle of 30° relative to the horizontal plane.

5.2. Thermally Decomposed Ochre

Ochre is a hydrated ferric oxide gel that is produced when Fe^{2+} dissolved in water is rapidly oxidized. The ochre used in this study was obtained from a water processing plant in Lejre, Denmark, and it is composed of ferrihydrite (approximate formula $\text{Fe}_2\text{O}_3 \times 9 \cdot \text{H}_2\text{O}$) with ~4% by weight of carbon and trace amounts of minor elements. The ferrihydrite was verified by X-ray diffraction to be of the two-line type [Pedersen et al., 1998]. The ochre as found is not magnetic (i.e., not ferrimagnetic). Dried ochre as found does not stick to any of the magnets on a magnet array.

A sample of ochre was heated in air at 500°C for 24 hours. Thermally decomposed ochre is not considered as a Mars sample analog because it does not have the elemental composition of the Martian dust and soils. Ochre is very fine grained,

and by heating it at various temperatures, one can control its magnetic properties. Ochre is thus useful as a magnetic analog to the dust on Mars.

Figure 16a shows the thermally decomposed ochre (500°C, 24 hours) blown onto an MA that was tilted 30° relative to the horizontal. The heated ochre sticks to four magnets, approximately as the dust on Mars sticks to the four strongest magnets.

We have measured the magnetization as function of the applied field B for the bulk sample of the decomposition product and for the dust sticking to the various magnets. In Figure 16b, we show the magnetization curves for the bulk sample and for the dust on magnets 2 and 4. The dust on magnet 2 has a saturation magnetization approximately 2 times the saturation magnetization of the bulk sample. The dust on magnet 4 is about 3 times as magnetic as the bulk sample.

Particles created by the thermal decomposition of the ochre are evidently magnetic. The particles must be composite, containing varying amounts of a strongly magnetic mineral. Each magnet has picked out a subset of magnetic particles. The weaker magnets have attracted preferentially the stronger magnetic grains, whereas the stronger magnets have attracted particles with a broader range of values of magnetization. In other words, the magnets are "filtering" the grains according to their magnetization. In fact, apart from pure chemicals, we have rarely seen a sample that was not partly separated in this way.

What is the mineral responsible for the magnetization of the decomposed ochre? Figure 16c shows Mössbauer spectra of the thermally decomposed ochre in the bulk sample and the dust recovered from magnets 2 and 4. The spectra were ob-

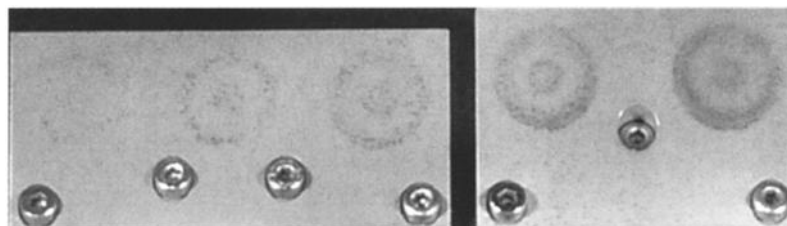


Figure 16a. Pattern formed when thermally decomposed ochre is collected on the magnet array.

tained at room temperature. The central doublet has an isomer shift (relative to metallic iron at room temperature) of 0.34 mm s^{-1} and a quadrupole splitting of 0.90 mm s^{-1} . The sextet has a magnetic hyperfine field of 49.6 T , an isomer shift of 0.33 mm s^{-1} , and a quadrupole shift of $\sim 0.0 \text{ mm s}^{-1}$, corresponding to the mineral maghemite ($\gamma\text{-Fe}_2\text{O}_3$). The relative spectral area of the sextet is 9%, 17%, and 23% for the bulk sample and the dust recovered from magnets 2 and 4, respectively.

Figure 16c shows that at least two phases are present. It is evident from the spectral areas that the content of maghemite relative to the compound corresponding to the central doublet increases as we go from the stronger to the weaker magnets. It is therefore clear that the particles in the bulk sample and the particles sticking to the magnets are composite. This is a confirmation of the fact that the magnets have sorted the grains according to their content of maghemite.

A detailed study of the thermal decomposition of ochre (ferrihydrite) is in itself an extensive project. Here we have paid attention to those aspects of the process that are of importance for the interpretation of the magnetic properties experiments on Mars Pathfinder.

The saturation magnetization of the bulk sample of the thermally decomposed ochre is $\sigma_s = 7 \text{ A m}^2 \text{ kg}^{-1}$. The dust on magnet 2 has a saturation magnetization of $\sigma_s = 13 \text{ A m}^2 \text{ kg}^{-1}$, and the dust on magnet 4 has $\sigma_s = 19 \text{ A m}^2 \text{ kg}^{-1}$.

When the laboratory simulation experiments are compared with the experiments on Mars, the following considerations should be taken into account. The capture of magnetic particles by the permanent magnets is a dynamic process. The interaction of arriving particles with particles already present on the target is of decisive importance. Furthermore, the MA used in the laboratory is identical to the arrays on the Mars Pathfinder lander except for one aspect. After glass sphere blasting, the surface of the flight version of the arrays was coated with a thin ($\sim 0.5 \mu\text{m}$) layer of platinum to have an electrically conducting surface and to provide some protection against corrosion. This sputtered layer does not, however, provide the array with sufficient protection to enable it to be cleaned. The arrays used in the laboratory are therefore coated by a hard lacquer. This treatment makes it possible to use the array many times for simulation experiments. The difference in surface treatment leads to a difference in the coefficient of friction for the same mineral.

6. Discussion

If we compare the results of the simulation experiment above with the experiment on Mars, we would tentatively conclude that also in the experiment on Mars the magnetization of the dust on the various magnets would be different. Each magnet has filtered out a subset of particles with a different spread in saturation magnetization. Magnet 1 can capture and hold grains with a broad distribution of saturation magnetization. The function describing the distribution of magnetization of the material held on magnet 1 will be different from the function describing the distribution of magnetization of the bulk material. The weaker magnets will have a decreasing ability to capture and hold weakly magnetic grains. The magnets may thus filter out grains with progressively narrowing distributions and with increasing average value of the saturation magnetization from magnet 1 to magnet 5. No grains on Mars were sufficiently magnetic to be stable on magnet 5.

This is an important result. If true, it suggests that the par-

ticles suspended in the Martian atmosphere must have a variable content of the magnetic phase and hence are composite. The magnetic phase is present in varying amounts in each composite grain, rather than as discrete magnetic particles. As previously mentioned, the results of the calculations of the relative capture cross sections of the magnets strongly suggest that the particles adhering to the magnets on Mars are composite (see Table 1b). The relative covering of the magnets corresponds approximately to the value of $0.1 \text{ T}^2 \text{ m}^{-1}$ for the parameter λ . This value of λ is typical for a magnetization between that of hematite ($\sigma_s = 0.4 \text{ A m}^2 \text{ kg}^{-1}$, $\lambda = 1.6 \text{ T}^2 \text{ m}^{-1}$) and that of maghemite ($\sigma_s = 70 \text{ A m}^2 \text{ kg}^{-1}$, $\lambda = 0.01 \text{ T}^2 \text{ m}^{-1}$), indicating composite particles.

Furthermore, we have performed a series of simulation experiments with other Mars sample analogs, and we have (until now) always observed some degree of variation in the magnetization of the grains sticking to the magnets of different strengths. We believe that the dust particles sticking to the four magnets on Mars are composite and they have different values of the saturation magnetization.

Using the results of the simulation experiments, and using results of the calculations represented in Figure 10, we have reached the conclusion that the dust particles suspended in the Martian atmosphere are composite particles with an average saturation magnetization of $4 \pm 2 \text{ A m}^2 \text{ kg}^{-1}$. As a firm conclusion, we can thus state that the reddish dust on Mars does not consist purely of hematite ($\alpha\text{-Fe}_2\text{O}_3$) or maghemite ($\gamma\text{-Fe}_2\text{O}_3$). Maghemite would stick to all five magnets, and hematite only to the strongest magnet.

We are also performing a series of simulation experiments with the TPM. As an example, we show some results in Figure 17. Figures 17a and 17b show that single-phase magnetic minerals ($\gamma\text{-Fe}_2\text{O}_3$, Fe_3O_4) have a tendency to form chains, while no chains are seen in Figure 17c. We have not yet been able to establish quantitatively the necessary conditions for chain formation. However, empirically we have not until now found chain formation with composite particles in which the nonmagnetic phases dominate the composition of the particles.

We see no chains on the images of the TPM from Mars. This result supports the idea that the particles suspended in the Martian atmosphere are composite.

6.1. Dust on the Surface and in the Atmosphere of Mars

The elemental composition of the soil on the Martian surface was measured by the Viking X-ray fluorescence spectrometer [Clark *et al.*, 1982] and by the alpha proton X-ray spectrometer on the Pathfinder rover [Rieder *et al.*, 1997].

The soils at the Pathfinder site have compositions similar to the soils measured at the Viking sites, but there are also some slight differences. Pathfinder soils are generally lower in S and somewhat higher in Ti than the Viking soils. In the first approximation, however, all soils measured have basically the same elemental composition. The amount of iron is given approximately as 18% Fe_2O_3 .

The soils at the Pathfinder site have been classified according to their reflectance spectra. The two most common soil types are labeled "bright soil" and "dark soil" [Smith *et al.*, 1997b]. Bright soils and dark soils may be perceived as a kind of end members, and soils spanning the reflectance range between these two units have been found.

The suspended dust that has settled on some rocks, for example, on the rock called Flat Top (the flat rock between the

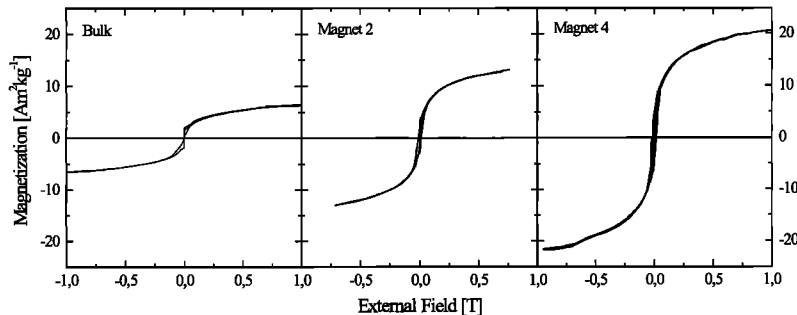


Figure 16b. Magnetization as function of impressed magnetic field of the bulk sample of the decomposed ochre, the material collected on magnet 2, and the material collected on magnet 4.

rocks named Bamm-Bamm and Moe, see *Science*, volume 278, 1997, Plate 6 on page 1741), has nearly the same optical spectrum as other bright soils on the surface of Mars.

One interpretation of the differences in the reflectance properties of the soils may be that the dark soil forming, for instance, the Mermaid dune is an intermediate weathering product that contains some silicates inherited from the parent basalts. The iron in the dark material may not have been completely oxidized from Fe^{2+} to Fe^{3+} [Smith et al., 1997b].

However, some of the difference in reflectivity may also be due to difference in particle size. It is well known that the optical reflectivity of particulate material of the same mineralogical composition is dependent on particle size. A particulate material having a small imaginary index of refraction appears brighter when finely divided [Hapke, 1993, Figure 11.2]. If difference in particle size is the cause of some of the difference in reflectivity, the darker patches of soil should contain the larger particles.

Concluding, we state that the results from the Viking mission and the Pathfinder mission are consistent with the notion that the small particles ($d \approx 3 \mu\text{m}$) suspended in the Martian atmosphere on the average have the same elemental composition and the same magnetic properties as the soil on the surface of Mars. This means that the particles in the soil on the ground as well as the dust in the atmosphere consist mainly of silicates [Clark et al., 1977; Toulmin et al., 1977; Rieder et al., 1997] mixed with a few percent of a strongly magnetic mineral.

6.2. Magnetic Properties of the Dust Suspended in the Martian Atmosphere

From the estimate of the growth of the bull's-eye pattern on the strong magnet of the upper magnet array, we previously concluded that most of the airborne particles on Mars are somewhat magnetic. Which mineral is giving rise to the magnetic properties of the airborne particles on Mars? Table 2 shows a list of well-known minerals carrying a spontaneous magnetization σ_s at and below 300 K.

The magnetism of soils is, however, more complicated than one would expect from the listing of magnetic minerals in Table 2. For example, isomorphous substitution of Fe with Al, Ti, and other ions occurs, and such substitutions alter the magnetic properties of the compounds. Another complication is introduced by small particle size ($d < 15 \text{ nm}$) because of the onset of superparamagnetism below a certain grain size and because some of the antiferromagnetic oxides and oxyhydroxides develop a substantial spontaneous magnetization.

The soil of Mars is known to be not only oxidized, but the soil is also oxidizing. The oxidizing character of the Martian

soil was proven by the fact that the soil was able to oxidize part of the organic nutrients to which the soil was exposed in the Viking biology experiment [Oyama and Berdahl, 1977].

Taking the oxidized character of the soil into account and also that the particles suspended in the atmosphere are small, we doubt that native iron or pyrrhotite (Fe_{1-x}S , $x \leq 0.1$), coated with a reddish surface layer of iron oxides, can be present on Mars. Magnetite ($\text{Fe}^{3+}[\text{Fe}^{2+}\text{Fe}^{3+}]_{\text{O}_4}$), which contains Fe^{2+} , is also doubtful due to the oxidizing character of the soil. However, magnetite is also unstable under present terrestrial conditions, and still magnetite is common on Earth.

The presence of ferric (Fe^{3+}) ions in the Martian soil has been abundantly confirmed by means of optical spectroscopy [Morris et al., 1989; Bell et al., 1990]. The spectral evidence strongly suggests that the iron is present mostly in the form of poorly crystalline Fe^{3+} compounds or as crystalline iron minerals of very small particle size (below about 10 nm), called "nanophase" particles or "nanocrystals" [Morris et al., 1989; Morris and Lauer, 1990]. At least some of the Fe^{3+} present in

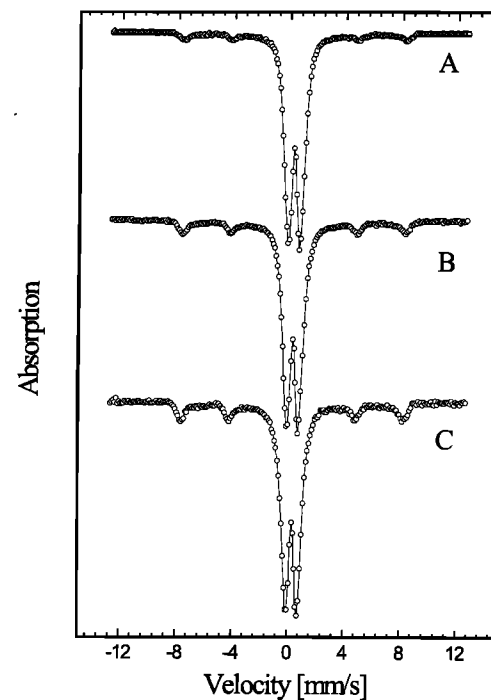


Figure 16c. Room temperature Mössbauer spectra of the same three samples for which the magnetization curves are given.

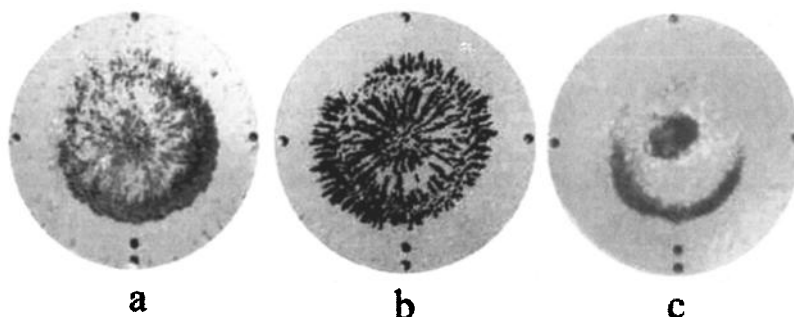


Figure 17. Laboratory simulations showing the patterns formed by three different samples on the tip plate magnet: (a) synthetic maghemite ($\gamma\text{-Fe}_2\text{O}_3$, $\sigma_s \approx 70 \text{ A m}^2 \text{ kg}^{-1}$); (b) beach sand from the island Anholt, Denmark, almost pure magnetite (Fe_3O_4 , $\sigma_s \approx 80 \text{ A m}^2 \text{ kg}^{-1}$); the particle size is different for the maghemite and the Anholt sand; and (c) black basaltic sand from Brædratunga, Iceland.

the soils of Mars must be located in crystals with dimensions substantially above the nanophase region because features indicating crystal field transitions in Fe^{3+} ions are present in some optical reflection spectra [Bell et al., 1990].

Hematite would stick almost exclusively to the strongest magnet (see Figure 15b). Because dust has been attracted to four magnets on Mars (Figure 11), macroscopic antiferromagnetic hematite can thus not be the cause of the magnetism in the airborne dust. This does not mean that the mineral hematite cannot occur in the particles. Hematite may be the cause of the reddish color of the soil, but a presence of hematite cannot explain the magnetic properties of the soil.

As seen in Table 2, nanophase superparamagnetic particles of hematite are substantially more magnetic ($\sigma_s \approx 5 \text{ A m}^2 \text{ kg}^{-1}$) than macroscopic hematite crystals ($\sigma_s = 0.4 \text{ A m}^2 \text{ kg}^{-1}$). It has been suggested [Morris et al., 1989] that nanophase hematite crystals are sufficiently magnetic to account for the magnetic properties of the Martian soil. If all the Fe_2O_3 in the soil of Mars is present as nanophase hematite, the calculated average magnetization of the surficial material is about $1 \text{ A m}^2 \text{ kg}^{-1}$. The hypothesis of nanophase hematite as the cause of the magnetism in the soil is, in our view, not likely.

The fact that we have not seen any distinct pattern on magnet 5 indicates that single-phase maghemite or single-phase magnetite are not present as free particles in the airborne Martian dust in any appreciable amount. A remote possibility for the magnetic phase in the soil is the mineral feroxyhyte, $\delta\text{-FeOOH}$ [Burns, 1980]. Feroxyhyte has a variable spontaneous magnetization of between virtually zero and $10 \text{ A m}^2 \text{ kg}^{-1}$. If, as we argue below, the particles are composites (mainly silicates) containing iron oxides and/or iron oxyhydroxides as a pigment or cement, all the iron should be present in one phase, namely, $\delta\text{-FeOOH}$, if the mineral responsible for the magnetization was feroxyhyte. Our results strongly point to the following.

Table 2. Magnetization of Selected Minerals

Mineral	Formula	$\sigma_s, \text{ A m}^2 \text{ kg}^{-1}$
Magnetite	Fe_3O_4	92
Titanomagnetite	$\text{Fe}_{3-x}\text{Ti}_x\text{O}_4$	≤ 92
Maghemite	$\gamma\text{-Fe}_2\text{O}_3$	70
Pyrrohotite	Fe_3S_8	~ 20
Feroxyhyte	$\delta\text{-FeOOH}$	≤ 10
Hematite	$\alpha\text{-Fe}_2\text{O}_3$	0.4
Nanophase hematite	Fe_2O_3	≤ 5

The particles suspended in the Martian atmosphere are composites and they have, on the average, essentially the same composition as the soil on the surface of Mars. The bulk composition of the Martian dust requires the presence of silicates [Clark et al., 1977; Toulmin et al., 1977; Rieder et al., 1997]. Most of the particles in the airborne dust are somewhat magnetic, and the dust has a substantial width in the distribution of saturation magnetization.

Maghemite, $\gamma\text{-Fe}_2\text{O}_3$ (rather than magnetite, Fe_3O_4 and certainly not hematite, $\alpha\text{-Fe}_2\text{O}_3$) is the mineral most probably responsible for the magnetization of the particles, and the maghemite is present as a component of composite particles of silicate and ferric oxide that constitute the bulk of the Martian soil and dust. The maghemite may be present as superparamagnetic particles ($d \leq 10 \text{ nm}$).

The content of maghemite (probably) varies from particle to particle. A few of the particles may have saturation magnetization up to about $10 \text{ A m}^2 \text{ kg}^{-1}$, corresponding to a content of up to about 15% maghemite in the dust on magnet 4 (Figure 11, sol 68). These more strongly magnetic particles have a higher probability of being caught and held by the magnets. Therefore the abundance of such particles in the dust forming the patterns on the magnets is higher than that in the dust suspended in the air. It should be noted that the amount of maghemite in the particles cannot be determined with a high degree of certainty. The saturation magnetization of maghemite particles is somewhat variable, especially for small particles ($d \leq 15 \text{ nm}$).

Calculations, and laboratory experiments with analog materials, lead us to an estimate of the average magnetization of the particles of $\sigma_s = 4 \pm 2 \text{ A m}^2 \text{ kg}^{-1}$. The iron oxides may be present as a stain on, or as a cement between, the silicate (clay?) particles. If our estimate of the average saturation magnetization of $4 \text{ A m}^2 \text{ kg}^{-1}$ will stand the test of time, about a third of the Fe_2O_3 in the dust will be in the form of maghemite, if the maghemite present in the particles has a saturation magnetization of $70 \text{ A m}^2 \text{ kg}^{-1}$.

The bulk magnetization of the SNC meteorites in an impressed magnetic field of $B = 280 \text{ mT}$ is at least an order of magnitude less than $4 \text{ A m}^2 \text{ kg}^{-1}$ [Cisowski, 1986]. Assume that the composition of the SNC meteorites is taken as an average composition of the Martian surface rocks. The magnetization of the Martian soil is then with certainty higher than the corresponding magnetization of the underlying rocks. This must be ascribed to the formation of secondary ferrimagnetic oxides

within the soil. The processes contributing to this are usually considered under the heading of "magnetic enhancement." The soil-forming processes on Mars somehow have converted iron in nonferrimagnetic form into ferrimagnetic phases (e.g., maghemite, $\gamma\text{-Fe}_2\text{O}_3$). This view is consistent with the most conspicuous evidence for chemical weathering on Mars: the reddish color of the surface of the planet and the spectroscopic features that identify ferric minerals in the Martian soil. The Fe^{2+} ions in the parent igneous rocks have been oxidized to ferric iron, which now occurs in the secondary minerals constituting the soil of Mars.

7. Summary and Conclusions

The interpretation of the magnetic properties experiment on Mars Pathfinder rests on the following.

1. The particles suspended in the Martian atmosphere have, on the average, the same elemental composition as the composition of the soil on the surface.

2. The particles are small, with linear dimensions equal to $3 \mu\text{m}$ or less.

3. The particles are composite, mostly silicates. They also contain Fe^{3+} compounds, probably including nanophase iron oxide minerals. The Fe^{3+} compounds are the cause of the reddish color of the particles.

4. Most particles are magnetic to some degree. This is true both for the particles in the surface soil (Viking mission) and for the particles suspended in the atmosphere (Viking, Pathfinder). The average saturation magnetization is estimated to be $4 \pm 2 \text{ A m}^2 \text{ kg}^{-1}$.

Our data (1) make it unlikely that the magnetic phase is occurring as a small subset of discrete highly magnetic particles among a major set of nonmagnetic particles; (2) preclude the possibility that the phase causing the magnetism of the soil is macroscopic hematite or distributed as superparamagnetic, nanophase hematite particles; (3) make it unlikely that the magnetic phase is inherited directly from the underlying bedrock and thus occurring as single-phase particles of titanomaghemite or titanomagnetite. The magnetic mineral is a secondary mineral. A magnetic enhancement with respect to the surface rocks on Mars has taken place by alteration of the rocks.

The phase responsible for the magnetic properties of the soil is most probably maghemite, $\gamma\text{-Fe}_2\text{O}_3$, present in intimate association with silicate particles and in an amount of about 6% by weight (on the average), perhaps more than 6% of maghemite if the saturation magnetization of the maghemite is substantially lower than $70 \text{ A m}^2 \text{ kg}^{-1}$. The maghemite may be present as superparamagnetic particles (dimensions $\leq 10 \text{ nm}$). The content of maghemite (probably) varies from particle to particle. A few of the particles may have saturation magnetization up to $10 \text{ A m}^2 \text{ kg}^{-1}$ corresponding to a content of up to 15% maghemite.

These results appear to require the formation of most of the dust particles by some form of hydrolytic alteration of the bedrock. This may include one or all of the following: surface weathering of crystalline or glassy volcanic rock (palagonitization [Bell et al., 1993; Morris et al., 1993]) or reaction with saline acid fog vapor [Banin et al., 1997], or finally, precipitation from solutions which had reacted hydrothermally below the surface and emerged as springs [Burns, 1993].

Acknowledgments. Our participation in the Mars Pathfinder Project is supported by the Danish Natural Science Research Council.

We acknowledge with thanks the assistance of the Imager for Mars Pathfinder Team, not only for supplying the decisive images, but also for the help given to us throughout a project which was more difficult than we had anticipated. One of us (R.B.H.) is supported by NASA grant 960869.

References

- Banin, A., F. X. Han, I. Kan, and A. Cecelsky, Acidic volatiles and the Mars soil, *J. Geophys. Res.*, 102, 13,341–13,356, 1997.
- Bell, J. F., III, T. B. McCord, and P. D. Owensby, Observational evidence of iron oxides on Mars, *J. Geophys. Res.*, 95, 14,447–14,461, 1990.
- Bell, J. F., III, R. V. Morris, and J. B. Adams, Thermally altered palagonitic tephra: A spectral and process analog to the soil and dust of Mars, *J. Geophys. Res.*, 98, 3373–3385, 1993.
- Burns, R. G., Does feroxyhyte occur on the surface of Mars?, *Nature*, 285, 647–649, 1980.
- Burns, R. G., Rates and mechanisms of chemical weathering of ferromagnesian silicate minerals on Mars, *Geochim. Cosmochim. Acta*, 57, 4555–4574, 1993.
- Cisowski, S. M., Magnetic studies on Shergotty and other SNC meteorites, *Geochim. Cosmochim. Acta*, 50, 1043–1048, 1986.
- Clark, B. C., III, et al., The Viking X Ray Fluorescence Experiment: Analytical methods and early results, *J. Geophys. Res.*, 82, 4577–4594, 1977.
- Clark, B. C., A. K. Baird, R. J. Weldon, K. M. Tsusaki, L. Schnabel, and M. P. Candelaria, Chemical composition of Martian fines, *J. Geophys. Res.*, 87, 10,059–10,067, 1982.
- Gunnlaugsson, H. P., The magnetic properties experiment on Mars Pathfinder and Mars Surveyor, thesis, Univ. of Copenhagen, Copenhagen, Denmark, 1997.
- Gunnlaugsson, H. P., S. F. Hviid, J. M. Knudsen, and M. B. Madsen, Instruments for the magnetic properties experiments on Mars Pathfinder, *Planet. Space Sci.*, 46, 449–459, 1998.
- Hapke, B., *Theory of Reflectance and Emissivity Spectroscopy*, Cambridge Univ. Press, New York, 1993.
- Hargraves, R. B., D. W. Collinson, R. E. Arvidson, and C. R. Spitzer, The Viking magnetic properties experiment: Primary mission results, *J. Geophys. Res.*, 82, 4547–4558, 1977.
- Hargraves, R. B., D. W. Collinson, R. E. Arvidson, and P. M. Cates, The Viking magnetic properties experiment: Extended mission results, *J. Geophys. Res.*, 84, 8379–8384, 1979.
- Hviid, S. F., et al., Magnetic properties experiments on the Mars Pathfinder lander: Preliminary results, *Science*, 278, 1768–1770, 1997.
- Morris, R. V., and H. V. Lauer, Matrix effects for reflectivity spectra of dispersed nanophase (superparamagnetic) hematite with application to Martian data, *J. Geophys. Res.*, 95, 5101–5109, 1990.
- Morris, R. V., D. G. Agresti, H. V. Lauer Jr., J. A. Newcomb, T. S. Sheffer, and A. V. Murali, Evidence for pigmentary hematite on Mars based on optical, magnetic, and Mössbauer studies of superparamagnetic (nanocrystalline) hematite, *J. Geophys. Res.*, 94, 2760–2778, 1989.
- Morris, R. V., D. C. Golden, J. F. Bell III, H. V. Lauer Jr., and J. B. Adams, Pigmenting agents in Martian soils: Inferences from spectral, Mössbauer, and magnetic properties of nanophase and other iron oxides in Hawaiian palagonitic soil PN-9, *Geochim. Cosmochim. Acta*, 57, 4597–4609, 1993.
- Oyama, V. I., and B. J. Berdahl, The Viking Gas Exchange Experiment results from Chryse and Utopia surface samples, *J. Geophys. Res.*, 82, 4669–4676, 1977.
- Pedersen, C. T., A. R. Dinesen, S. F. Hviid, M. B. Madsen, J. M. Knudsen, H. P. Gunnlaugsson, W. Goetz, and R. B. Hargraves, Laboratory experiments simulating the results of the magnetic properties experiment on Mars Pathfinder (abstract 1606), *Lunar Planet. Sci. Conf.*, XXIX [CD-ROM], 1998.
- Pollack, J. B., M. E. Ockert-Bell, and M. K. Shepard, Viking Lander image analysis of Martian atmospheric dust, *J. Geophys. Res.*, 100, 5235–5250, 1995.
- Rieder, R., T. Economou, H. Wänke, A. Turkevich, J. Crisp, J. Brückner, G. Dreibus, and H. Y. McSween Jr., The chemical composition of Martian soil and rocks returned by the mobile Alpha Proton X-ray Spectrometer: Preliminary results from the X-ray mode, *Science*, 278, 1771–1774, 1997.
- Rover Team, Characterization of the Martian surface deposits by the Mars Pathfinder rover, *Sojourner*, *Science*, 278, 1765–1768, 1997.

- Schofield, J. T., J. R. Barnes, D. Crisp, R. M. Haberle, S. Larsen, J. A. Magalhães, J. R. Murphy, S. Seiff, and G. Wilson, The Mars Pathfinder Atmospheric Structure Investigation/Meteorology (ASI/Met) Experiment, *Science*, 278, 1752–1758, 1997.
- Smith, P. H., et al., The Imager for Mars Pathfinder experiment, *J. Geophys. Res.*, 102, 4003–4025, 1997a.
- Smith, P. H., et al., Results from the Mars Pathfinder camera, *Science*, 278, 1758–1765, 1997b.
- Tomasko, M. G., L. R. Doose, M. T. Lemmon, P. H. Smith, and E. Wegryn, Properties of dust in the Martian atmosphere from the Imager on Mars Pathfinder, *J. Geophys. Res., this issue*.
- Toulmin, P., III, A. K. Baird, B. C. Clark, K. Keil, H. J. Rose Jr., R. P. Christian, P. H. Evans, and W. C. Kelliher, Geochemical and mineralogical interpretation of the Viking inorganic chemical results, *J. Geophys. Res.*, 82, 4625–4634, 1977.
- A. R. Dinesen, W. Goetz, H. P. Gunnlaugsson, S. F. Hviid, J. M. Knudsen, M. B. Madsen, C. T. Mogensen, M. Olsen, and C. T. Pedersen, Niels Bohr Institute for Astronomy, Physics and Geophysics, Ørsted Laboratory, Universitetsparken 5, University of Copenhagen, DK 2100 Copenhagen Ø, Denmark. (mbmadsen@fys.ku.dk)
- R. B. Hargraves, Department of Geological and Geophysical Sciences, Guyot Hall, Princeton University, Princeton, NJ 08544-1003.

(Received February 6, 1998; revised September 2, 1998; accepted September 15, 1998.)

The color of Mars: Spectrophotometric measurements at the Pathfinder landing site

J. N. Maki and J. J. Lorre

Jet Propulsion Laboratory, California Institute of Technology, Pasadena

P. H. Smith

Lunar and Planetary Laboratory, University of Arizona, Tucson

R. D. Brandt and D. J. Steinwand

Jet Propulsion Laboratory, Pasadena, California

Abstract. We calculate the color of the Martian sky and surface directly using the absolute calibration of the Mars Pathfinder (MPF) lander camera, which was observed to be stable during the mission. The measured colors of the Martian sky and surface at the Pathfinder site are identical to the Viking sites, i.e., a predominantly yellowish brown color with only subtle variations. These colors are distributed continuously and fall into five overlapping groups with distinct average colors and unique spatial characteristics: shadowed soil, soil, soil/rock mixtures, rock, and sky. We report that the primary difference between the sky color and the color of the rocks is due to a difference in brightness. Measurements of the sky color show that the sky reddens away from the Sun and toward the horizon and that the sky color varies with time of day and is reddest at local noon. We present a true color picture of the Martian surface and color enhancement techniques that increase image saturation, maximize color discriminability while preserving hue, and eliminate brightness variations while preserving the chromaticity of the scene. Although Mars has long been called the “red” planet, quantitative measurements of the surface color from telescopic and surface observations indicate a light to moderate yellowish brown color. The Pathfinder camera measurements presented here support the claim that the red planet is not red but indeed yellowish brown.

1. Introduction

In this paper we present spectral radiance and color measurements of the Martian sky and surface from data acquired by the Mars Pathfinder (MPF) lander camera. We calculate the perceptual color (Commission Internationale de l’Eclairage (CIE) tristimulus values) of the Martian sky and surface directly using the absolute radiometric calibration of the camera. This differs from the approach used by *Huck et al.* [1977] on the Viking lander, where the spectral radiance was estimated using a linear combination of basis functions [*Park and Huck*, 1976]. The Viking method was necessitated by the fact that the Viking color filters had significant out-of-band response and were performance-limited by planetary contamination requirements and corresponding biocleaning techniques. Our method eliminates the need for separate knowledge of the solar irradiance, the spectral reflectance of the scene, and the color calibration chips on the lander. We note here that color chips alone cannot be used for absolute color calibration because the colors of the chips are dependent on the illumination conditions (direct sunlight, atmospheric scattered light, and light reflected off of the lander) under which they are viewed. By using the absolute calibration of the camera, we eliminate the need for separate knowledge of the

Copyright 1999 by the American Geophysical Union.

Paper number 98JE01767.
0148-0227/99/98JE-01767\$09.00

illumination of the scene; this also allows us to examine the change in the color of the sky and surface as a function of time of day.

Color is that aspect of visual perception by which an observer may distinguish differences between two structure-free fields of view of the same size and shape caused by differences in the spectral composition of the radiant energy [*Wyszecki and Stiles*, 1982]. The human visual system compares the integrated intensity over three spectral regions (red, green, and blue) and classifies these intensities into the thousands of discernible colors that make up color vision. Humans rely on this experience in recognizing colors to assist in classifying objects and scenes. The calculation of the perceptual color of Mars allows an individual to experience the same visual sensation (aside from color acclimation) as if the individual were actually on the Martian surface. The calculation of the color of the Pathfinder landing site also enables the opportunity to directly compare the color of the Pathfinder landing site to the reported Viking colors. For these reasons, the calculation and the reproduction of the true color of the Martian surface is a useful and significant analysis tool both for the layman and for the experienced specialist.

The process of measuring and displaying the color of an object or scene consists of three steps: measuring the spectral radiance of the scene or object, converting the spectral radiance into colorimetric units, and converting the resulting colorimetric units into pixel intensity values for a particular display device. We discuss each of these operations in order.

Table 1. Responsivity Parameters for the Pathfinder Camera

Filter	Wavelength λ , nm	Bandpass $\delta\lambda$, nm	R_0	R_1	R_2
R0	443.2	26.2	117.9	-0.392	-0.0006
R5	671.2	19.5	557.3	-0.575	-0.0014
R6	752.0	18.9	787.1	-0.247	-0.0019
R8	599.5	21.0	592.7	-0.598	-0.0013
R9	530.8	29.6	578.6	-0.893	-0.0021
R10	479.9	27.0	368.1	-0.668	-0.0019
R11	966.8	29.6	393.5	2.185	0.0065
L0	443.3	26.2	128.8	-0.387	-0.0007
L5	671.4	19.7	575.3	-0.570	-0.0013
L6	801.6	21.0	872.2	0.237	-0.0029
L7	858.4	34.4	1435	2.491	0.0035
L8	897.9	40.8	1120	3.006	0.0059
L9	931.1	27.0	478.7	1.926	0.0051
L10	1002.9	29.1	213.4	1.606	0.0052
L11	968.0	31.4	395.8	2.027	0.0051

See *Reid et al.* [this issue] for a more detailed discussion of camera calibration.

2. Spectral Radiance

When the Pathfinder lander camera images a scene on the Martian surface, the amount of signal measured by the camera is digitized (to 12 bits) and sent back to Earth. Dividing this digital number (DN) by the exposure time t yields a flux value proportional to the absolute radiance of the image scene. The ratio of the measured signal to the absolute radiance of the scene is the sensitivity or responsivity R of the instrument. The camera responsivity in units of $(\text{DN}/\text{s})/[\text{W}/(\text{m}^2 \text{ st } \mu\text{m})]$ is

$$R(\lambda) = A\Omega\delta\lambda T_{\text{filter}}(\lambda) \frac{\text{QE}(\lambda)}{\text{gain}} \frac{\lambda}{hc} \quad (1)$$

where A is the area of a detector pixel in units of square meters, Ω is the solid angle subtended by the aperture (at the pixel-aperture distance) in steradians, $\delta\lambda$ is the spectral bandpass of the system in microns, $T_{\text{filter}}(\lambda)$ is the transmission of the optics and bandpass filter, QE is the quantum efficiency of the CCD detector, gain is the number of electrons per DN, h is Planck's constant (6.626×10^{-34} J s), c is the speed of light (2.998×10^8 m/s), and λ is the photon wavelength in nanometers. The camera responsivity can be approximated by a quadratic function in temperature that takes the form

$$R(\lambda, T) = R_0(\lambda) + R_1(\lambda)T + R_2(\lambda)T^2 \quad (2)$$

where the temperature T is in degrees Celsius and the values for $R_0(\lambda)$, $R_1(\lambda)$, and $R_2(\lambda)$ are included in Table 1. The work presented here is based on the preflight calibration, which was observed to be stable throughout the landed mission. For a more detailed discussion of camera calibration, see *Reid et al.* [this issue].

The absolute radiance S of a single pixel (at a location i, j in an image) is given by

$$S(i, j) = \frac{\text{DN}(i, j)}{tR(\lambda, T)G(i, j)} \quad (3)$$

where $\text{DN}(i, j)$ is the instrument signal (in units of DN), $G(i, j)$ is the normalized flat field of the camera system (which corrects for the pixel to pixel sensitivity variations), t is the exposure time of the image (in seconds), and $R(\lambda, T)$ is defined in (2) and in Table 1. The dark current of the camera

(i.e., the signal that does not correspond to photons incident onto the detector) is insignificant at the low Martian temperatures experienced by the lander camera and is not subtracted for the calculations presented here. During Mars Pathfinder surface operations, the largest dark current of the camera (1400 hours local solar time, camera temperature -9°C) was <2 counts/s (less than 0.5% in radiance for well-exposed pixels).

3. CIE Colorimetry

The modern science of colorimetry began with *Maxwell* [1860], and in 1931 the International Commission on Illumination (Commission Internationale de l'Eclairage, or CIE) defined the formalism for quantifying color vision that is used today [*Wyszecki and Stiles*, 1982]. This system has three components (corresponding to the red, green, and blue components of human vision). The tristimulus values represent the integrated intensity of incoming radiation weighted by a set of color matching functions and are given by

$$X = K \int_0^\infty S(\lambda) \bar{x}(\lambda) d\lambda \quad (4a)$$

$$Y = K \int_0^\infty S(\lambda) \bar{y}(\lambda) d\lambda \quad (4b)$$

$$Z = K \int_0^\infty S(\lambda) \bar{z}(\lambda) d\lambda \quad (4c)$$

where $S(\lambda)$ is the spectral radiance of the object as a function of wavelength and \bar{x} , \bar{y} , and \bar{z} are the CIE color matching functions (CMFs). The CMFs represent the amount of the three primary colors necessary to match a monochromatic stimulus and are related (but not equal) to the spectral sensitivity curves of the three types of cones in the typical human retina.

By design, \bar{y} is the photopic response of the human eye over the visible wavelength region. As a consequence, the Y tristimulus value is also a measure of the luminance (relative brightness) of an object. Both the spectral reflectance of an object and the illumination conditions under which it is viewed determine the color and luminance of an object; the spectral radiance $S(\lambda)$ of an object is the product of its reflectance $r(\lambda)$ and the incident irradiance $I(\lambda)$:

$$S(\lambda) = \frac{I(\lambda)r(\lambda)}{\pi} \quad (5)$$

The normalization constant K in (4) is given by

$$K = \frac{100}{\int_0^\infty S_L(\lambda) \bar{y}(\lambda) d\lambda} \quad (6)$$

where $S_L(\lambda)$ is the radiance of a perfect Lambertian reflector ($r(\lambda) = 1$), and $I(\lambda)$ is approximated as the value of the solar flux above the atmosphere.

The chromaticities of an object (pixel) are found by normalizing the tristimulus values

$$x = X/(X + Y + Z) \quad (7a)$$

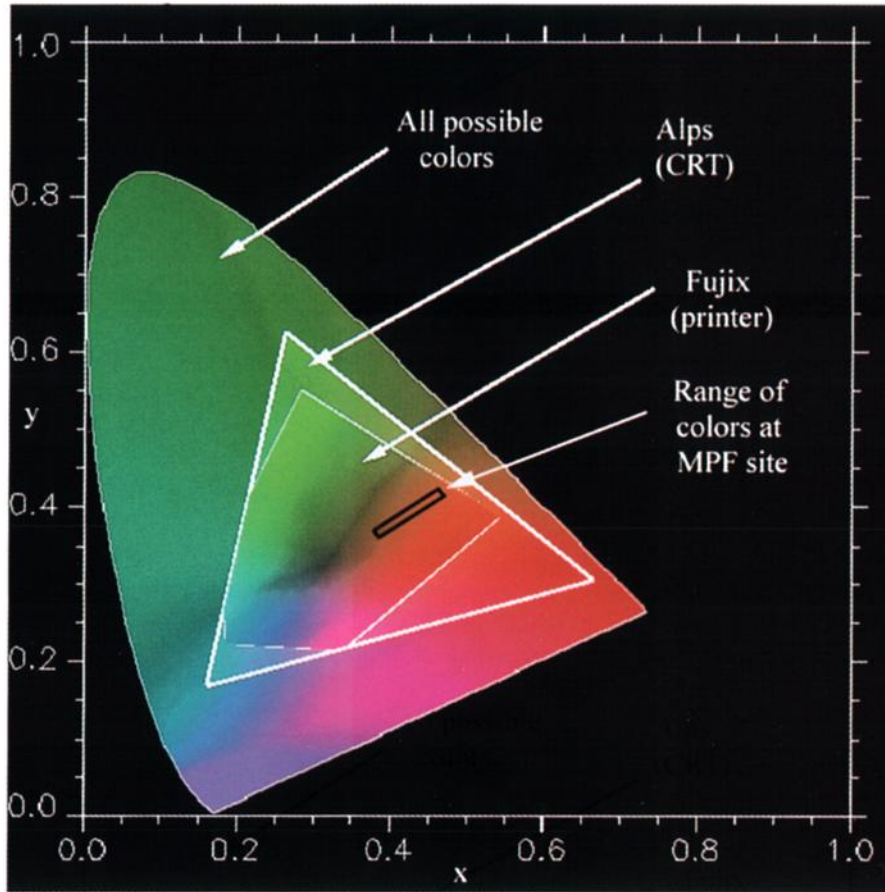


Plate 1. A CIE xy chromaticity diagram, containing the color coordinates of all possible colors, along with a schematic representation of the range of colors seen at the Pathfinder landing site. The curved edge of the color gamut is called the spectral locus and corresponds to the color of monochromatic stimuli. Superimposed onto the CIE color space is the gamut of a calibrated CRT computer monitor (an additive RGB device) named “Alps.” The R , G , and B device primaries correspond to the vertices of the triangle. Colors within the triangle (i.e., within the gamut) are generated by combining the RGB primaries. Colors outside the triangle cannot be generated and must be desaturated (i.e., brought into the device gamut) before being displayed. The gamut of a hard-copy printer (in this case a subtractive $CMYK$ device named “Fujix”) is smaller than the gamut of the CRT monitor. For illustrative purposes the relative brightnesses of the three gamuts have been arbitrarily varied.

$$y = Y/(X + Y + Z) \quad (7b)$$

$$z = Z/(X + Y + Z) \quad (7c)$$

Because $x + y + z = 1$, z is redundant. Thus the x and y chromaticities (along with the luminance Y) define a color. Plate 1 shows a chromaticity diagram containing the gamut of all possible colors. Within this gamut we show the gamut of two output devices (a CRT and a hard-copy printer), along with the range of chromaticities measured at the Pathfinder landing site.

For more detailed discussions of CIE colorimetry, see *Wyszecki and Stiles* [1982] or *Hunt* [1995].

4. Computing Tristimulus Values

There are three commonly used methods of converting from radiance units to color coordinates. We use method 1 in this paper.

4.1. Method 1

If the instrument measuring the spectrum of an object or scene has arbitrarily high spectral resolution, the radiance at each wavelength point is known exactly, and the tristimulus values can be calculated directly from the measured radiance spectrum. Because the camera samples the spectrum at discrete points, the spectrum $S(\lambda_i)$ is modeled as a curve (cubic spline) passing through each measured radiance point. $S(\lambda_i)$, in units of radiance, is integrated with the CMFs in (4) to obtain the XYZ tristimulus values, expressed below as sums:

$$X_i = K \sum S(\lambda_i) \bar{x}(\lambda_i) \quad (8a)$$

$$Y_i = K \sum S(\lambda_i) \bar{y}(\lambda_i) \quad (8b)$$

$$Z_i = K \sum S(\lambda_i) \bar{z}(\lambda_i) \quad (8c)$$

where the functions are summed discretely over the wavelength range for which $S(\lambda_i)$ is known.

Table 2. Data Used for Color Calculations

Panorama Name	Camera Sequence Numbers	Filters Used ^a	Compression Ratio	Time of Day	Sol	Notes
Gallery	0164–0166	R0 (440nm)	6:1	1100–1300 LST	9–11	entire panorama acquired during the same time of day, over a period of 3 days
Superpanorama	0181–0188	R5 (670nm) R9 (530nm) R0 (440nm) R10 (480nm) R9 (530nm) R8 (600nm) R5 (670nm)	6:1 6:1 lossless ^b 2:1 2:1 2:1 lossless	various; generally in the morning	13–83	acquired at various times of day; R9 and R10 overexposed in some frames.

^aR, right eye; L, left eye.

^bEarly portions of this panorama were initially taken 2:1 JPEG in R0.

4.2. Method 2

The tristimulus values can also be calculated directly by expressing them as a linear function of the measured radiances. Using this method, the tristimulus values are related to intensity by observing a set of i targets with known spectra (tristimulus values) in each of j filters and expressing X , Y , and Z as a linear combination of the camera responses $S(i, j)$:

$$X_i = a_1 S_{i1} + a_2 S_{i2} + a_3 S_{i3} + \dots + a_j S_{ij} \quad (9a)$$

$$Y_i = b_1 S_{i1} + b_2 S_{i2} + b_3 S_{i3} + \dots + b_j S_{ij} \quad (9b)$$

$$Z_i = c_1 S_{i1} + c_2 S_{i2} + c_3 S_{i3} + \dots + c_j S_{ij} \quad (9c)$$

The number of XYZ equations in (9) is equal to the number of targets measured, and the number of terms in each equation is equal to the number of filters in the camera system. The a , b , and c terms in the above equations are typically solved from the overdetermined set of XYZ equations by least squares. This method was used by the Galileo project for the solid-state imaging (SSI) instrument [Klassen and Breneman, 1988].

4.3. Method 3

When the filters of a camera system are broad relative to their spectral separation or have substantial out of band sensitivity, the above methods inaccurately calculate the tristimulus values. In this case the spectrum must be estimated by modeling it as a sum of basis functions. This requires detailed knowledge of the camera response as a function of wavelength, and the observed spectrum is determined by iteratively integrating it with the camera response function until the observed camera signal DN is obtained. This method was used for the Viking cameras [Park and Huck, 1976; Huck et al., 1977]. Method 1 was then used to obtain the tristimulus values.

4.4. Chromaticity Analysis

We used several sets of image data for our analysis. The first set is from the “gallery panorama,” a three-filter panorama acquired around local noon. Images in this panorama were compressed at 6:1 using the modified IMP Joint Photographic Experts Group (JPEG) compressor [Smith et al., 1997]. This time-continuous panorama contains over 10 million individual pixels per filter and covers the entire landing site. The second data set used in our analysis is a five-filter subset of the “superpanorama,” a multispectral panorama compressed losslessly in two filters and JPEG-compressed at 2:1 in all other geology filters (over 6 million individual pixels per filter). Un-

like the gallery pan, the superpan is not time continuous from frame to frame and does not cover the entire surface. Although the JPEG compression artifacts add noise to the measurements, we find that the computed color parameters are not significantly affected by lossy (6:1) compressed data (compared to the calculated color parameters from losslessly compressed data). For a more detailed discussion of the effects of JPEG compression on IMP images, see Reid et al. [this issue]. Table 2 summarizes the two data sets. We note that color estimates from the five-filter data have x chromaticities which are 0.01 higher than the three-filter data, and the five-filter data have y values slightly less (0.005) than the three-filter data. This difference is at the limit of human perceptibility [Wyszecki and Stiles, 1982]. We list the five-filter chromaticity values in Table 3.

Figure 1 shows two individual images of the Pathfinder landing site from the data set listed in Table 2. The images contain the five major color groups of material at the landing site: unshadowed soil, shadowed soil, rocks, a rock/soil mix, and the sky. See Figure 2 for the absolute spectral radiance of the soil, rock, and sky. Scatterplot chromaticity diagrams of these images (Figure 3) show that the color distribution on the surface is continuous and occupies a relatively small region in the CIE colorspace (i.e., the color variation is relatively small). In Figure 3, we have indicated the approximate boundaries of the color classes in the CIE colorspace. Though the boundaries are not distinct, the classes of material can be seen in the scatterplots. Figure 3b shows the sky as a distinct object. Below, we present techniques for redefining the colorspace to enhance these color differences.

The Inter-Society Color Council–National Bureau of Standards (ISCC–NBS) defined a standard color naming convention which defines color names in terms of calibrated color patches [Kelly, 1976]. This naming convention uses a set of hue names (red, orange, yellow, green, etc.) and their adjectival forms (reddish orange, yellowish green, etc.) along with modifiers (light, dark, pale, etc.). This system was used by Huck et al. [1977] to describe their results, and we find them equally useful. Translation of these color names into Munsell coordinates is described by Kelly [1976].

The measured chromaticity ($x = 0.43$ – 0.46 , $y = 0.38$ – 0.40) of the soil at the Pathfinder landing site corresponds to a moderate yellowish brown color (ISCC–NBS 77) and is in agreement with the Viking values (Table 3). The color of the surface as a function of azimuthal look angle does not signif-



Plate 2. The true color of Mars based upon three filters with the sky set to a luminance of 60. The color of the Pathfinder landing site is yellowish brown with only subtle variations. These colors are identical to the measured colors of the Viking landing sites reported by Huck *et al.* [1977]. This image should be illuminated with direct sunlight (or the corresponding CIE D65 illuminant) and viewed without surroundings containing brilliant colors.

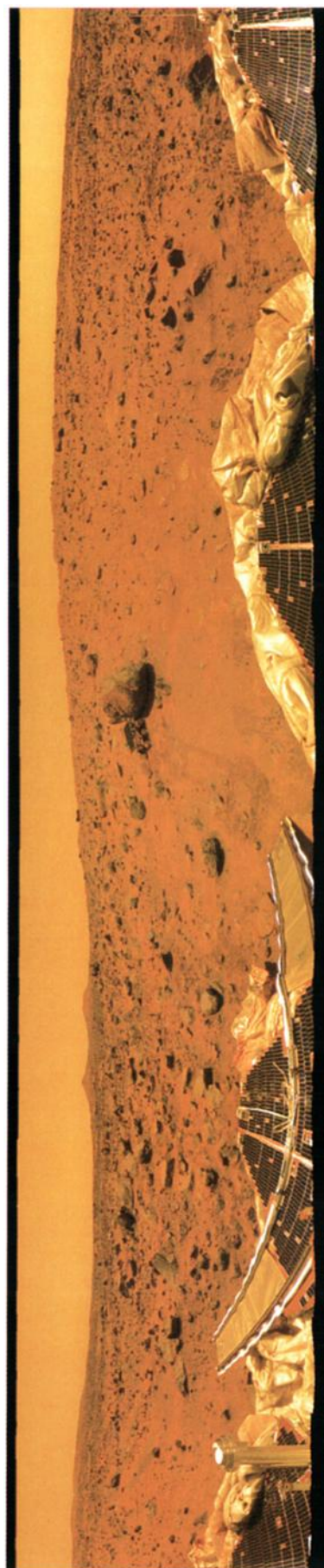


Plate 3. Color enhancement resulting from a multiplication of the saturation of the image in Plate 2 by a factor of 3. Hue and luminance have been largely preserved. Indistinct colors become artificially more vivid without a major loss of color balance.

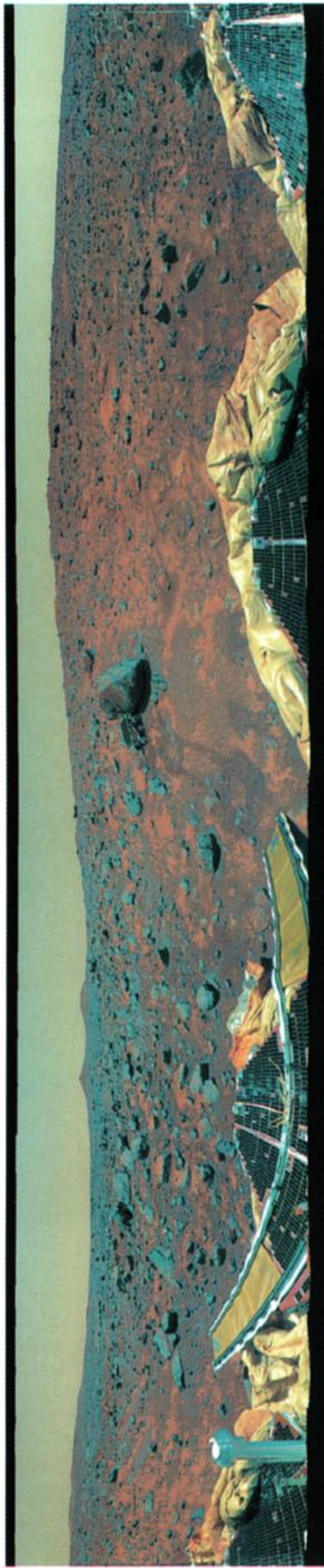


Plate 4. Color enhancement of Plate 2, resulting from the movement of the chromaticity coordinate $x = 0.405$ and $y = 0.380$ to neutral gray followed by a multiplication of the saturation by 3. Colors are now distributed about a new coordinate origin corresponding to the center of the distribution. With this artificial mapping, the eye can now easily discriminate between the colors of rocks, soil, and sky.

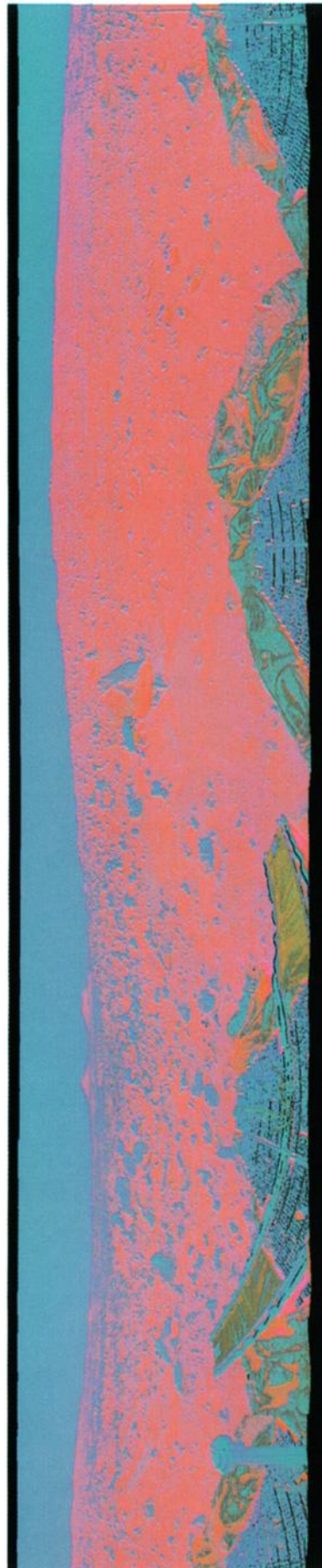


Plate 5. Color enhancement resulting from moving the chromaticity coordinate $x = 0.405$ and $y = 0.380$ to neutral gray, multiplying the saturation by 5, and replacing the luminance image by a constant of $Y = 25$. This eliminates the brightness variation in the image and enhances color differences. The colors of the shadows are now visible. Shadows are the reddest features, and the sky can be seen to more closely resemble the hue of rocks rather than soil.

Table 3. Color Estimates of the Martian Sky and Surface From Pathfinder (this paper) and Viking [Huck et al., 1977]

Location	Pathfinder		Viking 1		Viking 2		ISCC-NBS Color Designation
	x	y	x	y	x	y	
Sky	0.39–0.41	0.37–0.38	0.40	0.38	0.40	0.38	76–77 (light to moderate yellowish brown)
Rock	0.38–0.41	0.35–0.39	81 (dark grayish yellowish brown)
Rock/soil	0.41–0.43	0.38–0.40	58 (moderate brown)
Soil	0.43–0.45	0.38–0.41	0.43–0.46	0.39–0.40	0.43–0.44	0.39	77 (moderate yellowish brown); 78 (dark yellowish brown); 58 (moderate brown)
Shadowed soil	0.45–0.47	0.39–0.41	0.46	0.39	0.44	0.39	59 (dark brown)
Pathfinder Rover tracks	0.44	0.39	58 (moderate brown)

Data show the color of the sky and soil to be identical to the Viking sites. We compared (visually, with a color meter, and with the Color Names Dictionary [Kelly, 1976]) our prints to the ISCC-NBS centroid color chips [Kelly and Judd, 1968]. We find the sky color to be closest to ISCC-NBS chip 76 (light yellowish brown) and the soil color to chips 77 (moderate yellowish brown), 78 (dark yellowish brown), and 58 (moderate brown). Our matches to the ISCC-NBS color chips agree with those listed by Huck et al. [1977]. Additionally, we find the shadowed soil color as ISCC-NBS chip 59 (dark brown), and the color of the rocks as ISCC-NBS chip 81 (dark grayish yellowish brown).

icantly change (Figures 4 and Plate 2). We also note that the soil color is independent of time of day.

The light to moderate yellowish brown color ($x = 0.395\text{--}0.405$ and $y = 0.370\text{--}0.380$, or ISCC-NBS colors 76 and 77) of the noontime sky near the horizon is consistent with the sky color seen at the Viking sites [Huck et al., 1977]. The sky color varies as a function of time of day and azimuthal look angle (Figure 5). Figure 5 also shows that the sky is slightly redder in the anti-Sun direction and bluer in the direction of the Sun. This relative change in color is at the limit of perceptibility and would probably be difficult to notice with the naked eye while standing on the Martian surface. Figure 6 shows the color of the sky as a function of elevation, indicating that the sky reddens slightly near the horizon.

The color of the rocks at the Viking site was not reported due to difficulties in obtaining reproducible measurements [Huck et al., 1977]. We include the color of the Pathfinder rocks here and note that the rock radiance spectra are essentially identical in shape to the sky spectra except for a uniform intensity scale factor (where the sky is approximately 3 times brighter than the soil; see Figure 2). Thus the rock color ($x =$

$0.38\text{--}0.42$, $y = 0.35\text{--}0.39$) is similar to the sky color, and the perceived color difference between the sky and the rocks is due to the difference in brightness. The luminance values of the rocks are low enough that the rock color appears visually as gray, and if the brightness of the scene is set to be uniform throughout, the rocks and the sky have the same perceived color (Plate 5).

The color of the sky at sunrise and sunset is considerably different from the color of the noontime sky near the horizon. The sunrise/sunset sky has average chromaticity values ranging from $x = 0.34$ to 0.36 and $y = 0.34$ to 0.36 , which correspond to a grayish olive color (ISCC-NBS 110) or a brownish gray color (ISCC-NBS 64). This sky color becomes bluer toward the Sun, transitioning gradually from brownish gray at 15° to a bluish white color (ISCC-NBS 189) 5° from the Sun. At 2° from the Sun the x and y chromaticities are 0.28 and 0.29 respectively, which correspond to a very pale blue color (ISCC-NBS 184) or a very light blue (ISCC-NBS 180). Figures 7–9 illustrate this effect along with Plates 6 and 7.

We also examined the color of the tracks made by the Pathfinder rover [Rover Team, 1997]. The color of the subsurface



(a)



(b)

Figure 1. (a) Image taken at 0937 LST on sol 66 (sol = 1 Martian day = 24.6 hours), looking to the northwest. The rock named “Yogi” is in the upper right of the image. (b) Image taken at 1100 LST on sol 10, looking north.

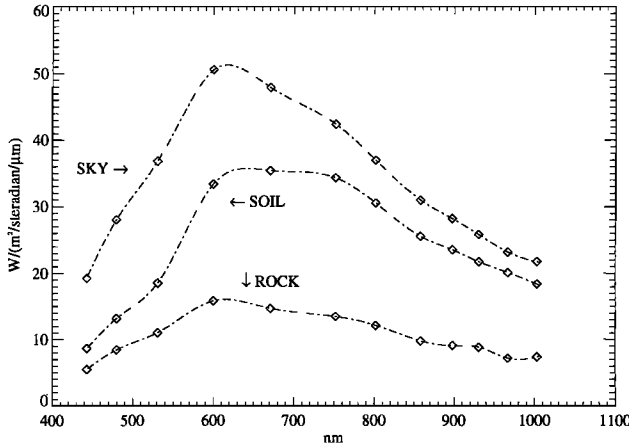


Figure 2. Spectral radiance of soil, sky, and a rock at the Pathfinder landing site. The measured data are shown as points connected with a cubic spline function. The rock spectrum and the sky spectrum have similar shapes, differing only by a constant scale factor in intensity (the scale factor for this particular example is approximately 3.2). The soil spectrum has a distinctly different shape than the sky or the rock spectra.

soil in the tracks ($x = 0.44$ and $y = 0.39$) is identical to the color of the surface soil material. A similar result was also reported by *Huck et al.* [1977] with the Viking trench soil.

5. Displaying the Color Data on Output Devices

Calculation of the CIE tristimulus values is a well-defined mathematical operation, and manipulation of these values (in the CIE colorspace) is a relatively straightforward process. Displaying the colors on output devices, however, is nontrivial and requires a careful calibration of the particular device. The xyY units calculated from (4) and (7) are in the CIE colorspace and are device independent. The image DN values of R , G , and B need to be specified through an xyY calibration table for a specific device. Similarly, radiance values must first be transformed through (4) into colorimetric units before being transformed into device units.

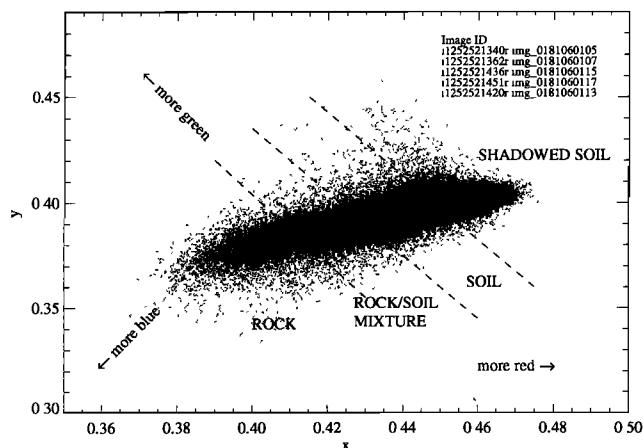


Figure 3a. Chromaticity plot for the image shown in Figure 1a. The values of x and y correspond to a yellowish brown color. The relative “redness” of the material increases from left to right. These data were computed using five filters.

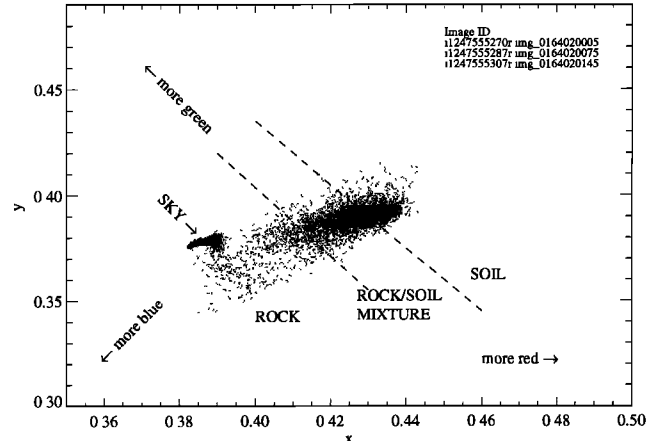


Figure 3b. Chromaticity plot for the image shown in Figure 1b. Only a representative portion of the pixels is shown in order to highlight the sky cluster. The sky chromaticity is within the range of values measured for the rocks. These data were computed using three filters.

5.1. Output Device Calibration

At the Jet Propulsion Laboratory (JPL) Multimission Image Processing Laboratory (MIPL) we calibrate our devices by measuring the xyY output for a large number of combinations of RGB input intensities and then interpolate to determine the amount of each device primary required to reproduce the desired xyY output values. This is done by displaying a data cube containing combinations of pixel RGB values onto the device and measuring the resulting xyY colorimetric response photometrically for each combination of RGB values. The cube typically contains 1000 xyY values (10 by 10 by 10). To calibrate a computer monitor, we strap a color meter onto the screen and measure these xyY values directly. The chromaticities of hard-copy prints are measured with a meter under a known illuminant such as D65 (Earth daylight, cloudless sky) using the same xyY cube approach.

Once the xyY cube has been populated for a particular device, the neighborhood of any target xyY value can be located and the corresponding RGB value interpolated within the xyY space. The xyY space is nonlinear in terms of equal

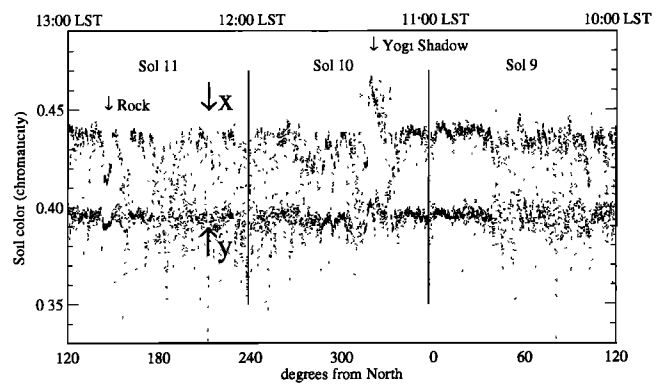


Figure 4. A 360°, 1-pixel-high strip of the surface color as a function of azimuthal look angle, showing that the average chromaticity does not vary as a function of azimuth. Note the relative redness of the “Yogi” rock shadow relative to the relative blueness of the rock material. See Plate 2 for the corresponding color print.

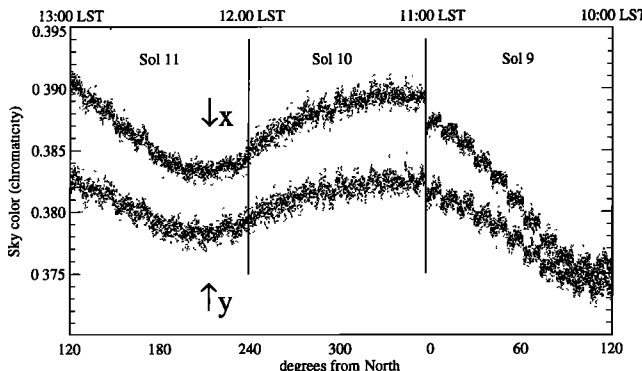


Figure 5. A 360°, 1-pixel-high strip of the chromaticity of the Martian sky as a function of both azimuthal look angle and local time, showing that the Martian sky color varies azimuthally and temporally. The data shown are from the three-filter “gallery panorama.” The panorama was acquired in a time-continuous fashion over a span of 3 days (from right to left in the figure). Local Mars time is on the top *x* axis and increases from right to left. The sky reddens slightly when looking toward the anti-Sun direction (north). The sky also reddens slightly from 1000 to 1100 LST. The “staircase” effect (most evident on sol 9) is due to 5 min pauses (during which the surface was being imaged) between the sky images. The large “step” between sol 9 and 10 is due to a 20 min difference in local acquisition time. See Plate 2 for the corresponding color print.

perceptual differences and is actually converted to a linear photovisual space such as $L^*a^*b^*$ or $L^*u^*v^*$ before the lookup process. In this fashion, any device can be modeled, whether it is additive (television monitor) or subtractive (film recorder or printer). The problem would be straightforward if all devices could reproduce all colors, but unfortunately, the gamut of any device is limited to a region between the chromaticities of its primaries in the *xy* chromaticity plane (Plate 1). This region narrows at low and high luminance. The problem of how to reassign out-of-gamut colors to others within the gamut of the device while preserving the hue is topologically complex, and we use the Candela commercial package offered

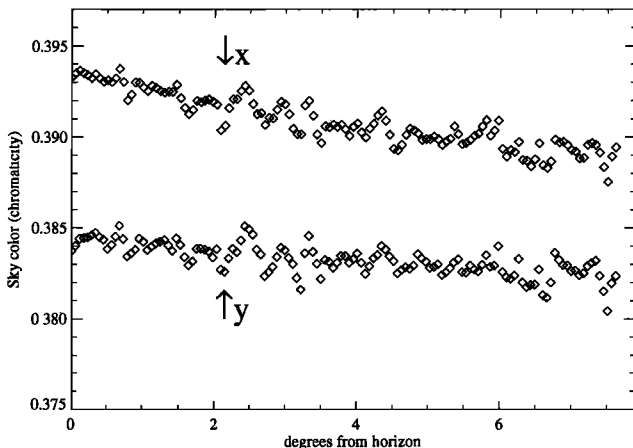


Figure 6. Sky color versus elevation, 1115 LST, NW direction. The sky is slightly redder near the horizon. See Plate 2 for the corresponding color print.

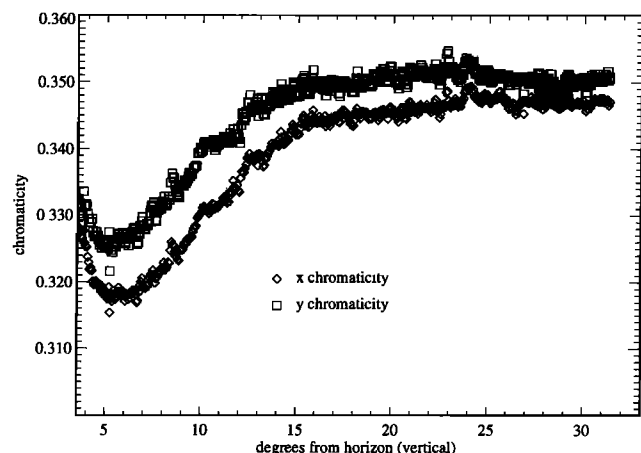


Figure 7. Sunrise, sol 39. The sky color at sunrise shows the same grayish brown color as seen at sunset. These predawn data show a reddening of the sky very near the horizon (<5° elevation), similar to the reddening shown in Figure 6. See Plate 6 for the corresponding color print.

by Candela, Ltd. of Burnsville, Minnesota, for mapping colors between devices.

5.2. Color Prints

The hard-copy prints in this paper must be viewed under the D65 illuminant (equivalent to Earth daylight on a clear day) in order to reproduce the correct color. We find that while artificial lighting (generally fluorescent) seems to produce acceptable results, viewing the prints under Earth sunlight on a clear day optimizes the color reproduction.

Using the techniques described above, we created color panoramas of the Pathfinder site using the three-filter “gallery” panorama data. Figure 10 shows the *x* and *y* chromaticity values of the landing site as grayscale images. Plate 2 shows a color image of Mars as it would be seen by a human observer on the Martian surface. Nearly everything is a similar yellow

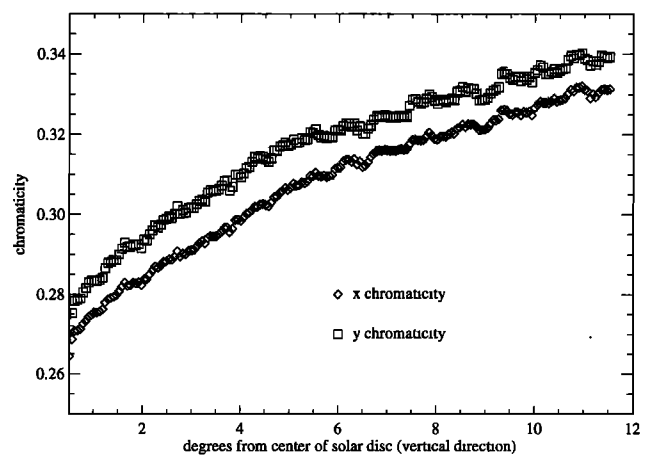


Figure 8. Sunset, sol 24. The color of the sky at sunset, shown as a function of vertical elevation. The sky slowly reddens away from the Sun, in the vertical direction. The color of the sky near (within 2°) the Sun is a very pale blue (ISCC-NBS 184), and farther away from the Sun (15°) the sky is a brownish gray color (ISCC-NBS 64), with a slight hint of a grayish moderate olive brown (ISCC-NBS 95). See Plate 7 for the corresponding color print.